POLITECNICO DI TORINO

Master's Degree in Nanotechnologies for ICTs

Master's Degree Thesis

Chemical Vapour Deposition of atomically thin $MoTe_2$ and its Optical and Morphological characterizations

Supervisors

Prof. Matteo COCUZZA

Dr. Christian MARTELLA

Candidate

Sara GHOMI

Academic Year 2020-2021

Summary

Graphene has been one of the most exploited 2D materials in various fields. However, it is not the most suitable candidate for many electronic devices unless its bandgap structure is tuned through functionalization. Recently, among the post-graphene 2D materials, transition metal ditellurides, like $MoTe_2$, have gained increasing research interest due to their unique physical properties.
They offer two stable allotropic states, namely the semiconducting 2H phase and the metallic 1T' phase, with a low energy difference of $44meV$. Consequently, the phase transition between its semiconducting and metallic phase is likely to happen, thus making them suitable candidates for "phase-change" related applications, like 2D non-volatile memory devices and memristors.

Applications require the growth of broad-area and high-quality samples, which is a non-trivial challenge due to tellurium's low reactivity. In this thesis, I dedicated my efforts to a systematic study on the synthesis of ultrathin $MoTe_2$ films through chemical vapor deposition (CVD), aiming to obtain centimeter-scale deposition with high crystalline quality (large grain size, phase uniformity, etc..).
I developed a protocol for the growth of few-layer $MoTe_2$ based on a tellurization approach, which takes advantage of a thin metal molybdenum film pre-deposited on the SiO_2/Si substrate exposed to tellurium vapors.

A vital aspect consisted of determining the thermodynamics and kinetics constraints in the CVD reaction, enabling the material's growth in one specific allotropic phase. In this context, different experimental parameters such as temperature, carrier gas flux, boat distance, substrate configuration, and growth time were tuned to optimize the growth. Aiming at optimizing the deposition condition, I also developed a simulation tool for modeling the precursor gradients, concentration, carrier gas fluxes, and temperature distribution starting from Navier-Stokes and mass-transport equation solved in the COMSOL environment.

The material quality assessment was performed by investigating morphological and physical properties at the nanoscale using atomic force microscopy (AFM)

operating in different modes: tapping, Kelvin-probe, and electrostatic force. The structural and optoelectronic investigations of the films were carried out by confocal micro-Raman spectroscopy. Moreover, before the characterization of the grown material, I used the AFM and Raman techniques to investigate $MoTe_2$ crystal flakes obtained by mechanical exfoliation of commercial bulk samples. I used the measurments on the flakes as a reference set of data to assess the quality of the grown material.

In this work, I will show that the adopted CVD approach allows the $MoTe_2$ deposition uniformly on the $4cm^2$ $SiO_2(50nm)/Si$ substrate in the 1T' dominant phase with ultra-scaled (7 nm) thickness.

The thesis is organized as follows:

Chapter 1 Transition Metal Dichalcogenides: In this chapter, I will present the class of the Transition Metal Dichalcogenides (TMDs) in terms of their physical properties and potential technological applications. I will focus on $MoTe_2$ as a member of the TMDs, pointing out the main aspects of his crystalline, electronic and vibrational properties.

Chapter 2 Methodology: In this chapter, I will describe the experimental and theoretical methodologies that I used to grow and characterize the Mote2 samples. I will focus on CVD, AFM, Raman scattering, and numerical simulations with COMSOL software. I will show the characterization of exfoliated $MoTe_2$ flakes in both the allotropic phases.

Chapter 3 $MoTe_2$ growth results and discussion: In this chapter I will present the results of my systematic study on the growth of $MoTe_2$ samples by CVD. Changing the experimental parameters, I will show that it is possible to optimize the quality of the grown $MoTe_2$ layers in terms of morphological and structural order. I will also discuss and compare the trends predicted by the numerical simulations with the experimental results.

Chapter 4 Conclusion: I will summarize my activity's main results and discuss the outlook and perspective for further improving the $MoTe_2$ growth.

Appendix: This section will include a brief overview of side results obtained during my experimental activities as the attempts to grow a thin film of tellurium on a large scale by CVD.

Acknowledgements

It was an excellent opportunity for me to work on my Master's thesis activity at the National Research Council of Italy for Microelectronics and Microsystems (CNR-IMM), Unit of Agrate Brianza.

First of all, I would like to express my sincere gratitude and appreciation to my supervisor **Dr. Christian Martella** for the continuous support of my thesis study and research, for his patience, motivation, dynamism, and immense knowledge. He has taught me the methodology to carry out the thesis and the principles of Atomic Force Microscopy as clearly as possible. It was a great opportunity and honor to work and study under his guidance. I am incredibly grateful for what he offered me and encouraged me at different stages of this research.

I would also like to thank **Dr. Alessio Lamperti** for providing valuable guidance during this thesis and **Dr. Alessandro Molle**, research director at CNR-IMM, for giving me the chance to work in this laboratory in an exciting research environment. I sincerely thank **Prof. Matteo Cocuzza**, Professor at Politecnico di Torino, for accepting and being my internal supervisor to my thesis activity in CNR-IMM. I would like to thank all the other lab members, postdocs, and Ph.D. students from the CNR-IMM Unit of Agrate Brianza for supporting and inspire me throughout my master thesis.

Last but not least, I would like to thank my family and friends for all their encouragement and support. Finally, my heartfelt thanks go to Arian, who helped me to find my way and care about me in every moment.

Look deep into nature, and then you will understand everything better.

Table of Contents

List of Tables

List of Figures

Chapter 1

Transition Metal Dichalcogenides

1.1 Two-dimensional Materials

Two-dimensional materials have attracted strong research attention due to their outstanding properties and applications in electronics, optoelectronics, spintronics, and valleytronics. They are layered crystalline solids with strong bonding in one crystalline plane while the neighboring atomic planes are held together by much weaker van der Waals forces [1]. Its van der Waals interaction enables 2D materials to construct a vertical heterostructure without suffering the lattice mismatch issues when using layers with different lattice constants [2]. Due to the absence of surface groups or dangling bonds, the charge carrier scattering is also reduced in the 2D materials as compared to the bulk [3].

Among the family of 2D materials, graphene was first discovered and studied as early as 2004 [4]. Graphene was first isolated from Highly Oriented Pyrolytic Graphite (HOPG). The interesting properties of graphene are rapidly growing among the layered materials, especially when thinned down to the atomic thickness. However, there are some properties in graphene such as the lack of bandgap, limiting its applications in modern electronics. Graphite has a very anisotropic crystal structure with strong covalent bonds lying in the 001-oriented planes but weak interatomic interactions between the adjacent layers as pictured in Figure 1.1 [5].

The unit cell of graphene contains two Carbon atoms, Each of them belongs to a separate triangular sublattice. The valence and conduction bands of graphene, known technically as π and π^* bands, show a linear relationship between electron energy and momentum and meet at specific points (K and K'), as depicted in the Figure 1.2, making it a gapless material.

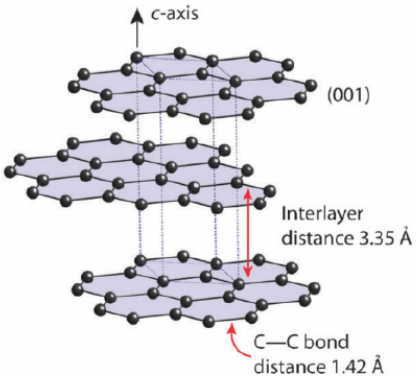

Figure 1.1: Ball and stick model for 3-layer graphene [5]

In order to generate a finite gap in the energy dispersion of graphene, several models have been proposed, including hydrogenation and fluorination, cutting graphene into ribbons, the alloying of graphene with hexagonal boron nitride (h-BN), and graphene–substrate interaction [6]. However, they result in the reduction of the carrier mobility of graphene.

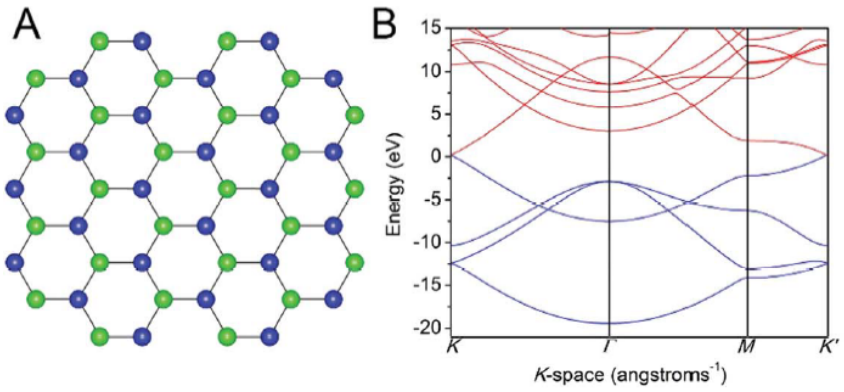

Figure 1.2: (A) Hexagonal arrangement of carbon atoms in a graphene sheet, (B) Band structure calculated for single-layered graphene [7]

After the discovery of graphene, many other 2D materials have been discovered and studied. Extensive research has been done to study the physical, chemical, and electrical properties of these materials. While graphene is semi-metallic, other 2D materials are insulating (e.g., hexagonal boron nitride, h-BN) or semiconducting (e.g., molybdenum disulfide, MoS_2) or metallic (e.g., tungsten ditelluride, WTe_2), or superconducting (e.g., niobium diselenide, $NbSe_2$) [8].

1.2 Transition Metal Dichalcogenides

The methodology learned in the search for graphene have been extended to other layered materials. Two-dimensional Transition Metal Dichalcogenides come into play due to the sizable bandgap. Transition metal dichalcogenides (TMDs) are a large family of two-dimensional (2D) layered materials with lamellar structures similar to that of graphite as indicated in Figure 1.3. They have received significant attention because of their various properties and natural abundance.
This type of material exhibits strong in-plane covalent or ionic bonding and weak out of the plane van der Waals bonding. TMDs are the well-studied system for layering van der Waals solids. They can form heterojunctions with each other and exploit them as the building blocks for the realization of functional new materials.

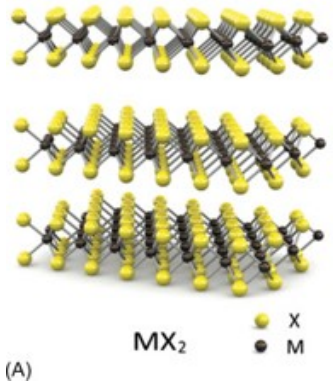

Figure 1.3: Layed Van der Waals structure of MX_2 [9].

1.2.1 Structural Properties

The chemical formula of TMDs is MX_2, M is the transition metal of groups 4–10 (typically Mo, Nb, W, Ni, V, or Re), and X is a chalcogen (typically Se, Te, or S). Group 4–7 TMDs in Figure 1.4 are predominantly layered, whereas some of group 8–10 TMDs are commonly found in non-layered structures. Each layer typically has a thickness of 6∼7 Å , consisting of a layer of metal atoms sandwiched between two layers of chalcogen atoms [10].

The group VI of TMDs (M = Mo and W, X = S, Se, and Te), has attracted more research interests, due to the electronic and catalytic properties of its 2D counterparts. One of the outstanding properties of Group VI TMDs is their layer-dependant band structure tunability. In the bulk materials they have indirect bandgap, and when they thinned down to a monolayer it changes to direct bandgap. The van der Waals heterostructures exhibit gaps between the constituent layers, and

they bridge them by weak van der Waals forces. Interfaces in these heterostructures are found to be clean and atomically sharp. Since the van der Waals forces that attract adjacent crystals and effectively squeeze out trapped contaminants or force them into micrometer-sized 'bubbles' [11]. In comparison, the conventional heterostructures derived from 3D solids involve a covalent bond between the layers.

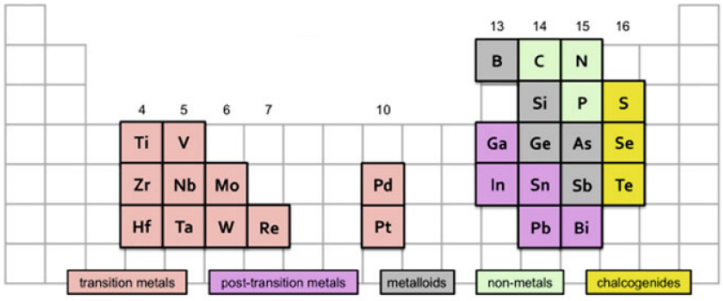

Figure 1.4: Simplified periodic table highlighting the elements, which form the most common layered and 2D materials MX_2 [3].

In contrast to graphite, Bulk TMDs exhibit a variety of Polymorphs. It is because each metal sublayer is sandwiched between two chalcogenides sublayers, so, M atom is sixfold coordinated with X atoms. Transition metal atoms have trigonal prismatic coordination and octahedral or distorted octahedral coordination. Single-layer TMD exhibits various phase structures such as H-, T- or T'- phases. The coordination of metal atom in H- phase has hexagonal symmetry (D_{3h}), T-phase has octahedral (D_{3d}), and in 1T', it's distorted.

1. ***Trigonal Prismatic:*** Belongs to the D_{3h} point group, 2H semiconducting phase, the above three X atoms are vertically above the below ones.

2. ***Octahedral:*** Belongs to the D_{3d} group, 1T metallic phase, the top and bottom chalcogen layers are in registry with different Mo-layer hollow sites

3. ***Distorted Octahedral:*** 1T' metallic phase, The 1T' phase represents a 2 $\times$ 1 reconstruction of the 1T phase leading to slight buckling of each atomic plane (Figure 1.5).

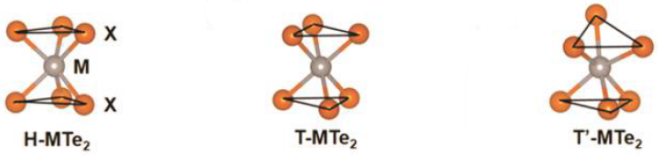

Figure 1.5: Atomic configuration of H, T and T' phase of monolayer transition metal dichalcogenide MTe_2 (M = Mo) [12].

In the single layer of sandwiched structure, the atoms arrangement is along the c-axis, the stacking sequence AbA is for the H-phase and AbC is for the T-phase, where A and C indicate chalcogen atoms and b represents the metal atom (Figure 1.6). Density functional theory calculations indicated that different polymorph structures (H and T) of monolayer TMDs could have different equilibrium relative energies [13].

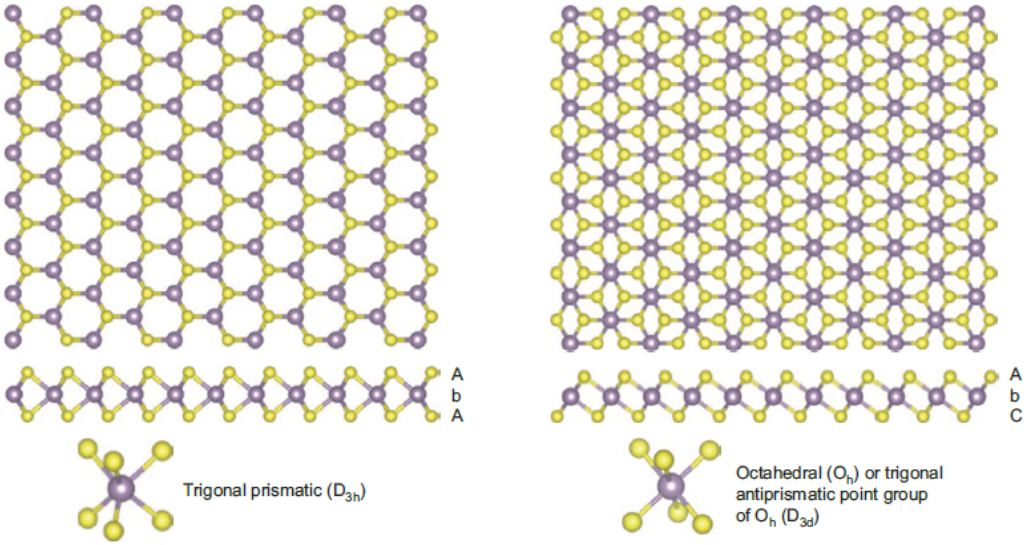

Figure 1.6: c-Axis and section view of transition metal atom coordination [10].

In the macroscopic bulk crystal structure, or more precisely, for an even number of monolayers, the crystal structure has an inversion center. In the case of a monolayer (or any odd number of layers), the crystal may or may not have an inversion center [14]. As a consequence, the lack of inversion symmetry allows unusually strong optical second harmonic generation (SHG) in monolayer structure [15].

1.2.2 Electronic Properties

According to the ligand field theory, the metallic nature of the 1T phase is caused by the partially filled t_{2g} band (d_{xy}, d_{xz}, d_{yz}). In contrast, the semiconducting behavior of the 2H phase is due to the filled d_{z^2} and empty d_{xy} and $d_{x^2-y^2}$ orbitals. The type of symmetry adopted by a TMD depends primarily on d orbital filling, i.e., the d electron count of the transition metal. Group 4 TMDs (defined as d0 transition metal) are preferred to be in the 1T phase, whereas both octahedral and trigonal prismatic phases are in group 5 TMDs (d1). Group 6 TMDs (d2) are in 2H geometry, and group 7 TMDs (d3) are typically in a distorted octahedral structure. Group 10 TMDs (d6) are all in an octahedral arrangement (Figure 1.7).

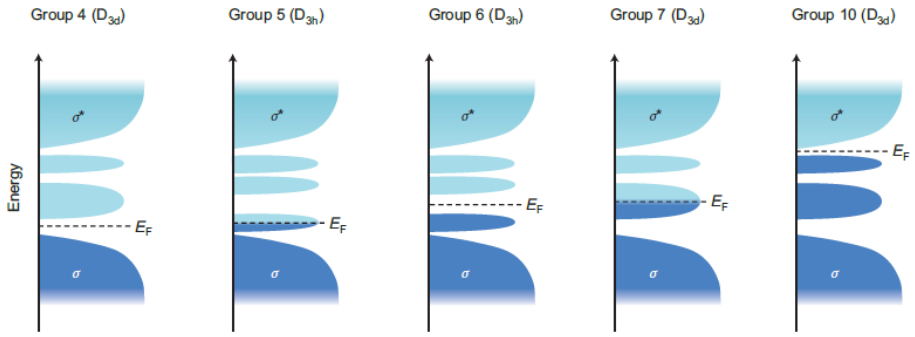

Figure 1.7: Progressive filling of d orbitals between the bandgap of bonding and antibonding states in group 4, 5, 6, 7 and 10 of TMDs [10].

In groups 5 and 7 of TMDs, the orbital is partially filled, and Fermi level E_F is located within the bandgap, and they exhibit metallic behavior. In group 6, the orbital is fully filled, and the Fermi level is in the bandgap, consequently showing semiconducting character.

1.3 Molybdenum ditelluride

Among group VI TMDs, Molybdenum ditelluride is getting attention because of its unique physical and structural properties. $MoTe_2$ exhibits two common electronic structures: 2H phase, a trigonal prismatic structure, which is a semiconductor, and 1T' has a distorted octahedral structure is metal.

Monolayer 2H-Molybdenum ditelluride has a direct bandgap of $\approx 1.1eV$ [16], which is the lowest among group VI TMDs and can be integrated with silicon photonics. In addition, 2H $MoTe_2$ shows a low thermal conductivity of $\approx 2W/(m.K)$, and a high Seebeck coefficient of $780\mu V/K$ [17]. Because of the heavy element of Te, it also causes strong spin-orbit coupling, which makes it attractive for spintronics applications. 1T'-Molybdenum ditelluride is also interesting in different applications and benefits from outstanding features. Bulk 1T'-$MoTe_2$ exhibits a maximum carrier mobility of $4000cm^2/V.s$ and magnetoresistance of 16000% in magnetic field 14T at 1.8K. In few-layered 1T'-$MoTe_2$, it exhibits a bandgap opening of 60meV [18].

The driven calculations by Density Functional Theorem show that the energy difference between 2H and 1T' phases is sufficiently tiny (43meV) [19], so it can be exploited as a phase-changing material. Furthermore, 1T'-$MoTe_2$ can be used in topological field-effect transistors, which takes advantage of topological phase transition to realize fast on/off switching [20].
The figure below represented the DFT calculated band structure for three different phase structures. 2H-$MoTe_2$ bandgap is direct, for 1T-$MoTe_2$ 1T MoTe2 is metallic; a valence band crosses the Fermi level at the K point by a tiny amount and a conduction band crosses below the Fermi level by a similar, minimal amount at a low-symmetry point along $\Gamma - K$. In 1T'-$MoTe_2$, the states near the VBM and CBM changed to some extent due to the crystal field's low symmetry.

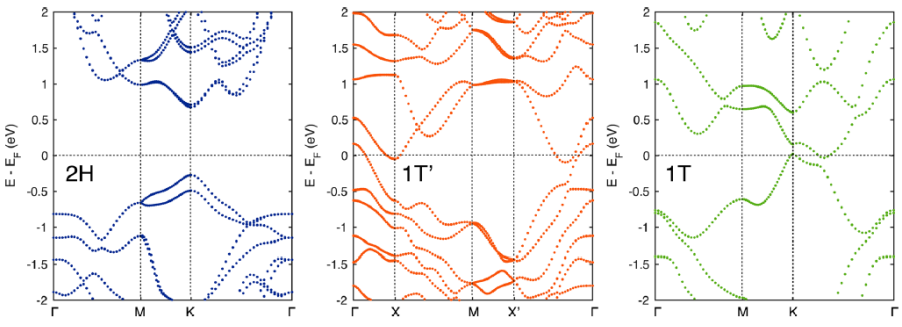

Figure 1.8: DFT calculated band structure of (a) 2H $MoTe_2$, (b) 1T $MoTe_2$, (c) 1T' $MoTe_2$ [21]

1.3.1 Vibrational Properties

The vibrational properties of $MoTe_2$ are shared with the other TMDs since they exhibit the same crystal structures (2H and the 1T' phase). However, the phonons' energy is different, resulting in different Raman spectra. The number of layers affects the vibrational properties. As the number of layers changes from odd to even, the space group varies until the crystal can be considered bulk.

Assign Raman Peaks in $MoTe_2$

Lattice vibrations are denoted by using the "Irreducible representation" of factor group crystals, So from this we can determine the optical activities of these vibrations: Raman active (R), Infrared active (IR) and optically silent [22]. The intensity of raman active mode is:

$$I = |e_s R e_i|^2 \tag{1.1}$$

With e_s and e_i the polarization vectors of scattered and incident photons along x, y, z and R describes a second rank tensor called the Raman tensor. The factor group at Γ point of the first Brilloiun zone is the point group which crystal belongs to, For example it is D_{6h} for the $MoTe_2$.
The irreducible representations of the phonons in bulk MX_2 at Γ point is:

$$\Gamma = A_{1g} + 2A_{2u} + 2B_{2g} + E_{1g} + 2E_{1u} + E_{2u} + B_{1u} + 2E_{2g} \tag{1.2}$$

However, single- and few-layers of $2H_b - MX_2$ belong to different space groups, depending on the parity of the number of layers, so:

$$\Gamma_{odd} = \frac{3N-1}{2}(A_1' + E'') + \frac{3N+1}{2}(A_2'' + E') \tag{1.3}$$

$$\Gamma_{even} = \frac{3N}{2}(A_{1g} + A_{2u} + E_g + E_u) \tag{1.4}$$

In the figure below, it is indicated the phonon modes for 1L, 2L and bulk of $2H_b - MX_2$. For example there are 3 raman active modes in bulk and 4 raman active mode in bilayer.

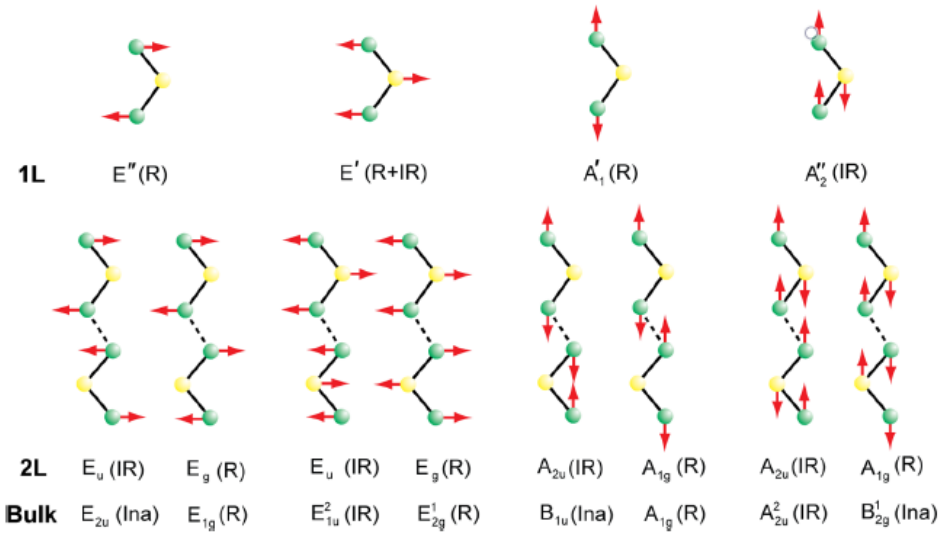

Figure 1.9: Phonon modes of 1L, 2L and bulk $2H_b - MX_2$ [23]

In the 3L $MoTe_2$ there are 2 Raman active modes which in (i) mode, the Te atoms are oscillating in-phase, but in the (j) mode, the central layer is phase shifted 180. The figure right, indicates the vibrational modes of 2L $MoTe_2$.

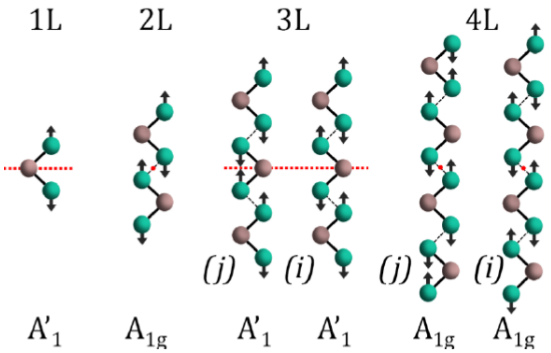

Figure 1.10: Raman active vibrational modes in $MoTe_2$ [24].

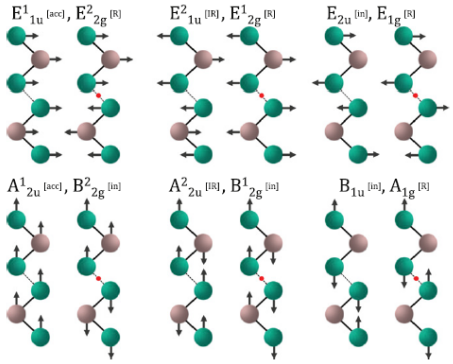

Figure 1.11: Vibrational modes in $MoTe_2$ [25]

The result of a Raman spectroscopy measurement is the intensity of light plotted against the frequency above and below the frequency of incident light (represented as reciprocal centimeters (cm^{-1})).
The fingerprint of 1T' mode which is the B_g mode at 161 cm^{-1}. The other first-order Raman active modes are at 107 cm^{-1}, 127 cm^{-1}, and 256 cm^{-1} which are assigned to A_u, A_g, and A_g modes of vibrations.

In 2H the E^1_{2g} mode at 232 cm^{-1} is the major peak. The other Raman characteristics peaks are 117 cm^{-1}, 172 cm^{-1}, and 291 cm^{-1} which they are assigned to E_{1g}, A_{1g}, and B^1_{2g} respectively [26].

The intensity ratio could be evaluated in order to determine the dominant phase in the growth film.

$$\frac{1T'}{1T' + 2H} = \frac{I_{B_g}}{I_{B_g} + I_{E^1_{2g}}} \tag{1.5}$$

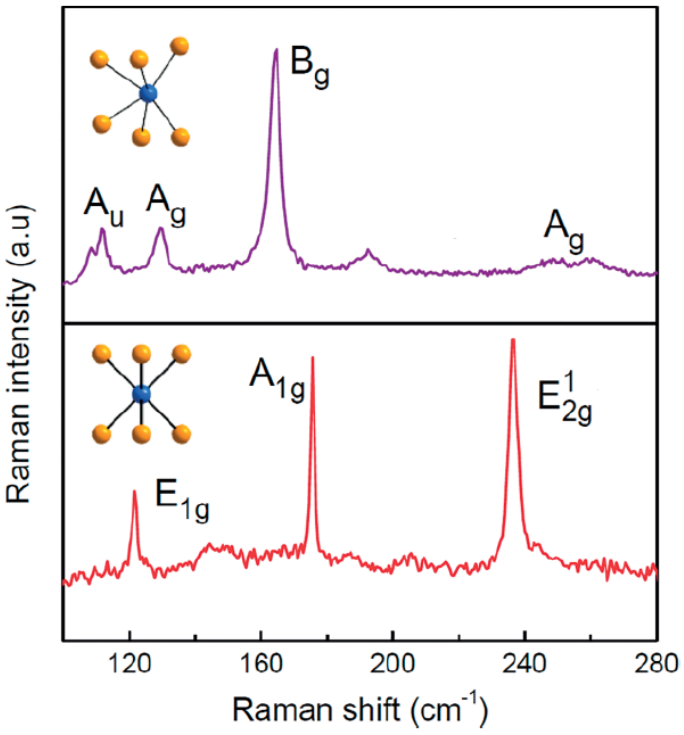

Figure 1.12: Raman Spectra of 2H and 1T' $MoTe_2$

1.4 Applications

- **Electronics applications**

  2D group VI TMDs are outstanding candidates for next-generation electronics and optoelectronics devices relying on ultimate atomic thickness. Although large-scale and defect-free TMDs on the desired substrate is still challenging, new growth techniques are developing. Atomically-thin field-effect transistors (FETs) based on the sulfides and selenides of Mo and W have demonstrated significant current modulation, and moderate carrier mobilities [27]. In contrast, semiconducting $2H - MoTe_2$ remains relatively underexplored, despite moderate indirect band gaps $E_G \approx 0.88$ to 1.0 eV in bulk crystal, and direct $E_G \approx 1.1$ eV (optical) and 1.2 eV (electronic) in monolayers, similar to bulk silicon [28]. Such moderate band gaps may facilitate low-power transistors with tunable injection of either electrons or holes, enabling low-voltage complementary logic and optoelectronics in the visible-to-infrared range [29] [30]. Despite these favorable properties, ambient degradation limits the broader exploitation of $MoTe_2$ electronic devices. Reference [28] reported the fabrication of air-stable, n-type transistors with the highest drive currents for this layered semiconductor (Figure 1.13). The figure below also shows the low temperature I_D vs. V_{DS} sweep of a typical fewlayer, short channel device, achieving record saturation current density of 420 $\mu A/\mu m$ at 78 K.

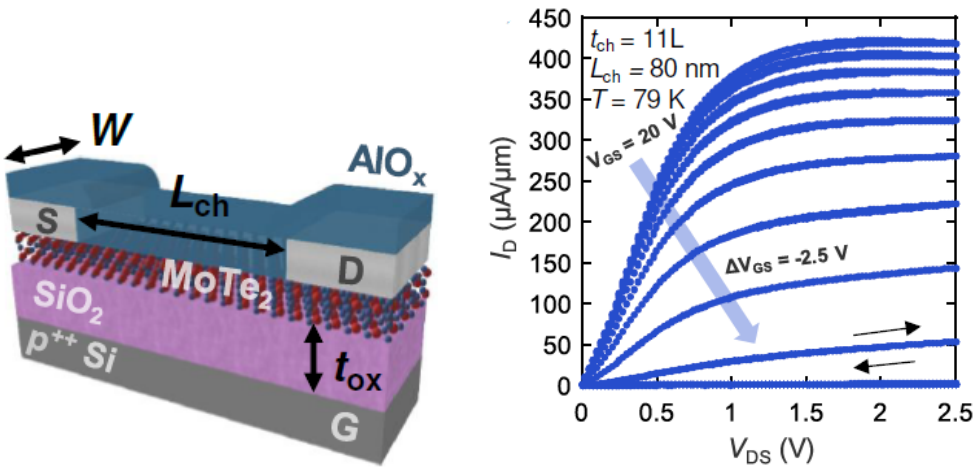

Figure 1.13: Schematic of AlO_x-encapsulated $MoTe_2$ FETs (left) - Measured I_D vs. V_{DS} curves of $MoTe_2$ FET (right) [28].

- **Optoelectronics applications**

  Since most mono-layer TMDs are direct bandgap semiconductors whose bandgap can be tuned by chemical processes and the metal and the chalcogen species, they have drawn the interest for optoelectronics and flexible optoelectronics. The mono-layer molybdenum ditelluride is a direct gap semiconductor, so it is suitable for optoelectronic applications. In [31] Lein et al. reports a high-performance ultrathin ambipolar $MoTe_2$ phototransistor. This phototransistor exhibits very high responsivity up to 2560 A/W at V_{gs}=80 V, which is higher than that of most other TMDs.

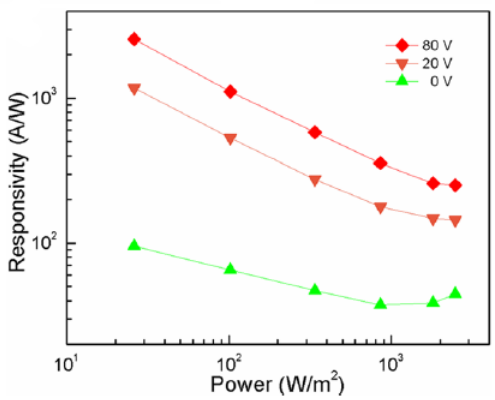

Figure 1.14: Responsivity of $MoTe_2$ phototransistor change with the laser power at different gate voltages.

- **Energy storage applications**

  TMDs have been studied as electrode materials in Li-ion batteries because lithium ions can be easily intercalated in and extracted from their layered structure. While bulk TMDs show structural instability when intercalated with Li-ions and are characterized by low energy density and average voltage, their nanosheets do not suffer from this structural instability. Among the TMDs, the molybdenum ditelluride is appealing because in the 1T'-phase, it is a layered conductor and the vacancies of tellurium play a significant role in enhancing the efficiency of the Li^+ diffusion. Moreover, it can be combined with graphene networks to prevent $MoTe_2$ aggregation and enhance overall conductivity. In reference [32] the $MoTe_2$ nanosheets encapsulated in few-layer graphene have been fabricated. It exhibits excellent electrochemical performance with high specific capacity of 574 $mAhg^{-1}$ after 400 cycles at 0.5 Ag^{-1} with a 99.5 % retention capacity.

- **Valleytronics applications**

  The Valley is referred to a local minimum in the conduction band or a local maximum in the valence band. In addition to charge and spin, an electron is also endowed with a valley degree of freedom, which specifies the valley that the electron occupies. The possibility of using the valley degree of freedom to store and carry information leads to conceptual electronic applications known as valleytronics. traditional semiconductors were among the first materials that have been investigated for the valleytronics applications. Early works investigating the valley degree of freedom date back to the 1970s, with studies of inversion layers occurring at silicon/insulator interfaces [33].
  The prominent feature of TMDs that leads to different applications in valleytronics is the lack of inversion symmetry, valance bands are split by spin-orbit coupling. The spin–orbit interactions split the spin degeneracy at each valley and lock the spin and valley pseudospin degree of freedom, the spin-up state at the K valley is degenerate with the spin-down state at the K' valley. This degeneracy can be lifted by applying an out-of-plane magnetic field to break the time-reversal symmetry. In bilayer and bulk TMDs, where inversion symmetry is restored, the spin degeneracy at each valley is reinstated.

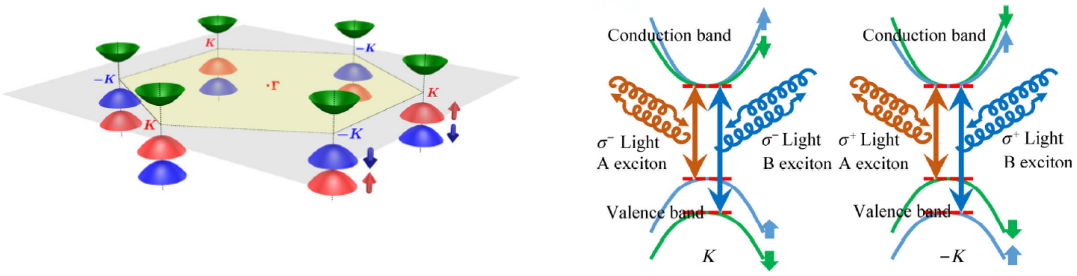

Figure 1.15: Band structure at the band edges located at the K points[34] (left). The optical selection rules in valleytronics (right).

The broken inversion symmetry in monolayer TMDs yields finite Berry curvatures Ω (effective magnetic fields in momentum space) and orbital magnetic moments m (arisen from the self-rotating motion of the electron wavepacket) of opposite sign at the K and the K' valleys [35]. Right (left)-handed circularly polarized light only couples to the K (K') valleys according to the optical selection rules.

- **Catalysis applications**

  The development of novel and efficient catalysts for renewable hydrogen generation has brought much interest since H_2 is regarded as an excellent energy source due to its large energy density and being environmental-friendly [36]. $MoTe_2$ is considered as a promising catalyst for the hydrogen evolution reaction (HER) owing to its abundant active sites such as atomic vacancies and step edges [37]. The hydrogen evolution reaction is through: $2H^+ + 2e^- \rightarrow H_2$.

  However, to date, there are very few reports of tellurides in this context, and none of these transition metal telluride catalysts is especially active [38]. It is reported that the monoclinic metallic phase of molybdenum telluride, $1T' - MoTe_2$ is a promising catalyst for the hydrogen evolution reaction, The stable metallic $1T' - MoTe_2$, allowing efficient charge transfer at the surface, would be promising for the HER. This contrasts with the electrocatalytic activity displayed by the semiconducting $2H - MoTe_2$ polymorph, which was found to be largely catalytically inert. Reference [38] also explains how electron doping under an applied reductive bias, and associated adsorption of hydrogen on specific Te sites in the material drives a distortion of the $MoTe_2$ structure, which gives a more active catalyst as long as H remains adsorbed to the surface.

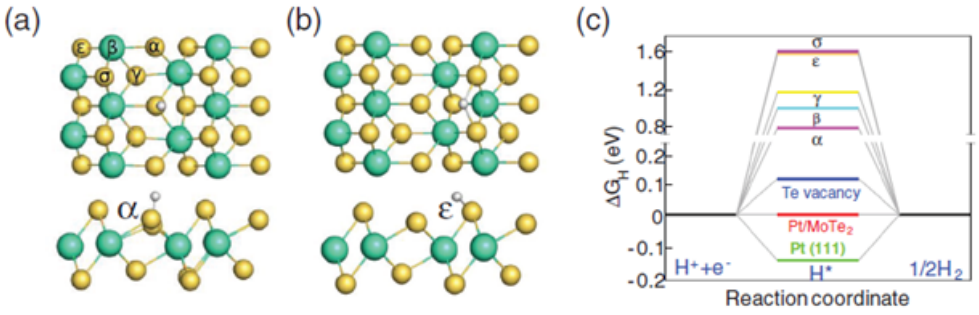

Figure 1.16: (a) hydrogen-adsorbed $MoTe_2$ at an α site (b) hydrogen-adsorbed $MoTe_2$ at an ϵ site (c) Comparison of free-energy at various H-bonding sites [39].

Chapter 2

Methodology

2.1 Deposition Methods

Aiming at the technological exploitation of 2D materials, the development of approaches to synthesize large-scale and high-quality films is mandatory. Many studies report on the synthesis of ultrathin crystals but with limited lateral extension (in the micrometer range) using mechanical and chemical exfoliation, or solution-based chemical approaches [40]. Compared with other group VI TMD materials, stoichiometric $MoTe_2$ films are more challenging to achieve. The electronegativity difference between Te and Mo is much smaller (0.3 eV) among these materials. Therefore, the bonding energy of Mo-Te bonds is relatively small, which translates to less tendency for the material formation and difficulty to obtain stoichiometric $MoTe_2$ [41]. Controlled growth of $MoTe_2$ in 2H or 1T' phase is very important to achieve high quality results. There are some limitations for the growth of 1T'-$MoTe_2$ because of its metastable nature. Therefore, synthesizing pure 1T' phase is challenging. There are various methods to grow $MoTe_2$ such as: Mechanical Exfoliation, Chemical Vapor Deposition and Molecular Beam Epitaxy.

2.1.1 Exfoliation

The easiest way to obtain clean $MoTe_2$ single crystals due to the weak van der Waals bond between the layers is mechanical exfoliation. It was also the first method to isolate a monolayer of graphite in 2004 by using scotch tape. However, this method does not imply control over the flakes' thickness, shape, or size, resulting in low yield. The different steps of the mechanical exfoliation approach are sketched in Figure 2.1. The scotch tape is pressed to the tape; see panel a in Figure 2.1. Then the scotch tape is pressed against the surface of the $MoTe_2$ rocks. Therefore, the top few layers will attach to the tape. The tape with crystals of $MoTe_2$ will

attach to the desired surface and press against it. The bottom layers will remain on the surface upon peeling off the tape.

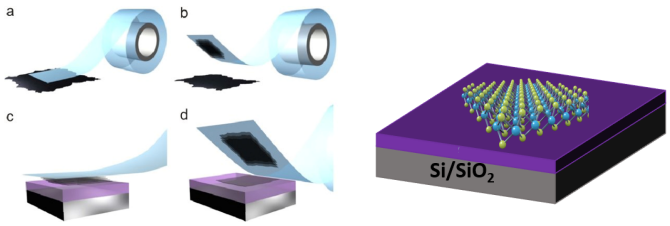

Figure 2.1: The process of mechanical exfoliation

Although this method is standard to prepare $MoTe_2$ flakes, it is not suitable for mass production. In addition, small obtained areas with this method are another limiting factor. As an alternative, **Liquid Exfoliation** based on mixing and dispersing materials in solution allows for the production of $MoTe_2$ flakes with a controllable thickness. The solvent has a vital role in defining the thickness of the flakes. It is typically done by using Li intercalation, but the drawback is the phase transition from 2H phase to 1T and the small size of the flakes. In the figure below, the process is indicated. The bulk material is used as a cathode in the electrochemical bath, and lithium foil as an anode provides lithium ions. Then, under discharge mode, a lithium intercalation process was done, and the rinsing procedure isolated the intercalated compound.

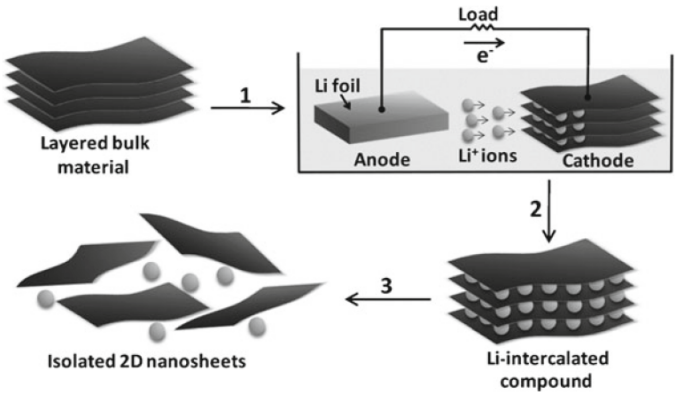

Figure 2.2: The process of liquid exfoliation[42]

2.1.2 Chemical Vapor Deposition

Chemical vapor deposition (CVD) is one of the best candidates aiming at a deposition of ultrathin films of transition metal ditellurides, tellurium, and their heterostructures on a large scale (centimeter scale) [43].

CVD is the process of chemically reacting a volatile compound of a material to be deposited with other gases to produce a nonvolatile solid that deposits atomistically on a suitably placed substrate. It belongs to the class of vapor-transfer processes, which is atomistic, as the deposition species are atoms or molecules or a combination of these. This technique has several advantages: high reliability and flexibility, good step coverage, and conformality in the deposition of thin films, which is crucial for filling high aspect ratio trenches such as in integrated circuit processing.

A CVD reaction is governed by thermodynamics, which is the driving force that indicates the direction the reaction is going to proceed (if at all), and by kinetics, which defines the transport process and determines the rate-control mechanism, in other words, how fast it is going. The process of CVD can be exploited in various processes such as atmospheric pressure CVD, low-pressure CVD (when the pressure is less than ambient), laser CVD, plasma-enhanced CVD (when plasma enhances the decomposition), photochemical vapor deposition, chemical vapor infiltration, and chemical beam epitaxy [44]. The discussion of the CVD in this work is based on atmospheric-pressure CVD.

Depending on the Mo-based precursor state of matter (gas or solid), there are two CVD processes: *Co-deposition* and *Tellurization*. If the Mo precursor reacts in the vapor phase with Te vapors, the process is co-deposition. If Mo reacts in the solid phase (pre-deposited Mo film) with Te vapor, the process is called Tellurization. Direct tellurization CVD has emerged as a viable technique for achieving continuous and high-area growth of $MoTe_2$. The process relies on a reaction between Te vapor and an atomically thin seeding layer (commonly Mo-metal) pre-deposited on a substrate. Although two polymorphs of $MoTe_2$ (2H and 1T') make controlling the reaction outcome difficult, it is possible to reach a specific polymorph by optimizing the reaction condition.

The CVD system that has been exploited is consists of a two-inch quartz tube and two furnaces. The temperature in each furnace can be set and controlled independently. The upstream furnace contains Te powders (150 mg) inside an Alumina boat with 2×2 cm Si Substrate covers. The Mo substrate $4 \times 1cm^2$ is inserted in the downstream furnace in a quartz boat covered on top. A mixture of $Ar/H_2(4\%H_2)$ gas is introduced into the furnace as a carrier gas for the whole process. The quartz tube is initially pumped down to 760 Torr and purged with N_2 gas to remove air contamination. The growth procedures are as follows: (1) pre-

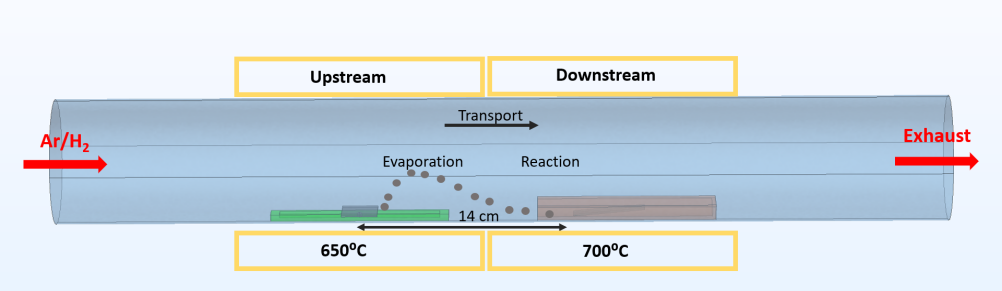

Figure 2.3: Schematic representation of two-furnace CVD apparatus with boats and precursors

heating for 10 minutes at $50°C$, meanwhile 10 sccm of N_2 gas flows. (2) Ramp the temperature up to $600°C$ at both furnaces in 15 minutes. (3) Ramp the upstream and downstream temperature to $650°C$ and $700°C$ in 120 minutes, dedicated to the growth process. The mixture of 100 sccm Ar/H_2 with 60 sccm of N_2 will flow as the carrier gas. (4) Cooldown temperature for 120 minutes by using 500 sccm Ar gas.

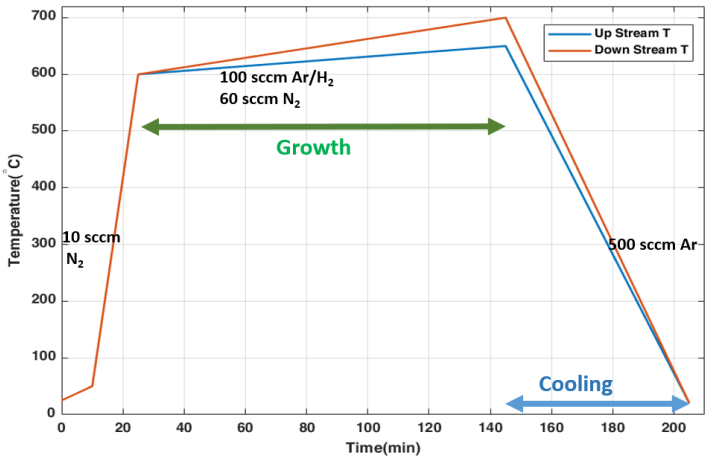

Figure 2.4: The time ramp used for the growth

In this thesis, Planartech Chemical Vapor Deposition (CVD) at CNR-IMM, Agrate Brianza has been employed to prepare the growth of two-dimensional transition metal dichalcogenides .

Figure 2.5: Fully automated CVD system for 2D-TMD growth at the MDM lab [45].

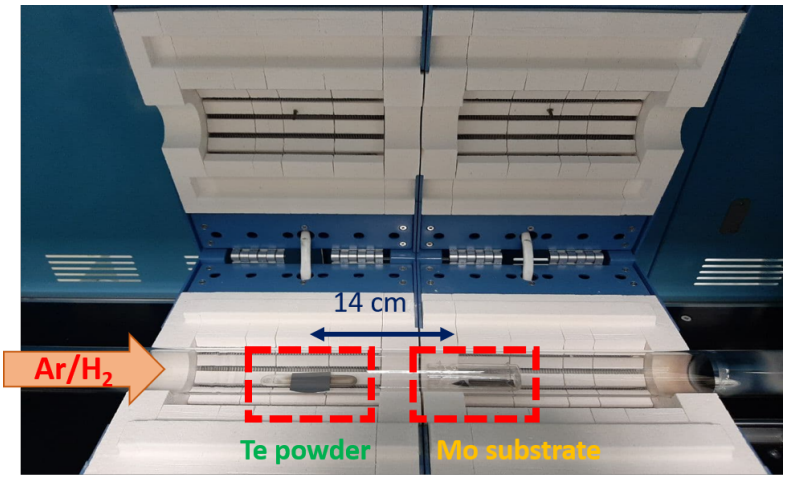

Figure 2.6: The CVD system with the boats, Te powder source, and Mo substrate.

2.2 Characterization Methods

2.2.1 Raman Spectroscopy

Raman scattering is a powerful light scattering technique used to diagnose the internal structure of molecules and crystals. In a Raman light scattering experiment, the light at a known frequency and polarization impinges on a sample. The large majority of generated photons are scattered elastically. The scattered photons have the same energy, i.e., frequency, as the incident photons, and this scattering process is regarded as Rayleigh scattering.

However, a low portion of the light is scattered (approximately 1 in 10^7 photons) at optical frequencies lower (or higher) than the incident photons frequency. The difference in the energies of the incident and scattered photons is attributed to the energy required to excite the molecule to higher vibrational modes. After scattering, the molecule will be in a different rotational or vibrational state. This process is inelastic scattering which is called Raman scattering.

To keep the system's total energy constant after attaining a new roto-vibronic state, the scattered photon shifts to different energies, i.e., different frequencies. The photon is shifted to lower frequencies if the final state is higher in energy than the initial state so that the total energy will be the same; this lowering of frequency is called the Stokes shift. In opposite to Stokes shift, if the energy of the final state is lower than the initial state, the frequency shifts to higher-value so-called Anti-Stokes shift [46].The schematic of both Stokes and Anti-Stokes shift is given below:

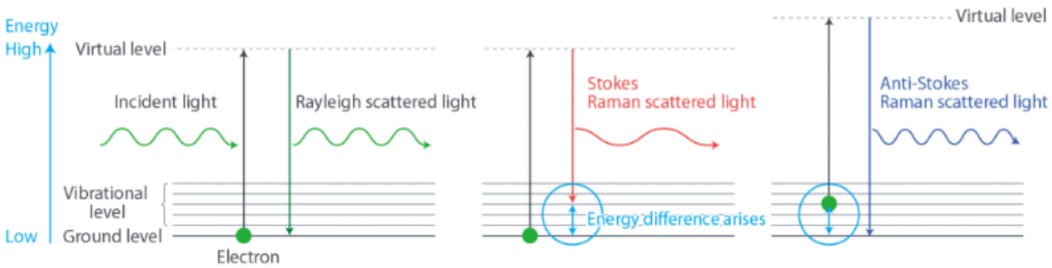

Figure 2.7: Comparison between Rayleigh and Raman scattering processes.

The oscillating electric field of the incident monochromatic electromagnetic radiation interacts with the molecule's electron cloud to create an induced dipole moment depending on its polarizability. There should be a change in its dipole-dipole polarizability concerning the rovibronic states associated with any molecule to exhibit Raman Effect. The intensity of Raman scattering is directly proportional to the change in the polarizability of the molecule giving Raman signal [47]. As a result, we can expect a very intense peak in the Raman spectrum when strong distortion in the electron cloud is induced by electromagnetic radiation. The specific vibrational mode of each molecular functional group is given by identifying the peak position. We can say that the Raman spectrum gives the "molecular fingerprint" of the sample. The peak intensity provides information about the crystallinity of the material also. Raman shift is usually given in wavenumbers as a function of incident and scattered photon wavelength. This "Raman shift" is an intrinsic property of the sample. This expression relates the spectral wavelength and wavenumbers of Raman shift [48]:

$$\nu = \frac{1}{\lambda_{incident}} - \frac{1}{\lambda_{scattered}} \tag{2.1}$$

Where ν is the Raman shift in wavenumber.

In this thesis, the Ex-situ Raman characterization is performed using a Renishaw InVia Raman Spectrometer in z-backscattering geometry attached with Leica optical microscope installed in MDM lab see Figure 2.8. It is equipped with 2.41 eV / 514 nm continuous wave Diode – Pumped Solid State (DPSS) RL514C Class 3B and a Renishaw RM1000 spectrometer, which is equipped with 1.96 eV / 613 nm (He-Ne laser) were used as excitation wavelengths [49].

Figure 2.8: Renishaw InVia Raman Spectrometer at MDM Lab.

The laser focuses on the sample by using a 50X 0.75 N.A. Leica objectives. An optical grating of 2400 lines/mm separates the wavelengths in the Raman signal and is detected utilizing a Charge Coupled Device (CCD) detector. The acquired signal is analyzed by using the software WiRE Interface 3.3 supplied by Renishaw. The power at the sample is maintained in the range of 1 – 10 mW by using optical filters to prevent laser-induced sample heating.

Raman Study on Mechanical Exfoliated 2H and 1T' Flakes

In my experimental activity, I explored the mechanical exfoliation method on commercial $MoTe_2$ stones (SPI supplier) both in the 1T' and 2H phases. Using this method, I obtained flakes with micrometer lateral size that I used to characterize the Raman modes of the molybdenum ditelluride material and familiarity with the Raman spectroscopy and AFM techniques. In this section and next, I will summarize the main measurements carried out on the flakes. Moreover, I will point out the main results on the flake characterizations that will also be useful for understanding the experimental evidence on the grown material presented in the following chapters.

The Raman spectra collected by green laser from 2H $MoTe_2$ stone by mechanical exfoliation are reported below. The laser power is set at 1% for 15 accumulations to avoid modification in the sample. The Raman active vibrations of 2H phase are: A_{1g} mode at 172 cm^{-1} and E^1_{2g} mode at 233 cm^{-1}. The Raman spectra are fitted by Voigt function, and the fitting parameters, including FWHM, intensity, and area of each peak, are summarized in Table 2.1.

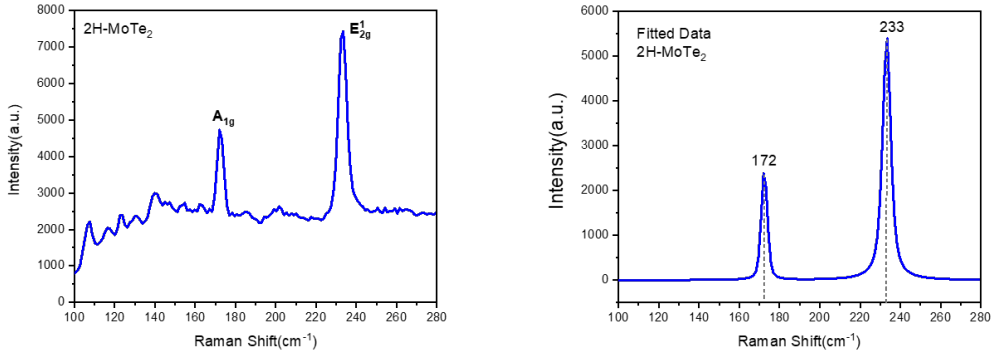

Figure 2.9: Green Raman (514 nm) spectra of mechanically exfoliated 2H $MoTe_2$ raw data (left) and fitted data (right).

Parameters	A_{1g} Peak	E^1_{2g} Peak
FWHM (nm)	3.59	4.89
Intensity (a.u)	2428	5431
Area $(a.u.(cm)^{-1})$	10942	37763

Table 2.1: FWHM, Intensity, and area of the Raman A_{1g}, and E^1_{2g} peaks of 2H mechanical exfoliated flake.

The Raman spectra collected from 1T' $MoTe_2$ stone is reported here. The observed Raman modes corresponding to the 1T' phase are A_u mode at 111 cm^{-1}, A_g at 128 cm^{-1}, B_g mode at 163 cm^{-1}, B_g mode at 191 cm^{-1} and A_g mode at 260 cm^{-1}. The Raman spectra is fitted by Voigt function and the fitting parameters of the 1T' flake are summarized in the Table 2.2.

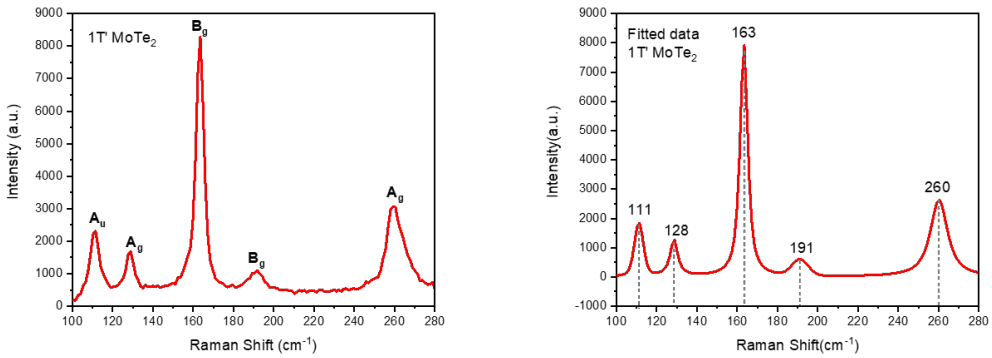

Figure 2.10: Green Raman (514 nm) spectra of mechanically exfoliated 1T' $MoTe_2$ raw data (left) and fitted data (right).

Parameters	A_u Peak	A_g Peak	B_g Peak	B_g Peak	A_g Peak
FWHM (nm)	4.74	4.52	4.58	8.10	9.34
Intensity (a.u)	1849	1277	7890	604	2658
Area $(a.u.(cm)^{-1})$	11301	8252	53750	4640	43345

Table 2.2: FWHM, Intensity and area of the Raman A_u, A_g, B_g, B_g, and A_g peaks of 1T' Mechanical exfoliated flake.

2.2.2 Atomic Force Microscopy

The atomic force microscopy (AFM) technique provides another opportunity to gain a topographical understanding of the sample. Atomic force microscopy is a technique that allows to see and measure surface structure with high resolution and accuracy. An AFM image can shows the arrangement of individual atoms in a sample, or to see the structure of individual molecules. Unlike optical or electron microscopes, it doesn't focus light or electrons on to a surface. The advantages of AFM could be magnification in X, Y and Z axes, high X-Y resolution and minimal sample preparation.

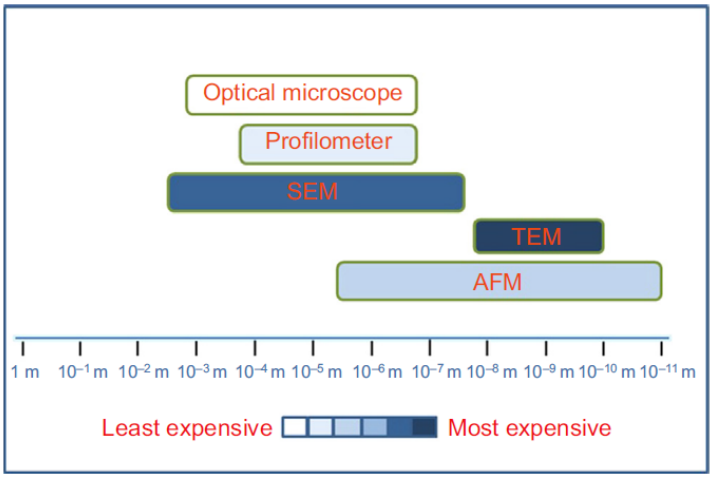

Figure 2.11: Comparison between length scales measured by different microscopes

The length scales of AFM and Optical microscope has an overlap, which makes it possible to do combination of both field of views. It is also possible to do comparison between AFM, SEM and TEM since the length scales are similar. However, the resolution of SEM is smaller (5nm) than AFM (0.1nm), but the TEM resolution is similar to AFM.

The other advantage of this technique is high accuracy in positioning of the probe above the sample surface which make it a promising technology for manipulation of samples at nanoscale. The other advantages of AFM are the possibility to provide 3D information on the sample surface and performing the measurement of sensitive materials in their operating environment. The surface imaging with TEM and SEM requires to samples to be in a vacuum and sometimes preparation to ensure electrical conductivity, but the AFM measurement doesn't necessarily needs these conditions.

Principles of AFM technique

AFM somehow "feels" the sample surface by using a sharp probing tip. While the probe scans a surface of a sample, the contact force between the probe tip and the surface being scanned leads to a small elastic deflection of the micro-cantilever.The atoms response to the developed van der Waals force could be short-range repulsive interactions or longer-range attractive, depending on the type of contact.
The probing tip will continuously build up a map of the height or topography of the surface as it goes along.

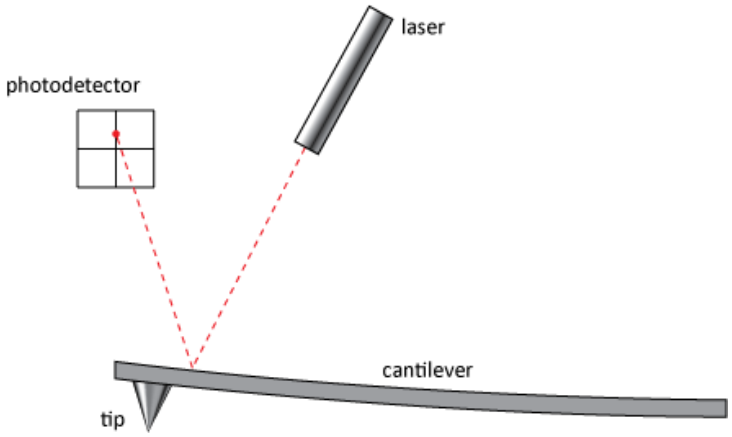

Figure 2.12: A schematic of AFM set-up and Cantilever Deflection [50].

- *Piezoelectric transducers* are used for controlling the motion of the probe as it is scanned across the sample surface. They are electromechanical transducers that convert electrical potential into mechanical motion in the presence of the voltage gradient. The inverse of piezoelectric effect is employed for z-scanner measurements. Typically, the millivolt-regime control of applied bias corresponds to sub-Angstrom control of Z displacement. It is worth to mention that piezoelectric scanners are nonlinear devices and have some problematic behaviors such as: hysteresis (irreversibility), creep (time dependance) and aging [51]. Furthermore, the x-y piezoelectric elements are used to scan the probe across the surface in a raster-like pattern.

- *Cantilever with integrated tip* is utilized in AFM instrumentation as force transducer. It measures the force between the tip and surface when it comes near the sample. The cantilevers could be in different shapes depending on the applications. The two common shapes are rectangular and V-shapes that are indicated in the figure below [52].

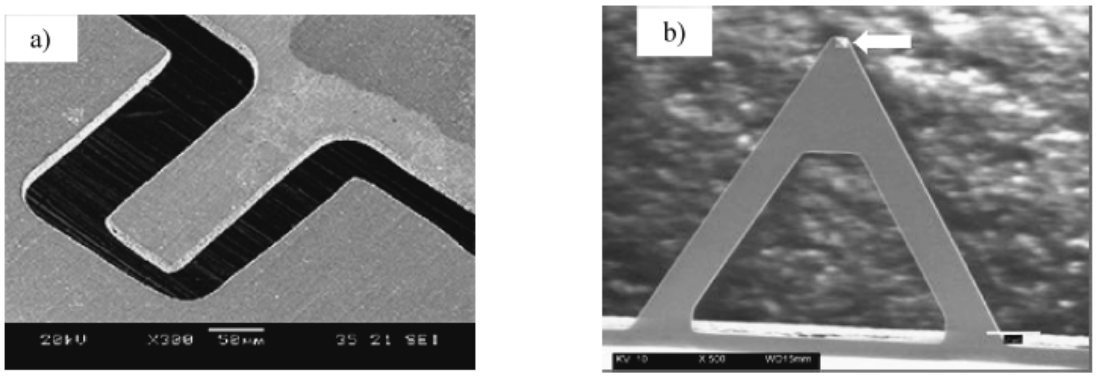

Figure 2.13: a) SEM image of rectangular cantilever - b) SEM images of a V-shaped cantilever (right).

- *Feedback control* has an important role to maintain a sufficient distance between the tip and surface. It takes the signal from force transducer and use it to control the expansion of the z piezoelectric transducer.

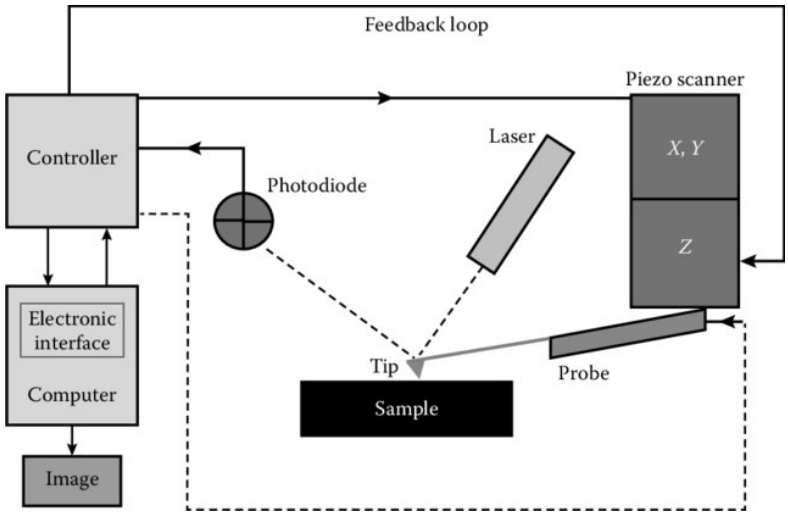

Figure 2.14: Block diagram of AFM operation.

AFM modes

- *Contact mode* It's a simple mode conceptually and it is used when the sample surface is not stiffer than the tip. It is the fastest mode with capability of obtaining high resolution images. The probe touches the sample surface all the time. Due to the repulsive van der Waals force the cantilever deflects and an image of the surface is obtained. The feedback circuit continuously adjusts the cantilever height to maintain a constant force. A detector monitors the deflection and the resultant force is calculated using Hooke's law.

$$F = -k \times D \tag{2.2}$$

With F = force (N), k = probe force constant (N/m) and D = deflection distance (m).

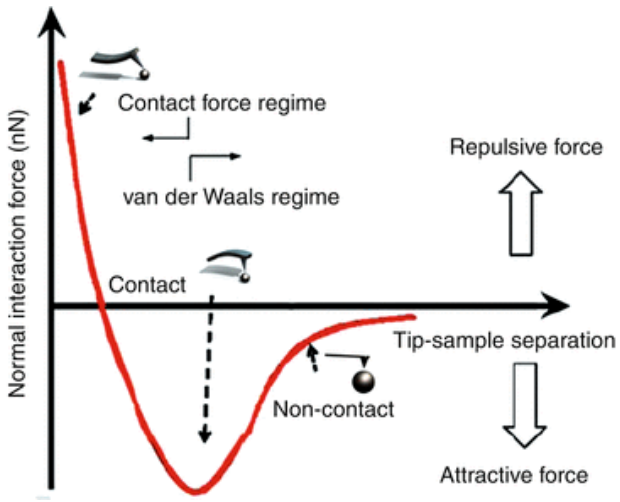

Figure 2.15: Force–distance curve of AFM operation.

- *Oscillating or tapping mode* An oscillating input signal is applied to the cantilever to make the probe vibrate up and down. In tapping mode, the cantilever makes intermittent contact with the surface at a resonant frequency. The actual movement of the probe will depend on its interaction with the sample surface. The tip-sample interaction passes from the 'zero-force regime, through the attractive regime, and the repulsive regime. The resulting oscillation in the cantilever deflection is measured and compared to the input oscillation to determine the forces acting on the probe.

- *Non-contact mode* In non-contact mode, the AFM cantilever and sample surface do not come into contact. The cantilever vibrates very near the sample surface at a frequency higher than its resonant frequency. The probe can oscillate within the attractive regime only. In this mode, there is a change in the cantilever resonant frequency which is caused by forces from the surface (attractive van der Waals forces) acting on the tip. The resonance frequency far from the surface is given by:

$$\omega_0 = c\sqrt{k} \tag{2.3}$$

Where k is the spring constant. The new resonance frequency due to the additional forces from surface is given by:

$$\omega_0' = c\sqrt{k - f'} \tag{2.4}$$

Where f' is the derivative of the force normal to the surface.

2.2.3 Electrostatic Force Microscopy

Electrostatic Force Microscopy (EFM) represents the electric properties on a sample surface by measuring the electrostatic force between the surface and a biased AFM cantilever. By changing the surface, electrical properties such as surface potential and charge distribution, the interaction force between the tip and surface will be modified and deflect the cantilever. The constant voltage U_0 and the variable voltage $U_1 sin\omega t$ are applied between the tip and the sample, and $\phi(x, y)$ is the potential distribution on the sample. So:

$$U = U_0 + U_1.sin(\omega t) - \phi(x, y) \tag{2.5}$$

The tip-sample capacity would be:

$$E = \frac{CU^2}{2} \tag{2.6}$$

According to the $F = -\nabla E$, the z-component of the electric force acting on the tip would be:

$$F_z = -\frac{\partial E}{\partial z} = -\frac{1}{2}U^2\frac{\partial C}{\partial z} = -\frac{1}{2}[U_0 + U_1.sin(\omega t) - \phi(x, y)]^2\frac{\partial C}{\partial z} \tag{2.7}$$

Since the value of $\partial C \partial z$ depends on the tip-sample distance, so a two-pass technique is introduced to measure each scan line. In the first pass close to the surface, the cantilever oscillations are excited by the piezo-vibrator with a frequency close to the resonant frequency. Then the probe will lift to the distance h from the surface and scan the surface at a constant height. So at this height, the changing of the local dielectric properties of the surface will lead to the change in the cantilever oscillation amplitude and phase.

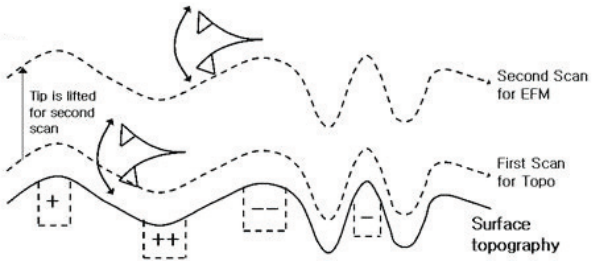

Figure 2.16: Schematic of the two-pass technique in EFM.

EFM study on the mechanical exfoliated flakes

The mechanical exfoliation technique (described in section 3.1) was used to obtain 2H and 1T' phases of $MoTe_2$ flakes from bulk crystals. Indeed, the exfoliated flakes are transferred onto a conductive substrate to characterize their electrical properties using the electrostatic force microscopy method. I used a conductive substrate in which the gold was deposited on top of Si/SiO_2 substrate in the MDM lab by DC sputtering. The sketch below describes the capacitive coupling (C_1) between the sample and conductive tip. The induced charges at the AFM tip in response to the applied voltage bias is Q'.

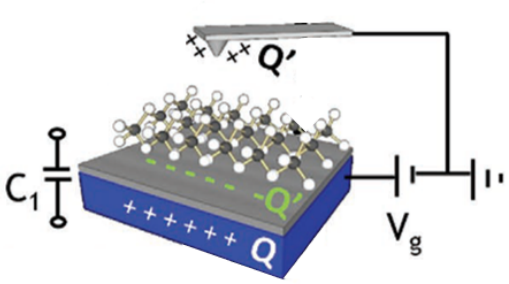

Figure 2.17: Experimental configuration of the EFM measurements [53].

In the EFM measurements, the phase shift due to the electrostatic force on the tip resulted:

$$tan\phi = -\frac{Q}{2k}C_1''(z)V_{tip}^2 \tag{2.8}$$

In this equation, $Q = \frac{f}{\Delta f} = 120$ and $k = 120\frac{N}{m}$ are quality factor and spring constant of the cantilever respectively. C_1'' is the second derivative of the electrical capacitance between the conductive AFM tip and flakes as a function of the lift height (z) [53]. The AFM tip can be modeled as a parallel plate of radius R at a distance z above the substrate.

The EFM measurements were carried out in a dual-pass scan. In the first scan, the topography was acquired with the tip electrically grounded, in the second scan, the phase signal was acquired withdrawing the tip at a lift height of 20 nm above the surface. The voltage ramp that is applied between the tip and sample varies in the range of 1-5 V.

As predicted by Equation 2.8, the variation of $|tan\phi|$ has parabolic relation with the applied voltage to the tip (Figure 2.18). The minimum of the $|tan\phi|$ (vortex) means that the surface potential of the tip and flakes are equal and the voltage of the vortex can correspond to the contact potential difference. By collecting the phase data during the backward pass and performing average on them, we can make a plot of $|tan\phi|$ with respect to the applied voltage to the tip. As we can see, the vortex of the parabola has a minor shift toward lower voltages in the 2H flakes.

1T'	R-square	**2H**	R-squre
25 nm	0.87	25 nm	0.74
35 nm	0.90	46.5 nm	0.95
60 nm	0.87	76.5 nm	0.80

Table 2.3: Reported R-square parameter for the polynomial fitting used in the Figure 2.18.

From the fit of the EFM measurements, I calculated the values reported in Table 2.4 for the second derivative of the electrical capacitance as a function of the flakes thickness and allotropic phase:

1T'	C_1''	**2H**	C_1''
35 nm	8.51×10^{-4}	46.5 nm	9.25×10^{-4}
60 nm	6.9×10^{-4}	76.5 nm	10.99×10^{-4}

Table 2.4: Calculated second derivative of capacitance along two different heights of 1T' and 2H Flakes.

Note that in 2D materials, the confined nature of the atomically thin layer poses serious concerns on the physical definition of the dielectric constant. In this scenario, the local electronic polarizability has been proposed as the fundamental variable to describe the dielectric properties of the 2D materials [54]. It is therefore interesting to use the EFM measurements to study the dielectric properties of the flakes. Indeed, we can use the calculated second derivative values of the electrical capacitance to derive the dielectric constant associated with the $MoTe_2$ flakes.

Following the model derived in [55], we can relate the second derivative of the electrical capacitance to the dielectric constant of the material according to the equation:

$$C_2''(h) = \frac{8\pi R^2 \epsilon_0}{\gamma^2} \frac{1}{(h + D/\epsilon + t/\epsilon_s)^3} \tag{2.9}$$

Where the $C_2(h)$ is the total capacitance of tip-sample-substrate, D is the thickness of the flake, ϵ is the dielectric constant of the flake that we want to derive, and

$$\gamma = ln(\frac{1 + cos\theta}{1 - cos\theta}) \tag{2.10}$$

is a constant factor that depends on the half-angle θ of the AFM tip. Equations 2.9 and 2.10 contain the following constants: $\epsilon_0 = 8.854 \times 10^{-12} F/m$ is the vacuum permittivity, R = 10 nm, and $\theta = 20°$.

From equation 2.9, I obtained that the mean value of the dielectric constant for the flakes in the 1T' phase is 7, while the 2H phase is slightly higher 7.84. Note that analysis is limited to a restricted statistical set of measurements and flakes with a relatively high thickness. Even though the EFM showed the potential to study the dielectric properties of the material at the nanoscale, further investigations should consider lower thicknesses down to the monolayer limit in order to prove the validity of the dielectric constant as a valuable physical quantity for 2D materials.

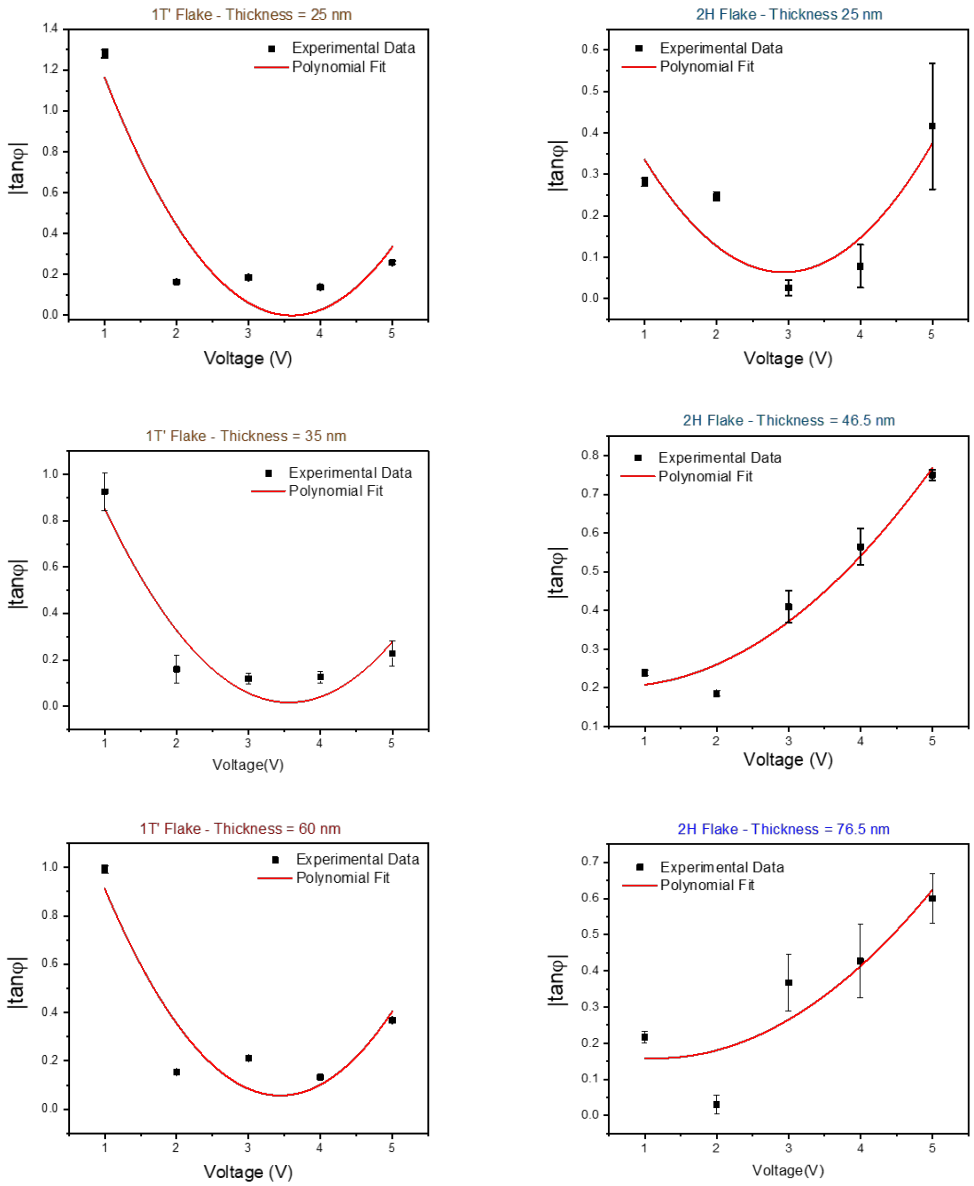

Figure 2.18: Plot of the $|tg(\phi)|$ function for the applied voltage 1,2,3,4,5 V with the fitted data of 1T' and 2H flakes.

2.2.4 Kelvin-Probe Force Microscopy

The contact potential difference (CPD) between two materials depend on a variety of parameters like the work function, dopant concentration in semiconductors or temperature changes on the sample [56]. The Kelvin-probe method can be used in order to measure the CPD between the tip and sample.

$$V_{CPD} = \frac{\phi_{tip} - \phi_{sample}}{-e} \tag{2.11}$$

Conductive tip (cantilevers coated with platinum-iridium (PtIr)) and sample act as parallel plate capacitors with small space between them. Due to the difference in the Fermi energies of these two materials, an electric force will be generated. Workfunction can be defined as the minimum amount of energy needed to remove an electron from the Fermi level to the vacuum level. The figure below indicates that the conductive tip and sample close to each other but without electrical contact, and their vacuum levels align. When a wire connects these two materials, the electrons flow from the metal with the minor work function to the larger work function. Thus, it will shift the electronic levels, and it will continue until the electric field (between the positively charged sample and negatively charged tip) compensates for the work function difference. Now, the potential associated with the electric field equals the CPD between the metals. Then by applying a DC voltage to nullify the CPD, the surface charges will be eliminated in the contact area. KP measurements are only able to detect the CPD. In order to obtain the work function, KP needs to be calibrated against a surface with a known work function (e.g., Gold). During a KPFM measurement, a tip is passing above the sample at a constant height. Then, an AC voltage is applied to the cantilever. It creates an oscillating electrostatic force between the tip and sample that is measured by a lock-in amplifier. A DC offset voltage is then added to the AC voltage to cancel out the cantilever oscillation at the AC frequency. By mapping the applied DC offset voltage, a representation of the CPD emerges.

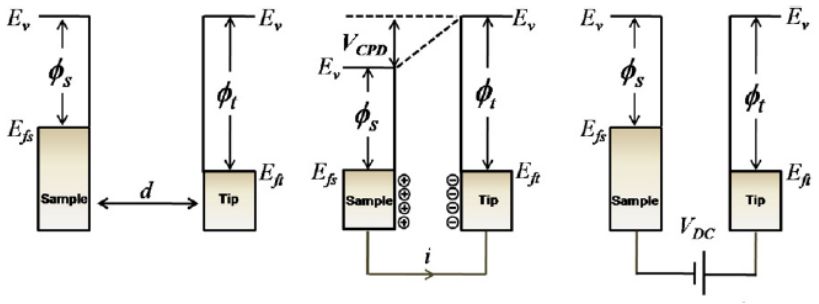

Figure 2.19: Schematic of the Kelvin Probe measurement [57]

KPFM study on the mechanical exfoliated flakes

In order to map the contact potential difference (CPD) of the tip and sample surface quantitatively, the KPFM method is exploited. We used Pt/Ir-coated cantilevers in noncontact mode, with a mechanical drive frequency of 76.57 kHz and an AC modulation of 2V. The topography and surface potential signal were measured simultaneously. By using the expression:

$$\phi_{sample} = \phi_{tip} - e * CPD \tag{2.12}$$

The work function of the tip can be driven from:

$$\phi_{tip} = \phi_{Au} + e * CPD_{Au} \tag{2.13}$$

The gold work function is assumed $\approx 5.1eV$ [58]. The calculated work function of the tip is substituted in the Equation 2.14 and the work function of the sample is obtained. By scanning the gold substrate, the CPD of the gold is driven to be $0.049eV$, and the work function of the tip is determined:

$$\phi_{tip} = 5.1eV + 0.049eV = 5.149eV \tag{2.14}$$

For calculating the sample work function, the CPD of the 1T' flake of 60 nm height with respect to the substrate is $0.069eV$. So the value of the work function calculated for this flake is:

$$\phi_{sample} = 5.149eV - 0.069eV = 5.08eV \tag{2.15}$$

This method is applied to the 2H and 1T' flakes with different heights to calculate the corresponding work functions. Table 2.4 summarized the value of work functions assigned to the different flakes heights.

1T'	ΔV	ϕ_{sample}	**2H**	ΔV	ϕ_{sample}
25 nm	3 mV	5.146 eV	25 nm	11.3 mV	5.137 eV
35 nm	4.1 mV	5.144 eV	120 nm	10.3 mV	5.138 eV
60 nm	6.9 mV	5.08 eV	260 nm	23.6 mV	5.125 eV

Table 2.5: Calculated work function along three different heights of 1T' and 2H Flakes.

The Figure 2.20 shows the flakes height that are measured at different points of the surfaces together with the CPD profiles. In panel a-b height profiles along

three different lines are depicted. Panel c-d represents that the potential variations along these scan lines are prportional to the thickness of the flakes. In particular, the potential of the 2H flake with 260 nm thickness is ≈ 25 mV and the potential of the gold substrate is ≈ 48 mV.

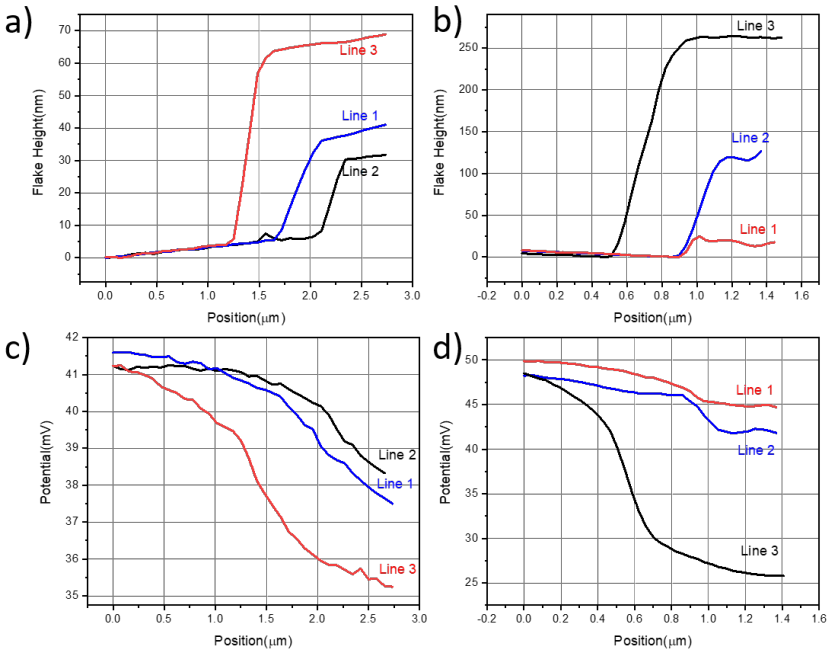

Figure 2.20: Height profile along three different lines of the a) 1T' flake b) 2H flake. Potential measured along the indicated lines in c) a. d) b.

In this thesis the samples studied by using AFM Bruker commercial system equipped with ultra sharp silicon probes (Figure 2.21).

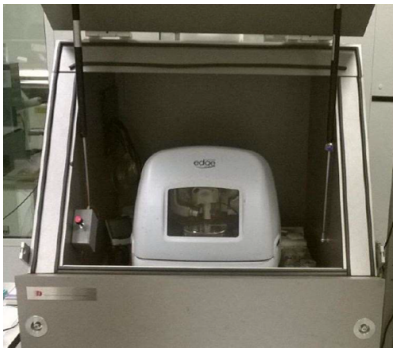

Figure 2.21: AFM Bruker commercial system at MDM lab.

The morphology and phase images are represented in Figure 2.22. The thickness of the 1T' flakes is measured along three different lines, which are 55, 35, and 25 nm. The thickness of the 2H flake along the two depicted lines is 65 and 50 nm.

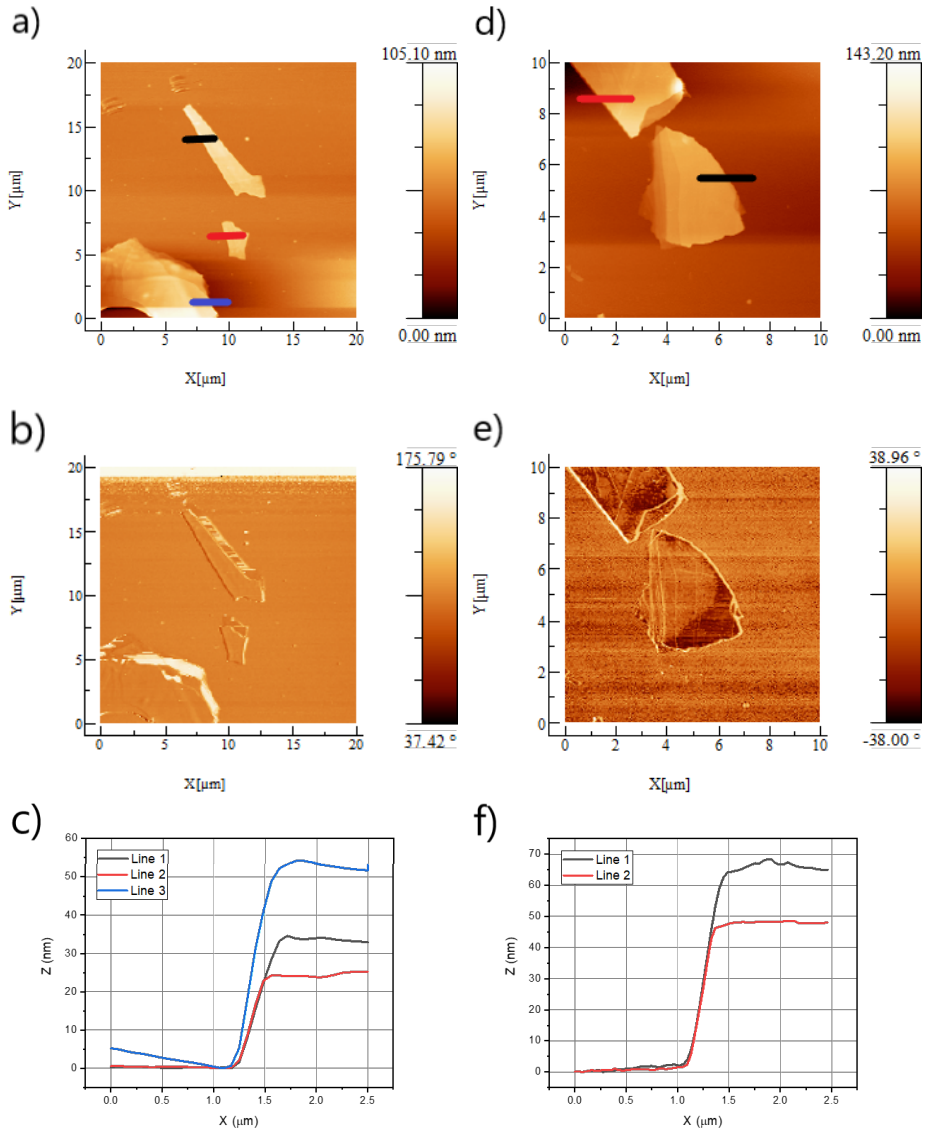

Figure 2.22: a) $20\mu m \times 20\mu m$ topographical image of the 1T' $MoTe_2$ b) Phase profile of 1T' $MoTe_2$ taken at V=3V c) cross-sectional plot along the three line in a. d) $10\mu m \times 10\mu m$ topographical image of the 2H $MoTe_2$ e) Phase profile of 2H $MoTe_2$ taken at V=4V f) cross-sectional plot along the three line in d.

2.3 Multiscale model for the growth chamber

This section illustrates the Finite Element Modelling (FEM) of a reactor for chemical vapor deposition (CVD). This multiscale model introduces a FEM growth chamber model for predicting the continuum level transport phenomena, including the laminar gas flow and flow-assisted Diffusion during CVD growth processes. In the Chemical species transport interface of COMSOL multiphysics, it is possible to simulate the laminar flow coupled to species transport in a gas or liquid by implementing "Reacting Laminar Flow, Diluted Species" multiphysics interface.

2.3.1 Model Definition

Modeling the growth chamber at a continuum level provides the spatial distributions of the precursor concentration, its gradient, carrier gas velocity, pressure, and temperature with a growth chamber. The developed model considers the flow of carrier and precursor gases and flow-assisted diffusion of precursor. The coupled governing equations are solved using FEM.

Governing Equations

- *Laminar Flow:* The gas flow rate is determined by solving the Navier-Stokes equation:

$$\rho\frac{\partial u}{\partial t} + \rho(u.\nabla)u = \nabla.[-p.I + \mu(\nabla u + (\nabla u)^T)] + F; \rho\nabla.u = 0 \tag{2.16}$$

  Where **u** is the velocity field, **p** is pressure, **I** is the unit matrix, μ is the dynamic viscosity, superscript T means matrix transpose, and **F** is the volumetric applied force, i.e., gravity. Furthermore, the density ρ is a function of temperature and precursor concentration in general. However, due to the low concentration of precursor in the gas phase, we have assumed ρ only to be a function of temperature.

- *Transport of Diluted Species:* The flow assisted diffusion of precursor materials is described by:

$$R = \frac{\partial c}{\partial t} + \nabla.(-D\nabla c) + u.\nabla c; N = -D\nabla c + uc; \tag{2.17}$$

  where R is the source term for precursor, c is the precursor concentration, D is the diffusion coefficient, and N is the flux of the precursor.

2.3.2 Modelling Instructions

This model combines the Laminar Flow and Transport of Diluted Species interfaces. The Reacting Flow, Diluted Species multiphysics coupling, is added automatically, couples fluid flow and mass transport. The fluid flow can either be free flow or flow in a porous medium. The mass transfer solves the development of one or several solutes dissolved in a gas or liquid solvent.

- **Configuration and dimension of chamber:**

  The length of the chamber is 140 cm, and its cross-section dimension is set at 5cm (which matches the actual dimension of our chamber) in this two-dimensional model. The position of the boats and substrate are also according to the real configuration in our CVD setup.

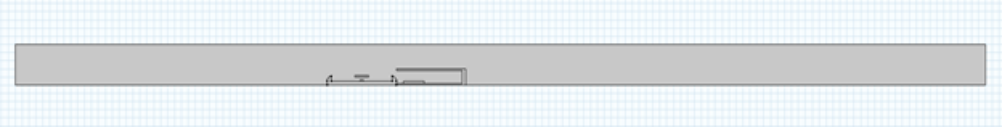

Figure 2.23: The entire two-dimensional geometry of the CVD chamber implemented in the COMSOL simulations

  We assume the precursor powder to be distributed as rectangular with a length 0.5 cm and a height of 0.15 cm. The length of each boat is 10cm, and there is a Si substrate on top of the precursor powder, which acts as the barrier. The length of the Mo substrate is set to be 3cm with a rectangular shape.

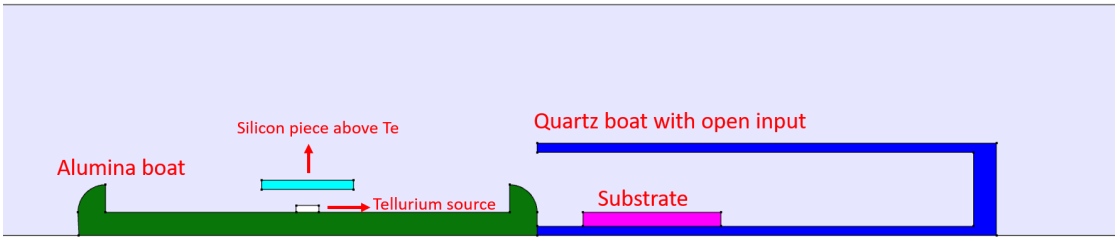

Figure 2.24: The geometry of boats and substrate inside the CVD chamber

- **Temperature on the walls of chamber**

  The temperature profile of the walls should be implemented as boundary conditions. This temperature is chosen according to the temperature set in the experimental configuration of each furnace. The temperature of the upstream and downstream furnaces are set to 650 and 625°C. The temperature profile in Figure 2.25 is used as boundary condition.

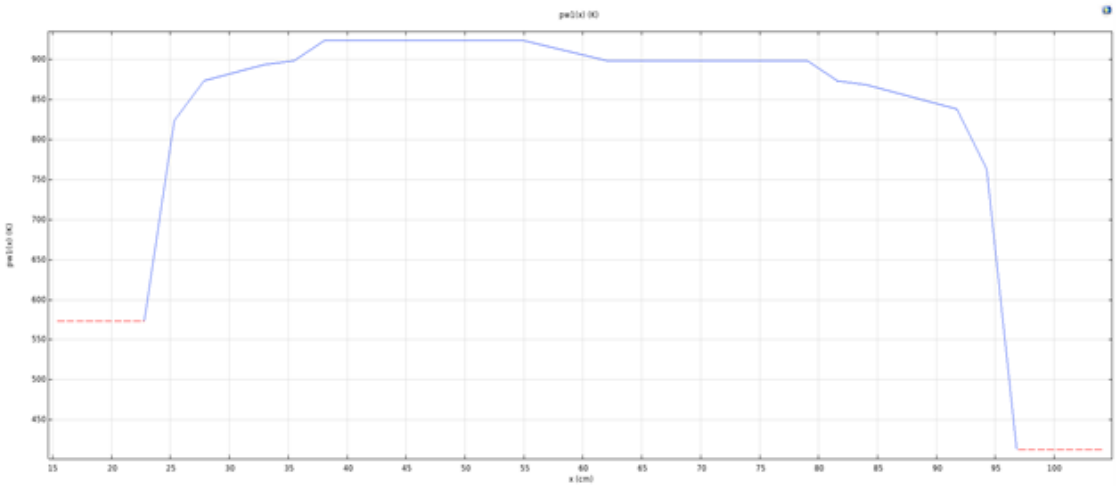

Figure 2.25: The temperature profile over the chamber's wall

- **Meshing of the geometry**

  The continuum domain is discretized using a triangular mesh with "Fine" element size on the whole geometry and "Finer" size on the boundaries. There is also "corner refinement" adapted with element size scaling factor 0.25.

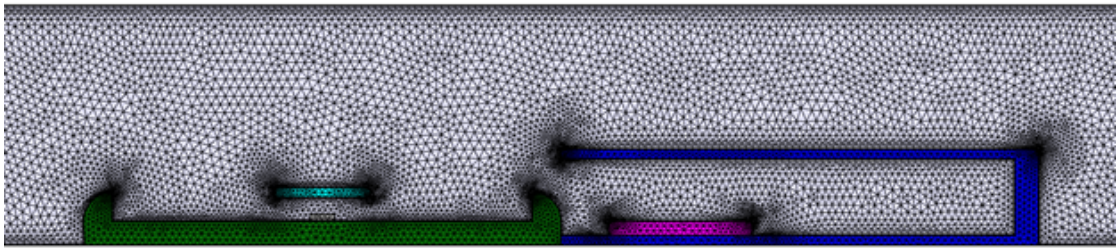

Figure 2.26: The "user-defined" meshing of the boats

- **Implemented Boundary Conditions**

  The Boundary conditions applied to the Navier-stokes equation are summerized in the table below:

Walls	**Inlet**	**Outlet**
No Slip	*Mass Flow*	*Zero Pressure*
$u = 0$	*100 sccm Flow Rate*	$-p\mathbf{I} + \mu(\nabla\mathbf{u} + (\nabla\mathbf{u})^T) - \frac{2}{3}\mu(\nabla.\mathbf{u})\mathbf{I} = 0$

Table 2.6: Boundary conditions applied to the laminar flow interface

The boundary conditions that are applied to the diffusion-based transport are as follow:

Walls	**Inflow**	**Outflow**
$-n.N_i = 0$	$c = 0$	$-n.D_i\nabla c_i$

Table 2.7: Boundary conditions applied to the transport of diluted species interface

- **Implemented Initial Values**

  Carrier gas density ρ, carrier gas heat capacity C, carrier gas thermal conductivity k, and carrier gas dynamic viscosity μ are functions of temperature and should be defined as piecewise functions at different temperature intervals. These parameters are depicted in Figure 2.27. These functions can be imported from the material library of COMSOL, which contains the properties of different materials as piecewise polynomial functions of temperature.

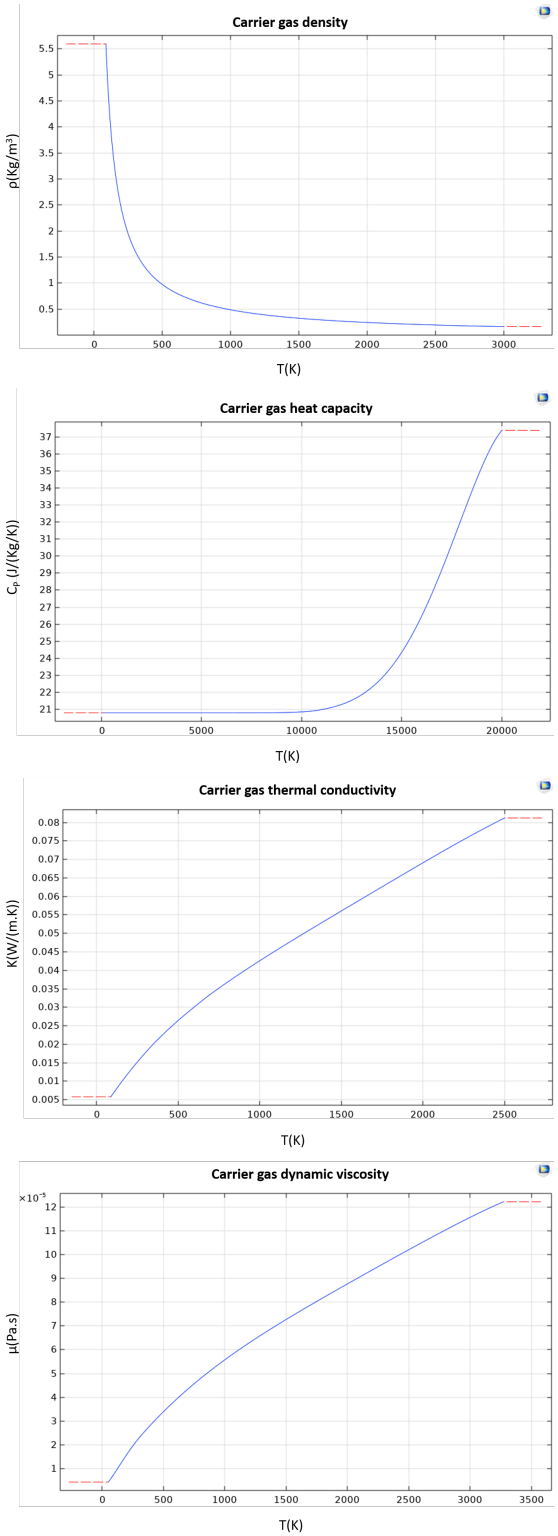

Figure 2.27: Carrier gas density, heat capacity, thermal conductivity and dynamic viscosity as a funcion of temperature 41

Chapter 3

$MoTe_2$ growth: results and discussion

In this chapter, the synthesis method based on Chemical Vapor Deposition (CVD) and described in the previous chapters is employed for growing large-area continuous films of $MoTe_2$. In detail, the process can be distinguished from a standard CVD approach since it is a heterogeneous vapor–solid reaction between a pre-deposited molybdenum solid film and tellurium vapor, thus resulting in the controlled growth of $MoTe_2$ films onto SiO_2/Si substrates utilizing a tellurization approach. The growths were performed controlling different experimental parameters, including temperature, carrier gas flux and type, the distance between the precursors, and substrate positioning into the reactor tube. Optical and surface characterization techniques, including Raman Spectroscopy and Atomic Force Microscopy, were used to study the vibrational and morphological properties of the grown films. The confocal Raman Spectroscopy was performed using Renishaw InVia spectrometer with excitation wavelength in the visible range (514 nm). The AFM measurements were made by a Brucker Dimension Edge in Tapping mode with few nm spatial resolution on the surface plane.

3.1 Molybdenum precursor films

During the tellurization experiments, the molybdenum precursor was a pre-deposited film onto a $SiO_2(50nm)/Si(100)$ substrate obtained by electron beam evaporation. In reference [59], the films deposited by e-beam in the CNR laboratory have been analyzed employing X-ray photoelectron spectroscopy (XPS) to determine the chemical composition of the film. This analysis revealed that the evaporated films react with the oxygen in the environment when brought outside the deposition chamber. In Figure 3.1, I report the XPS spectra taken from reference [59].

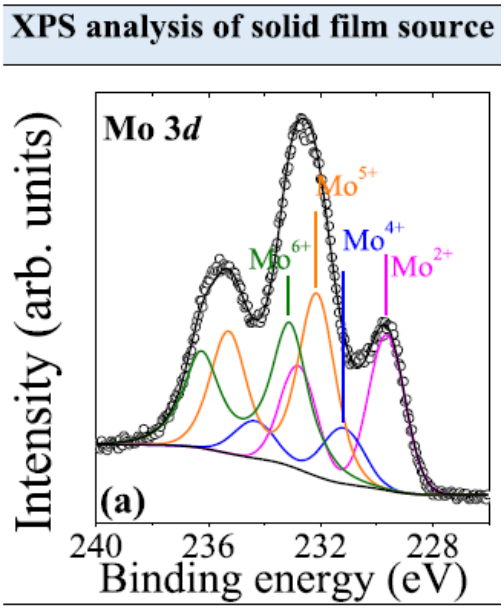

Figure 3.1: XPS profile of Mo atoms binding energy for e-beam evaporated Mo film [59].

The figure shows the *Mo 3d* core level of the deposited precursor as a function of the binding energy. The deconvolution of the spectrum in different components demonstrates that the Mo film undergoes oxidation into four different oxidation states, namely $Mo^{6+}, Mo^{5+}, Mo^{4+}, Mo^{2+}$. This study clearly suggests that the reactions involved in the tellurization process are similar to those reported for the sulfurization process [59] and are of the following type:

$$MoO_x + 3Te \rightarrow MoTe_2 + TeO_x \tag{3.1}$$

It is worth noting that Equation 4.1 may involve a reduction of the oxidation state of molybdenum; therefore, it is favored in the presence of reducing species like hydrogen. In the following, I will show that this is confirmed by comparing the experiments carried out with and without the presence of a small percentage of molecular hydrogen in the carrier gas.

In order to evaluate the thickness of the grown film, the substrate was patterned prior to deposition of the Mo film. The AFM topographies in Figure 3.2 a-b show that the Mo film has a thickness of 8 nm and a smooth and homogeneous morphology with RMS roughness below 1 nm. This is made clear by observing the height

profiles in panels c and d, respectively. In panel c, the blue line starts from the un-deposited place on the substrate, which the background is darker, and continues to scan inside the deposited area with bright color. In panel d, the height profile scans inside the deposited area on the substrate showing a flat and homogenous deposition.

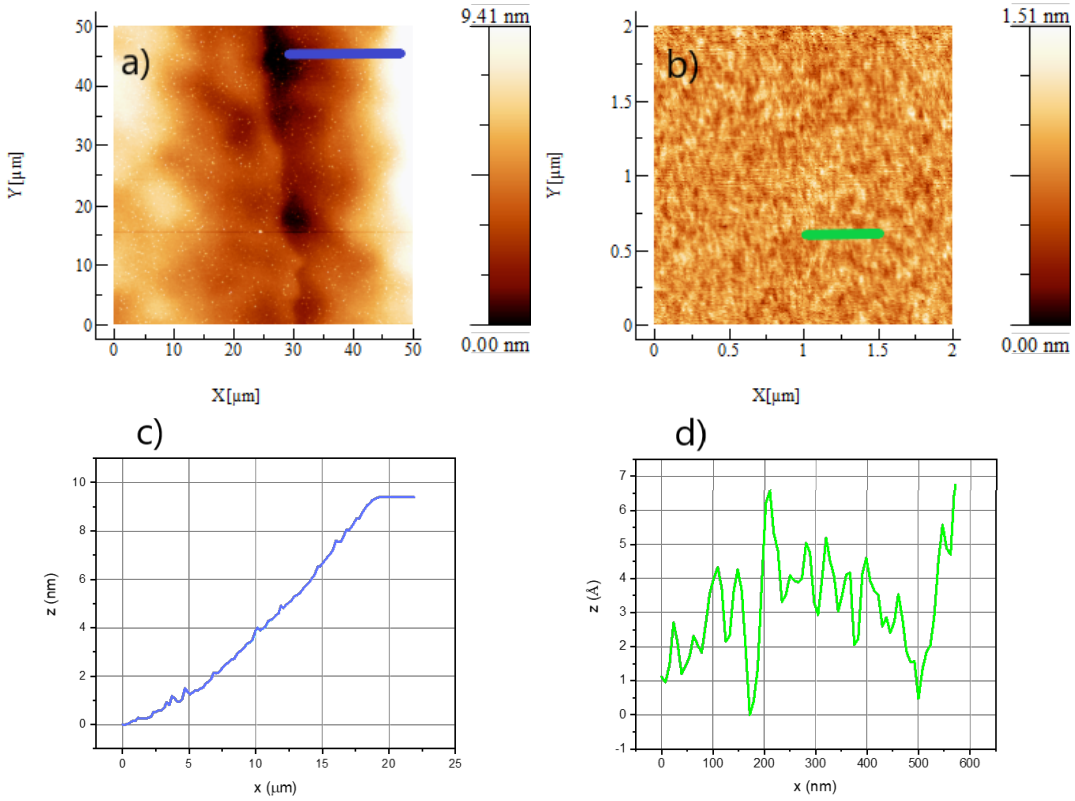

Figure 3.2: a) $50\mu m \times 50\mu m$ topographical image of the patterned Mo deposited film. b) $2\mu m \times 2\mu m$ topographical image from the inside of the Mo deposited area. c) cross-sectional plot along the blue line in a. d) cross-sectional plot along the green line in b.

3.2 $MoTe_2$ Growth

In the course of this experimental work, we studied the impact of the different growth parameters on the quality of the $MoTe_2$ films. Different variables can be changed, one at a time, aiming at optimizing the CVD growth:

1. **Growth Temperature:** we study the effect of the growth temperature on the $MoTe_2$ film formation. Two different temperatures were explored $700°C$ and $800°C$. We can expect the growth temperature to be a critical parameter since it affects the surface reaction rates and the dynamics of the chemical reactions involved.

2. **Carrier Gas:** The impact of the carrier gas flux and composition was studied by varying the flow rates of N_2 gas in the range 30- 90 sccm and using or not the Ar/H_2 gas flux at 100 sccm.

3. **Distance and Geometry:** Another variable that is expected to have a crucial role in our method is the distance between the Mo film and the Te powder source. We studied the effect of a change of distance from 14cm to 6cm. Then, in order to improve the growth quality, we change the configuration of the substrate from a flat to a tilted positioning.

4. **Growth Time:** For a systematic study, the impact of the growth time on the film quality was evaluated at a fixed temperature ($625°C$) and varying the time from 60 to 180 minutes at different steps.

3.2.1 Growth Temperature

Morphological Analysis

In this section, I investigate the effect of two different growth temperatures on the $MoTe_2$ formation using AFM and Raman spectroscopy to characterize the samples. Table 3.1 summarizes the experimental conditions employed for the growth of sample 1 and sample 2 obtained respectively at $700°C$ and $800°C$. After the process, from the visual inspection of the sample and then from the optical microscope investigation, we detected clear changes in the colour and optical reflectivity of some areas of the pre-deposited Mo films, see Figure 3.3. Our assumption was that in these regions the tellurium vapour reacted with the solid Mo film to form the $MoTe_2$ layers.

Figure 3.3: The sample after growth.

Sample	Upstream T($^\circ C$)	Downstream T($^\circ C$)	Growth Time (minutes)	Carrier Gas Flux (sccm)
1	650	700	120	100 (Ar/H_2) - 60 (N_2)
2	650	800	120	100 (Ar/H_2) - 60 (N_2)

Table 3.1: Process conditions used to grow $MoTe_2$ in Sample 1 and Sample 2.

We investigated the morphology of the two samples by AFM taken in tapping mode, and two representative topographies are shown in Figure 3.4 a-b. The measurements are reported with a 2 µm scan size. The topography of the films reveals that in both cases, the films are continuous and completely cover the surface, as made clear by the height profiles along the blue lines reported in panel c-d. The statistical analysis of the maps shows that the RMS roughness of the samples increases with the temperature. Indeed, the sample grown at temperature $700^\circ C$ has RMS roughness of 4.27 nm, while the sample obtained at $800^\circ C$ has RMS roughness of 6.96 nm. Matching these values with the AFM analysis of the Mo precursor, we can conclude that the effect of the tellurization process is to increase the surface roughness. Moreover, the topographies in Figure 3.4 a-b show that the morphologies are constituted by grains with the mean size that can be assessed recurring to the images' self-correlation function as described in the previous chapter.

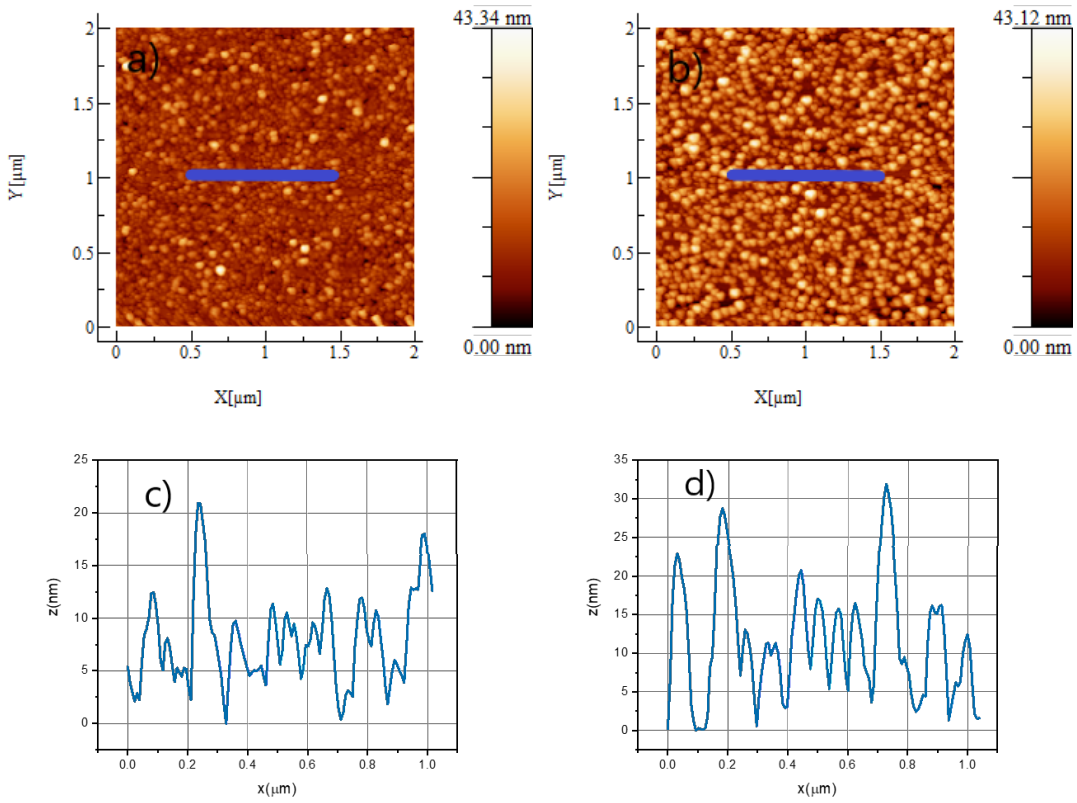

Figure 3.4: $2\mu m \times 2\mu m$ topographical image of the $MoTe_2$ a) Sample 1. b) Sample 2. c) cross-sectional plot along the blue line in a. d) cross-sectional plot along the blue line in b.

In Figure 3.5 a-b, we show the self-correlation function of the AFM topographies of Figure 3.4 a-b. The symmetric central peak in the self-correlation function demonstrates that in both cases, the morphology of the samples is constituted by grains with symmetric round shapes. Therefore, we can assess the mean grain size by measuring the full-width-half-maximum of the peak along a horizontal line profile at the center of the image. In order to avoid artifacts connected to instrumental (electronic or thermal) drifts and tip wear, we repeated the self-correlation filter on several topographies acquired at different times and with different tips. The reported mean grain size values have been obtained as the mean value calculated on the different measurements. The uncertainty has been obtained as the standard deviation of the measurements from the mean value. We can conclude that the average grain size is $50.22nm \pm 2.48$ for sample 1 grown at $700°C$ and $84.76nm \pm 15.41$ for sample 2 grown at $800°C$.

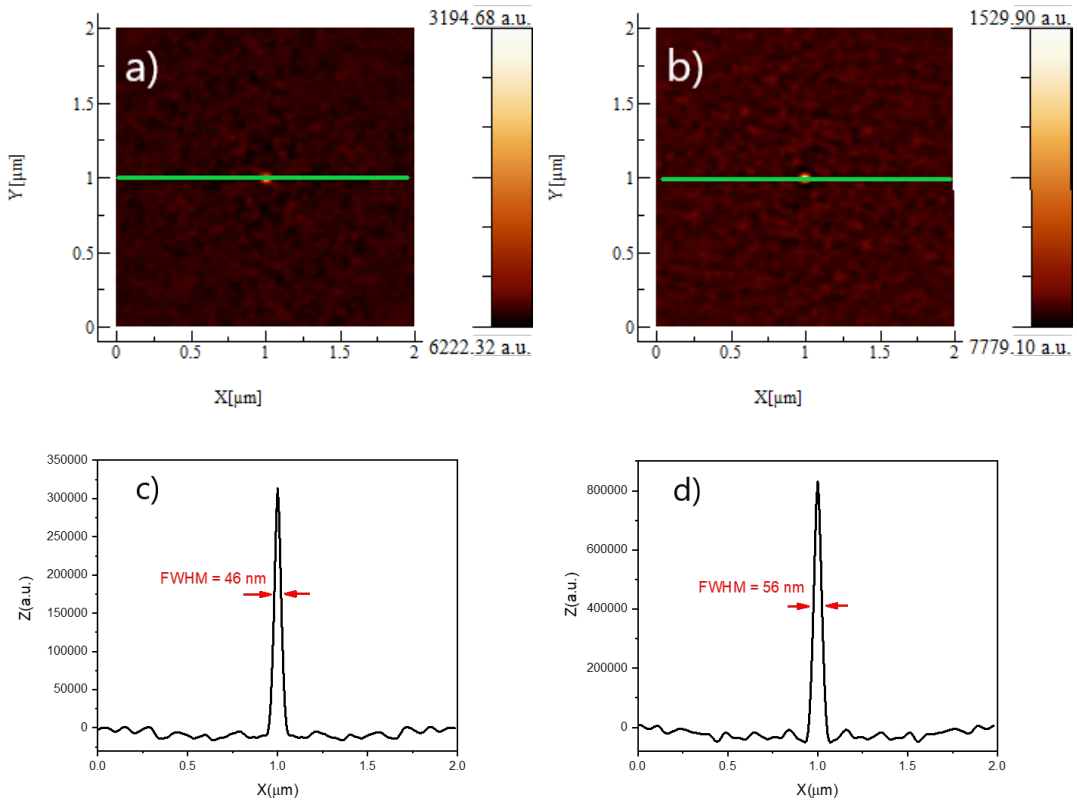

Figure 3.5: a) $2\mu m \times 2\mu m$ Self-correlation image of the $MoTe_2$ Sample 1. b) $2\mu m \times 2\mu m$ Self-correlation image of the $MoTe_2$ Sample 2. c) cross-sectional plot along the green line in a. d) cross-sectional plot along the green line in b.

Raman Scattering Investigation

To gain a deeper insight into the $MoTe_2$ formation, we used Raman scattering spectroscopy carrying out a positional investigation from the left part of the sample, namely the part closer to the tellurium source, to the opposite right part, see the sketch in Figure 3.6.

Figure 3.6: The sample after growth at 700°C with dedicated left and right positions of the sample

Figure 3.7 a and b shows the Raman spectra of sample 1 and sample 2, respectively. The spectrum at 700°C exhibits three sharp peaks at 111cm^{-1}, 127cm^{-1}, and 161cm^{-1}, which are assigned to A_u, A_g, and B_g modes, respectively. According to reference, these peaks are associated with the 1T' phase of $MoTe_2$ [60]. There is a weak hump at 261cm^{-1} that is assigned to A_g mode of vibration.

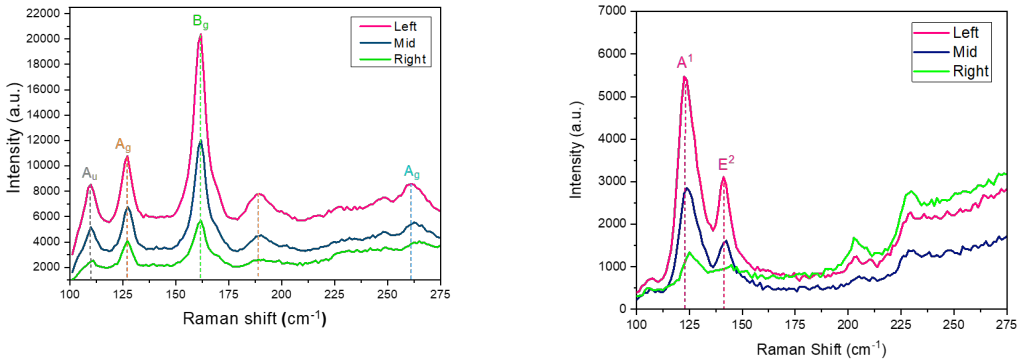

Figure 3.7: The Raman spectrums with the growth temperature 700°C (left) and 800°C (right).

The observed peaks at left side of the sample, which the Raman intensities are higher than other positions are fitted by Voigt components, and they present FWHM dedicated in table 3.2. The FWHMs of the peaks are sensibly larger than those of the exfoliated material reported in Chapter 3.

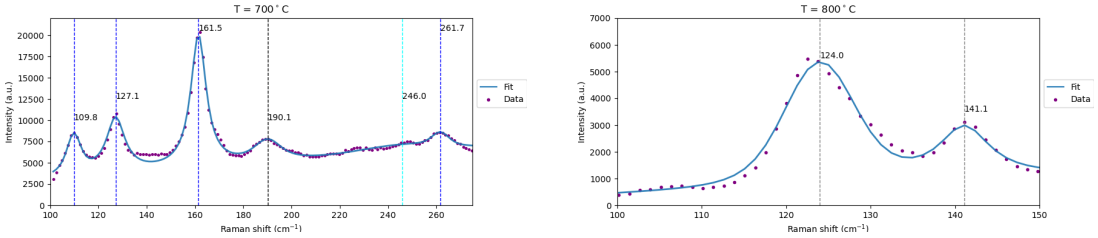

Figure 3.8: The fitted Raman spectrums with the growth temperature 700°C (left) and 800°C (right).

Sample	A_u Peak	A_g Peak	B_g Peak	B_g Peak	A_g Peak
CVD grown - sample 1	5.10 nm	6.51 nm	6.90 nm	12.44 nm	17.03 nm
Mechanical Exfoliated flake	4.74 nm	4.52 nm	4.58 nm	8.10 nm	9.34 nm

Table 3.2: Comparison of the FWHM of the Raman A_u, A_g, B_g, B_g, and A_g peaks between the CVD grown sample 1 and Mechanical exfoliated flake.

This result suggests that the structural order of the grown material is lower than the exfoliated flakes. As a matter of fact, the width of the Raman modes is dramatically affected by the degree of disorder inside the material, which introduces a broadening of the atomic bond length distribution and thus of the vibrational frequency distribution. This observation can be easily linked with the morphological pieces of information derived by the AFM analysis, which showed the presence of grains and grain boundaries. Nevertheless, the Raman mode FWHMs of our sample are comparable to those of CVD-grown $MoTe_2$ films reported in the literature [60]. For the sake of completeness, we note that the band center at $190cm^1$ is assigned to a minor oxide tellurium component into the film. As confirmed by a recent study based on X-ray photoelectron spectroscopy (XPS), the oxidation of $MoTe_2$ film obtained by CVD occurs in few minutes after exposure to ambient conditions and is limited to the outermost part of the film [59]. The positional analysis indicates that the sample is not uniform: the Raman intensity decreases moving from the left to the right. Quantitatively, taking the B_g peak as a reference, the intensity ratio between the left and right spectra is $\frac{I_{B_g}(left)}{I_{B_g}(right)} = 3.6$.

The same variability in the Raman spectra is observed in sample 2 grown at $800°C$. Nevertheless, we can observe a stark difference in the vibrational modes of this sample compared to sample 1. The most intense peaks in sample 2 is at $122cm^{-1}$, which is assigned to the A_1 mode of Te related to the chain expansion in which each atom moves in the basal plane. The other peak at $141cm^{-1}$ is assigned to E_2 mode, represent the asymmetric stretching along the c-axis of the Te chain [61]. These assignments suggest that in the process at $800°C$, the CVD does not result in the formation of $MoTe_2$ films by tellurization of the pre-deposited molybdenum precursor. Instead, it results in the deposition of Te only onto the SiO_2/Si substrate. We can speculate that performing a reaction environment at a high temperature leads to the evaporation of the Mo deposited film prior to its reaction with Te vapor.

Preliminary Conclusion

In conclusion, our study confirms that the $MoTe_2$ film can be obtained by tellurization of a pre-deposited Mo precursor. More in detail, we established a temperature threshold corresponding to $700°C$ for the dominant 1T' phase formation. Moreover, in Figure 3.9, we show the AFM topography of sample 1 after

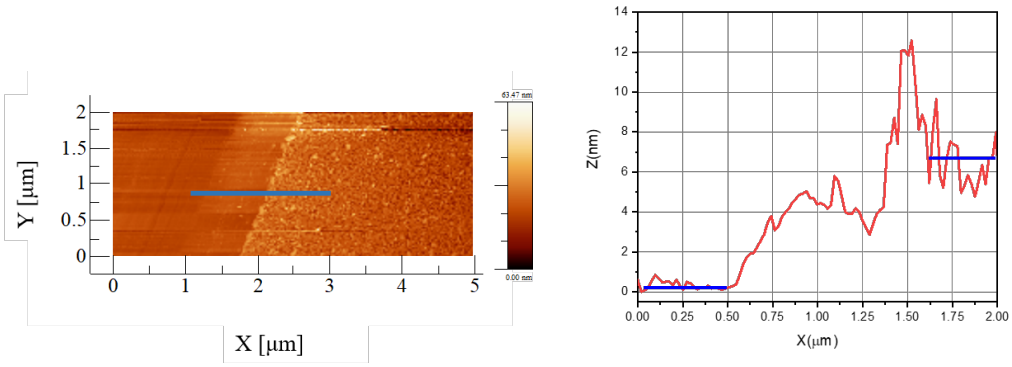

Figure 3.9: The topographical image of the sample after scratching with a micrometer tip (left) - Height profile along the depicted line (right).

mechanical scratching of the deposited film with a micrometer tip. We used the scratch to quantitatively assess the thickness of the deposited $MoTe_2$. The height profile confirms that the film is around 7 nm thick in quantitatively agreement with the Mo pre-deposited precursor. Even though we can not exclude that part of the Mo precursor does not react with tellurium, this result suggests that, similar to the case of sulfurization [59], we can control the thickness of the $MoTe_2$ film by controlling the thickness of the e-beam deposited Mo film.

3.2.2 Carrier Gas Flux

Before studying the effect of the gas fluxes, I performed two experiments with and without introducing the Ar/H_2 gas mixture. These experiments aim to demonstrate that a reducing atmosphere is beneficial to promote the $MoTe_2$ formation. Figure 3.10 shows the Raman spectra of the two samples with the usages of N_2 gas flux and Ar/H_2. In the case of using N_2 as the carrier gas, we obtain no deposition at all, and the Raman spectra represents only the second-order peak of SiO_2 at $301cm^{-1}$. However, by exploiting Ar/H_2 mixture, the growth leads to deposition of $1T' - MoTe_2$.

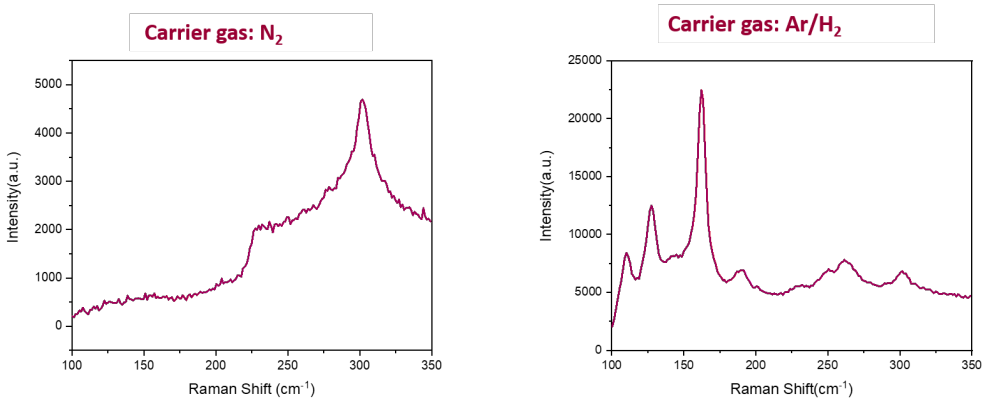

Figure 3.10: The Raman spectra from the sample that is grown with the usages of N_2 as carrier (left) - The Raman spectra from the sample that is grown with the usages of Ar/H_2 as carrier (right).

After studying the effect of the hydrogen mixture, I investigated the effect of N_2 gas flux on the Raman spectra and surface morphologies. We explored three different N_2 fluxes: 30, 60 and 90 sccm. The growth time and temperature are kept unchanged as the Sample 1 introduced in the previous case study. For the sake of simplicity, the experimental conditions are summarized in Table 3.3.

Sample	**Upstream T($^\circ C$)**	**Downstream T($^\circ C$)**	**Growth Time (minutes)**	**Carrier Gas Flux (sccm)**
3	650	700	120	100 (Ar/H_2) - 30 (N_2)
4	650	700	120	100 (Ar/H_2) - 60 (N_2)
5	650	700	120	100 (Ar/H_2) - 90 (N_2)

Table 3.3: Process conditions used to grow $MoTe_2$ in Sample 3, Sample 4 and Sample 5.

Morphological Analysis

Figure 3.11 a-c shows three representative AFM measurements corresponding to the experiments with 30, 60, and 90 sccm gas fluxes, respectively. Furthermore, the corresponding height profiles along the blue lines are shown in panel d-f.

From these measurements, it can be realized that at 30 sccm flux, the deposition is not uniform and results in cluster formation. Clusters have lateral size of hundread of nanometers and height in the same vertical range. They coalesced in large structures leaving large part of the substrate exposed, for this reason the RMS roughness of the surface morphology is as high as 19nm.
By increasing the gas flux to 60 and 90 sccm, AFM measurements confirm more uniform deposition and a compact granular morphology in both cases. The RMS roughness is estimated at 5.94 and 7.31nm, respectively.

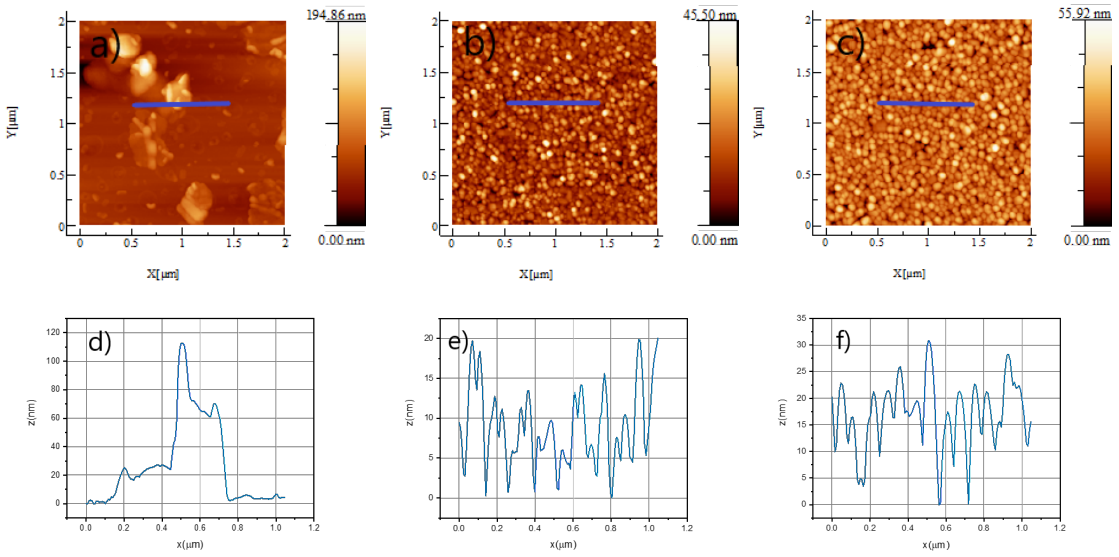

Figure 3.11: $2\mu m \times 2\mu m$ topographical image of the $MoTe_2$ a) Sample 3. b) Sample 4. c) Sample 5 - cross-sectional plot along the blue line d) in a. e) in b. f) in c.

Average Grain Size

The self-correlation filter of the topography images at 60 and 90 sccm experiments is depicted in Figure 3.12 a-b. By measuring the FWHM of the center in these images, we conclude that the amount of gas flux does not affect the average grain size.

The topography of Figure 3.11 a, corresponding to the sample obtained at 30 sccm, cannot be analyzed utilizing the self-correlation function filter because of the not homogeneous deposition.

On the other hand, the samples at 60 and 90 sccm show a symmetric self-correlation function of the AFM topographies in Figure 3.12. The symmetric central peak in the self-correlation function demonstrates that the morphology of the samples is constituted by grains with symmetric round shapes in both cases. Therefore, we can assess the mean grain size by measuring the full-width-half-maximum of the peak along a horizontal line profile at the center of the image. The reported mean grain size values have been obtained as the mean value calculated on different AFM measurements; the uncertainty has been obtained as the standard deviation of the measurements from the mean value. We can conclude that the average grain size is 52.62 ± 8.43 nm for the sample grown at 60 sccm and 55.58 ± 10.34 nm for the sample grown at 90 sccm.

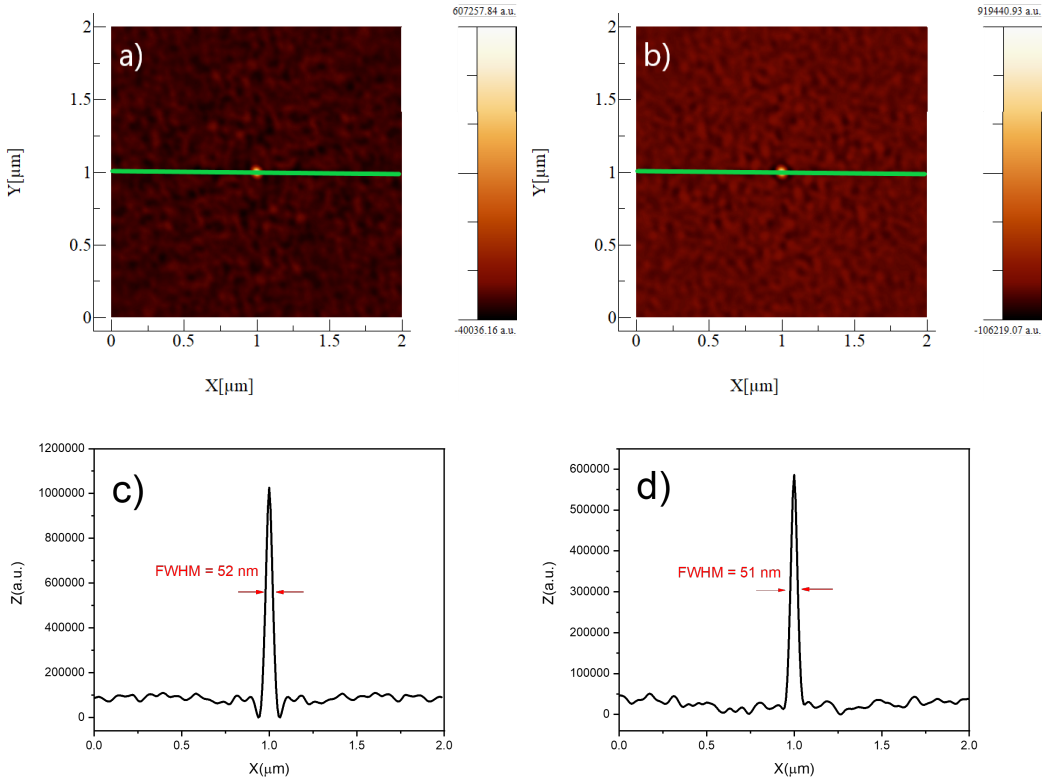

Figure 3.12: $2\mu m \times 2\mu m$ Self-correlation image of the $MoTe_2$ a) Sample 4. b) Sample 5 - cross-sectional plot along the green line in c) a. d) b.

Raman scattering investigation

As for the previous studies, I used Raman spectroscopy to gain a deeper understanding of the material deposition. In Figure 3.13, I show the Raman spectrum of the sample grown with 30 sccm gas flux. I carried out a positional analysis of the sample acquiring the Raman spectra in three positions from the left (closer to the tellurium source) to the right. I observed an high variability of the spectra in term of peak intensity. More in detail, all the spectra exhibit two main peaks at 120 and 140.7cm^{-1}. These two peaks are assigned to A^1 and E^2 peaks of Te. Other peaks at 162cm^{-1} and 260cm^{-1} are assigned to B_g and A_g peaks of 1T' phase of $MoTe_2$. The spectrum also exhibits the MoO_2 peak at 190cm^{-1}. It is interesting to notice that the high degree of structural disorder identified with the AFM investigation reflects into broad Raman peaks, see for instance the A_1 mode in the spectra.

Figure 3.14 shows the Raman spectrum of the samples grown with 60 sccm and 90 sccm gas flux, respectively. They exhibit three main peaks of the 1T' $MoTe_2$ phase: A_u, A_g, and B_g at 109, 127, and 162cm^{-1} respectively. Apart from a slight difference in the peak intensity, the variability of the Raman spectra is more pronounced in the sample obtained with 60 sccm gas flux. Nevertheless, the study clearly demonstrates the formation of the $MoTe_2$ film in both the cases. Also in this case, the FWHMs of the Raman peaks are larger than those of the exfoliated flakes but comparable to those obtained in other CVD grown $MoTe_2$ films. I reported the analysis fit of the Raman peaks in Table 3.4.

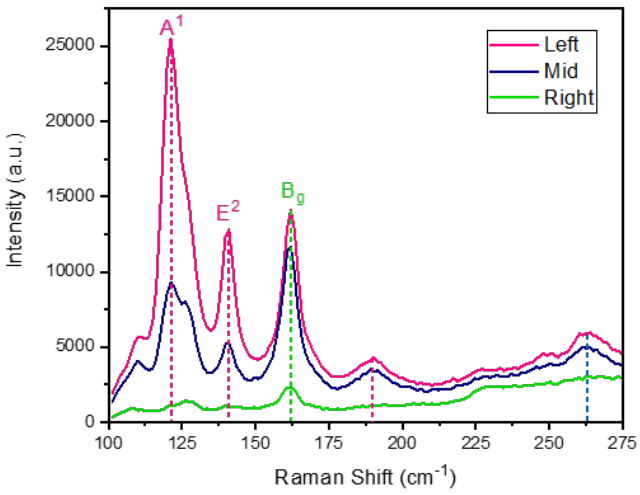

Figure 3.13: Raman Spectrum with the N_2 gas flux 30 sccm.

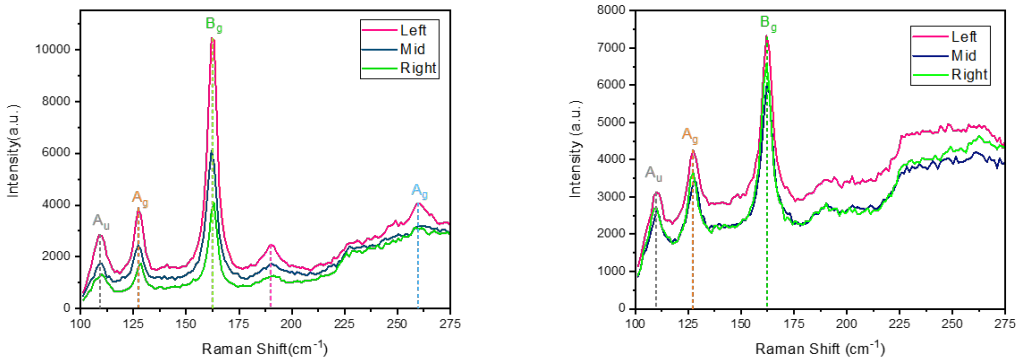

Figure 3.14: Raman Spectrum with the N_2 gas flux 60 scccm (left) and 90 sccm (right).

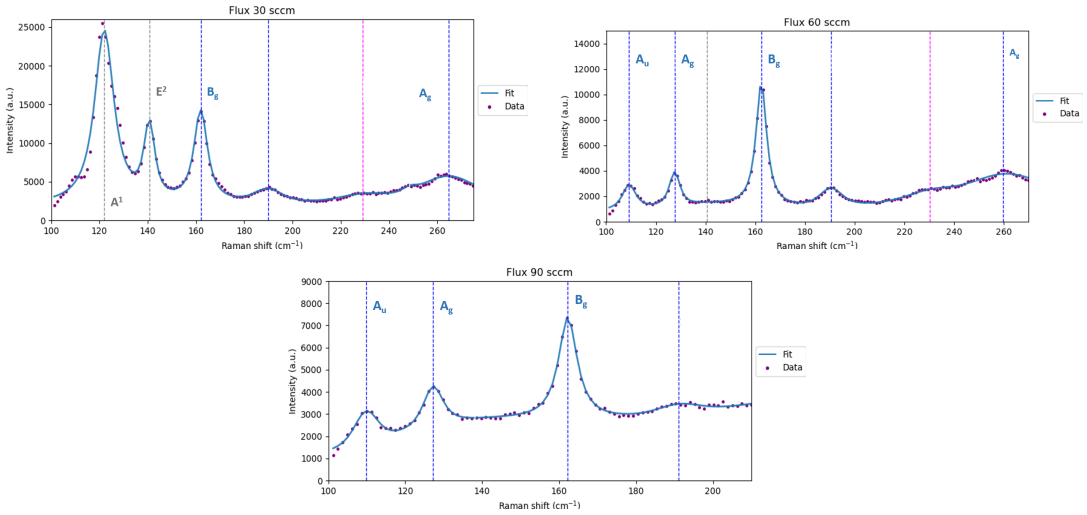

Figure 3.15: The fitted Raman spectrums of the left side (closer to the tellurium source) of the sample 3, 4, and 5 with Voigt function.

Sample	A^1 Peak	E^2 Peak	A_u Peak	A_g Peak	B_g Peak	MoO_2 Peak	A_g Peak
Sample 3	7.08 nm	5.44 nm	-	-	6.32 nm	12.65 nm	21.43 nm
Sample 4	-	-	6.31 nm	5.18 nm	5.19 nm	6.79 nm	48.32 nm
Sample 5	-	-	4.65	8.80 nm	5.75 nm	12.82 nm	-

Table 3.4: Comparison of the FWHM of the Raman A^1, E^2, A_u, A_g, B_g, MoO_2, and A_g peaks between the sample 3, 4, and 5.

Preliminary conclusion

We can draw some preliminary conclusions based on the studies of the role of the carrier gas. Firstly, I demonstrated that a reducing atmosphere, provided by the presence of molecular hydrogen during the high-temperature process, is mandatory for the tellurization reaction to occur.

Secondly, I showed that a low gas flux, i.e., lower than 60 sccm, does not result in a uniform and homogenous $MoTe_2$ formation. Both AFM and Raman spectroscopy pointed out that, in this case, the film is highly disordered, and not-reacted tellurium deposition is found. This result can be explained considering that such low gas flux could not be enough to provide sufficient tellurium atoms for the reaction to occur before evaporation of the molybdenum film.

Lastly, by comparing the FWHM and intensities of the Raman B_g peak at 60 sccm and 90 sccm gas fluxes, I found more homogeneity in the growth of $MoTe_2$ is obtained at fluxes higher than 60 sccm. This is reported in Figure 3.16, where I used the analysis on different Raman spectra to calculate the mean value and uncertainty on the measure using the standard deviation from the mean value. The data show that at 90 sccm, the dispersion around the mean value is very low both in the intensity and FWHM value of the peak. In addition, I found that the same condition holds for samples obtained in the flux range 90-150 sccm that I identified as the optimal condition for the growth.

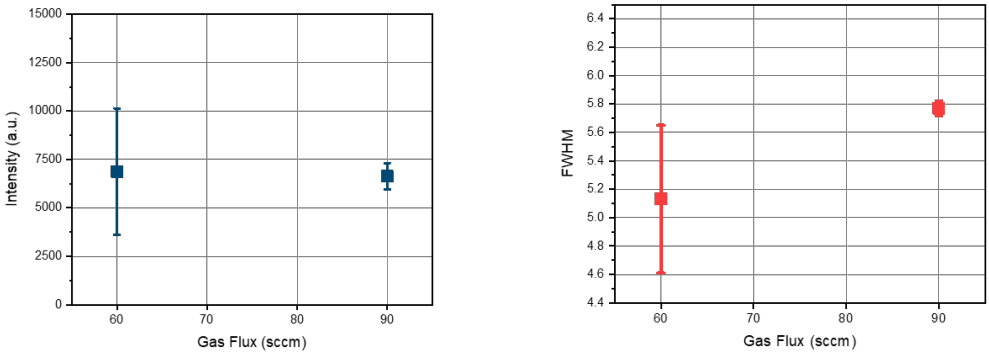

Figure 3.16: Comparison of the B_g peak intensities (left) and FWHM (right) at 60 and 90 sccm gas flux

3.2.3 Boats Distance and Substrate Positioning

In the previous sections, I studied the role of temperature growth and carrier gas (type and flux) on the formation of the $MoTe_2$ film. Here, to obtain more precise control of the film homogeneity and structural quality, I explore the effects of changing the precursor distance and the substrate positioning. More in detail, I will show the results obtained reducing the gap between the boats containing the precursors from 14 cm to 6 cm. In addition, to investigate the critical parameters controlling the growth scale, I compare two different substrate positions: (I) the substrate surface parallel to the gas flow and facing up lying on the bottom of the boat, (II) the substrate surface facing toward the gas flow and tilted with respect to the boat's bottom. Based on the results of the previous sections, I set the growth temperature and Ar/H_2 carrier gas flux at 650°C and 100 sccm, respectively.

Sample	Geometry	Upstream T(°C)	Downstream T(°C)	Growth Time (minutes)	Carrier Gas Flux (sccm)
6	Flat	650	625	60	100 (Ar/H_2)
7	Tilted	650	625	60	100 (Ar/H_2)

Table 3.5: Process conditions used to grow $MoTe_2$ in sample 6 and sample 7.

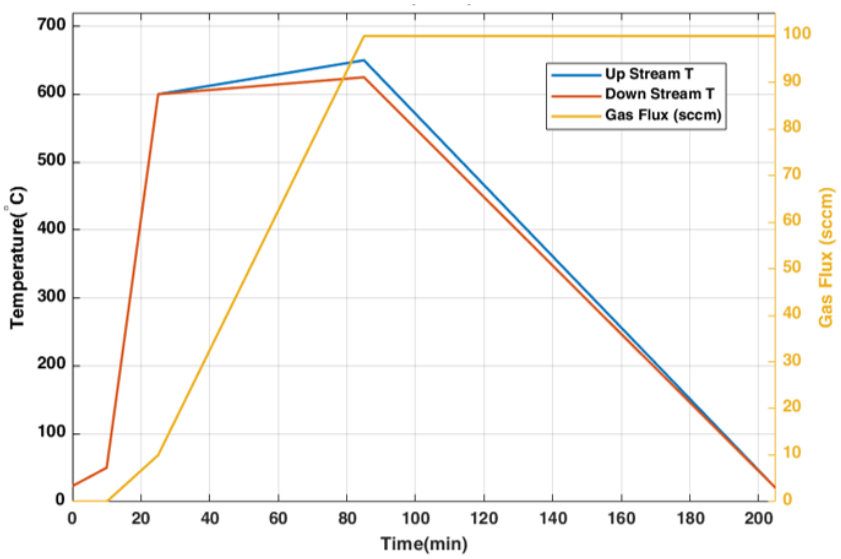

Figure 3.17: Growth ramp of sample 6 and sample 7.

In a recent paper [62], numerical calculations based on transport phenomena predicted the distribution of velocities, concentrations, and concentration gradients of precursors during the CVD growth of MoS_2. Furthermore, these calculations have provided valuable hints for the optimization of the experimental parameters during the synthesis. Inspired by these studies and aiming at calculating the concentration gradient distribution of the tellurium precursors in the CVD system, I developed and implemented the model described in Chapter 3 using the commercial finite element software package COMSOL.

My first goal was to study the effect of changing the distance between the two precursor boats. I modeled two experimental conditions corresponding to a distance of 14 cm, the same employed in the study presented in the previous sections, and 6 cm, the minimum gap distance achievable in the CVD configuration I used during the activity. In Figure 3.18, I plot the results of the calculated concentration of Te precursor C, (background color); its gradient in front of the substrate (arrows) $|\nabla C|$; and carrier gas stream velocity (solid lines) |V| for two different distance between precursor boats 14 cm and 6 cm. The arrows' color and size are proportional to the amount of concentration close to the substrate. For the case of 14 cm distance, due to the lower concentration of Te close to the substrate, I used $\times$ 20 larger scale of arrows to clarify the results better.

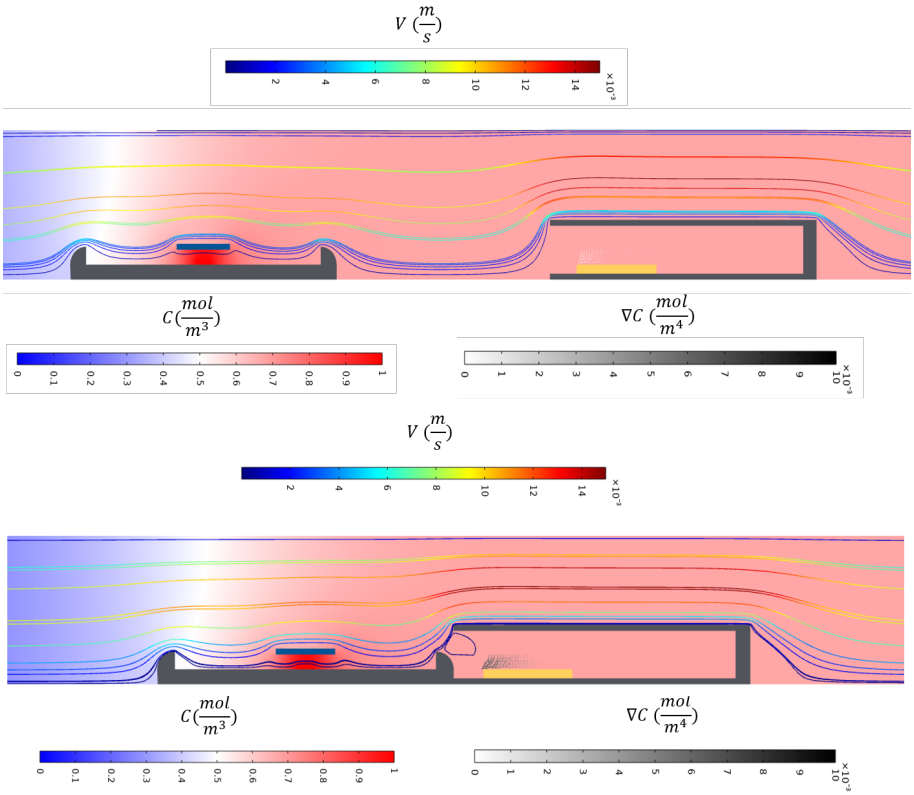

Figure 3.18: Distance between the Te source and Mo substrate = 14 cm (top). distance between the Te source and Mo substrate = 6 cm (bottom).

I tried to match the results predicted by the model with the experimental results. Figure 3.19 shows the Raman spectra of the samples obtained with the gap between the precursors 14 cm and 6 cm, respectively. The Raman spectra of the 14 cm gap indicate a tiny B_g peak at 162 cm^{-1} and dominant substrate peak at 303 cm^{-1} which confirms the prediction of low Te concentration and its gradient by the simulation. Instead, the Raman spectra, by decreasing the distance, reveals improvement of the intensities and dominant B_g peak at 162 cm^{-1}. The intensity ratio between the B_g peaks of these two cases is: $\frac{I_{14cm}}{I_{6cm}} = \frac{4660}{12518} = 0.37$.

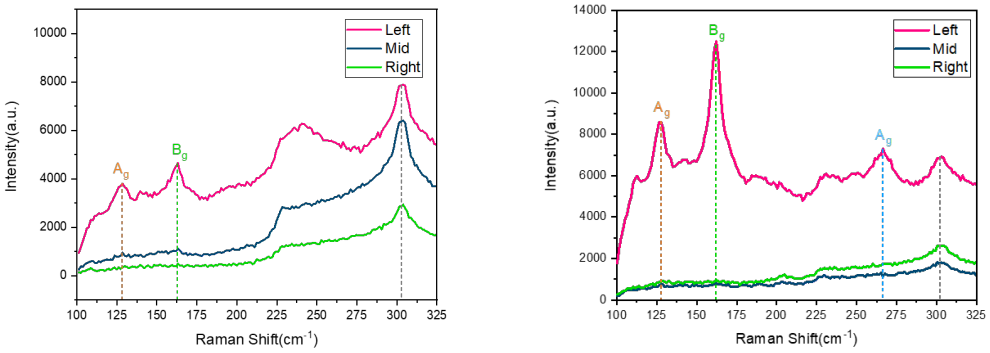

Figure 3.19: Raman spectra of the sample with distance of 14 cm between precursor boats (left) - Raman spectra of the sample with the distance of 6 cm between the precursor boats (right).

Substrate positioning: flat and tilted

Having established that reducing the distance between the two precursors is beneficial for the growth, I modeled, in the implemented COMSOL experiment, two different configurations for the Mo precursor positioning inside the boat. The first configuration is the flat positioning, in which the sample lies down on the bottom of the boats. The second configuration is the tilted one with the sample facing the gas flux. For the sake of clarity, I show the two configurations in the sketches of Figure 3.20.

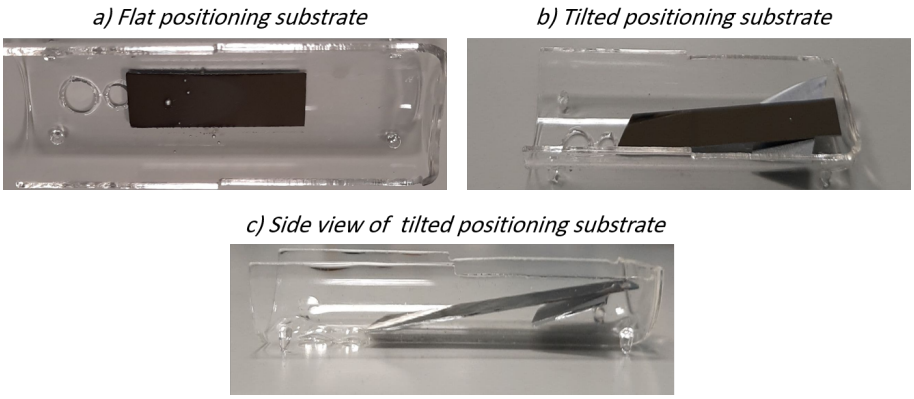

Figure 3.20: a) Configuration of the flat positioning substrate (top view) - configuration of the tilted positioning substrate b) (top view) - c) (side view).

Flat configuration

The numerical simulation results for the concentration of Te vapor and flow around the substrate are shown in Figure 3.18, which indicates a change in Te gradient concentration along the substrate. The color of the background represents Te concentration, while streamlines show the carrier gas velocity. Simulation results predict a significant reduction of the mass flow along the substrate, from left to right, resulting in a lower density of the grown film. It can be due to decreasing the carrier gas velocity, which induces a smaller thermodynamic driving force for the growth. The color change of the arrows corresponds to the concentration of the Te, i.e., darker arrows indicate a higher concentration.

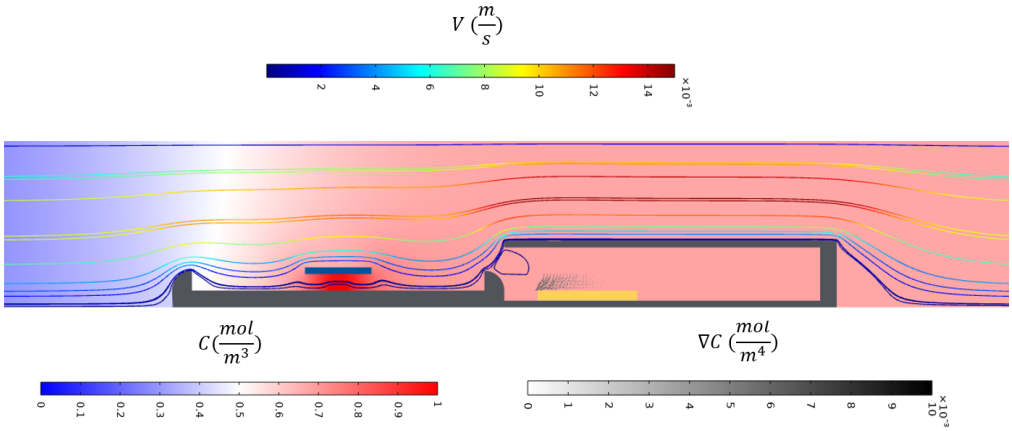

Figure 3.21: Numerical simulation showing concentration of Te precursor C, (background color); its gradient in front of the substrate (arrows) $|\nabla C|$; and carrier gas stream velocity (solid lines) |V|.

Tilted configuration

In this experiment, the Mo substrate is placed with a tilted angle on a support (a piece of a silicon substrate in the experimental configuration) and facing up to investigate the effect of the geometry on the growth area. The numerical simulation represents the concentration of the Te around the substrate in this setup, see Figure 3.22. This simulation predicts a significant improvement in the concentration gradient as indicated by arrow density.

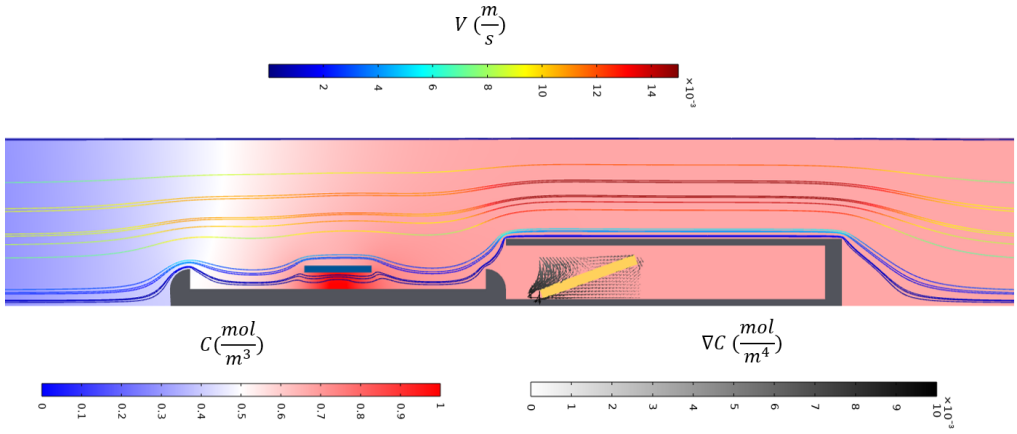

Figure 3.22: Numerical simulation showing concentration of Te precursor C, (background color); its gradient in front of the substrate (arrows) $|\nabla C|$; and carrier gas stream velocity (solid lines) |V|.

Numerical simulation and experimental observation of the growth reveal a significant change in the concentration gradient of Te by tilting the substrate. It is worth noting that the gradient arrows are more concentrated on the left side of the substrate compared to the flat case; see Figure 3.23 panel a and b.

This is also supported by the experimental results showing that in the tilted case, the deposition of Te flakes in that area is observable by optical microscope and Raman investigation. I compare the numerical simulation results and the experimental observations in Figure 3.23. As already mentioned, simulation and experimental results can be easily matched and are in good agreement.

The Raman spectrum of the flat substrate (Figure 3.23 e) on the left edge of the sample (close to Te powder source) shows two broad peaks at 127 and 162 cm^{-1} assigned to A_g and B_g modes of 1T' $MoTe_2$. See the photos panel c showing the points of the Raman spectra. While the spectra taken from the middle and right part of the sample indicate only Si substrate second-order peak at 302 cm^{-1}.

The Raman spectrum of the tilted substrate shows higher intensities with respect to the flat substrate. There are two characteristics peaks at 162 cm^{-1} assigned to B_g mode, and the peak at 127 cm^{-1} is assigned to A_g mode of 1T' phase. There is also a low intense peak at 142 cm^{-1} that can be assigned to the 2H phase.

Figure 3.24 indicates a comparison between the concentration of Te above the substrate area in three different cases that we studied till now. The concentration of Te has a higher amount in the case of tilted configuration, and it is decreasing in the flat case with a 6 cm distance of the boats. It can be seen that the lowest Te concentration happens in the case of 14 cm distance between the boats.

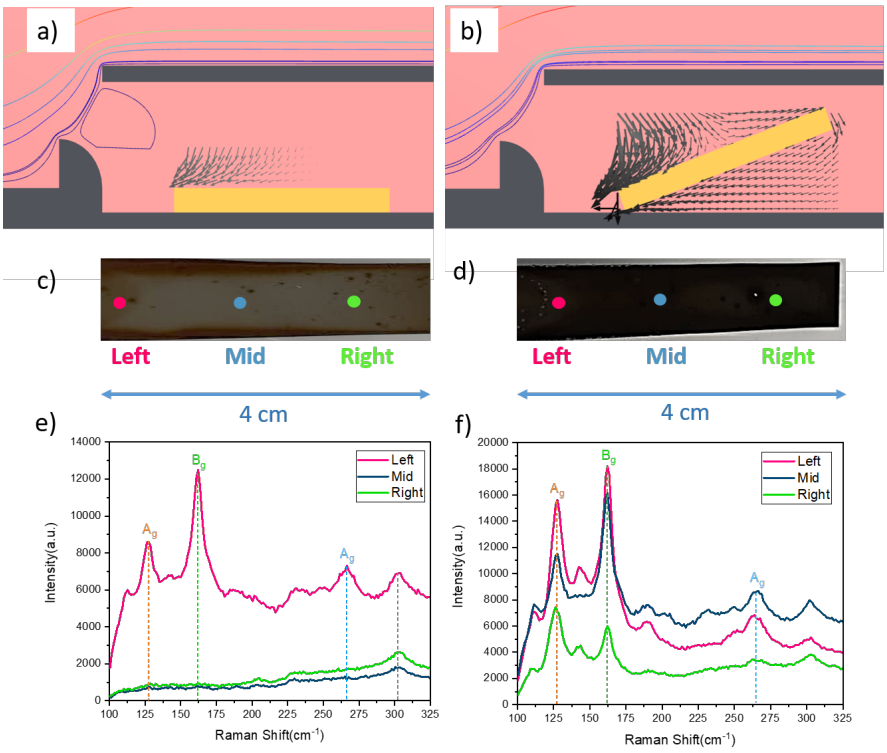

Figure 3.23: Numerical simulation result in a) tilted substrate. b) flat substrate - experimental result in the c) tilted substrate. d) flat substrate - Raman spectra of the e) flat substrate (Sample 6). f) tilted substrate (Sample 7).

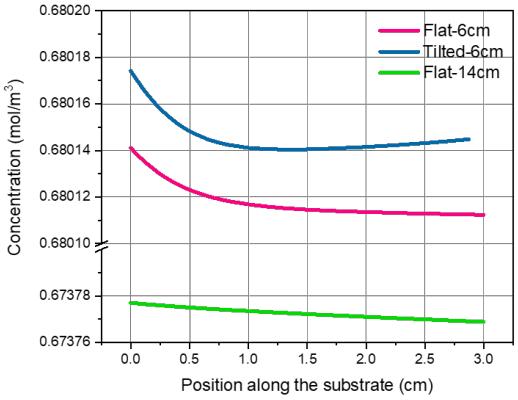

Figure 3.24: The comparison of the concentration on top of the substrate in the flat configuration with 14 and 6 cm distance of boats, and in the tilted configuration.

3.2.4 Growth Time

The study on the sample positioning inside the CVD reactor revealed that better coverage and uniformity could be achieved by adopting the tilted geometry. Nevertheless, the Raman spectra in Figure 3.23 panel f show that high variability is still present in the considered three different regions of the sample (namely left, center, right). In order to improve the homogeneity of the sample, I studied the role of the growth time, keeping the other experimental parameters unchanged compared to the experiment described for the tilted sample in the previous section. The distance between substrate and tellurium boats is kept at 6 cm and growth time varies from 60, 90 to 130 minutes. Table 3.6 summarises the adopted experimental parameters.

The Raman results of the experiments of 90 and 130 minutes of growth time are represented in Figure 3.25. For comparison purposes, I report in panel a) the Raman spectra of the sample obtained using 60 minutes.

For the 90 minutes experiment, the sharp peak of B_g mode appears at 162 cm^{-1}, A_u mode at 110 cm^{-1}, A_g mode at 128 and 260 cm^{-1} are detected (Figure 3.25 b). For 130 minutes of growth time, the peaks become asymmetrical with lower intensities. The 1T' peaks are observed at 127 cm^{-1}, 161 cm^{-1}, and 264 cm^{-1} (Figure 3.25 c).

The comparison of the Raman spectra reported in Figure 3.25 demonstrates the formation of 1T' $MoTe_2$ films at every considered temperature. Nevertheless,

Sample	Upstream T($^\circ C$)	Downstream T($^\circ C$)	Growth Time (minutes)	Carrier Gas Flux (sccm)
8	650	650	90	100 (Ar/H_2)
9	650	650	130	100 (Ar/H_2)

Table 3.6: Process conditions used to grow $MoTe_2$ in Sample 8, and Sample 9.

some important considerations can be made by carefully analyzing the intensity and FWHM of the Raman peaks. As a reference, I analyzed the most intense B_g peak, but the same considerations hold for the other peaks.

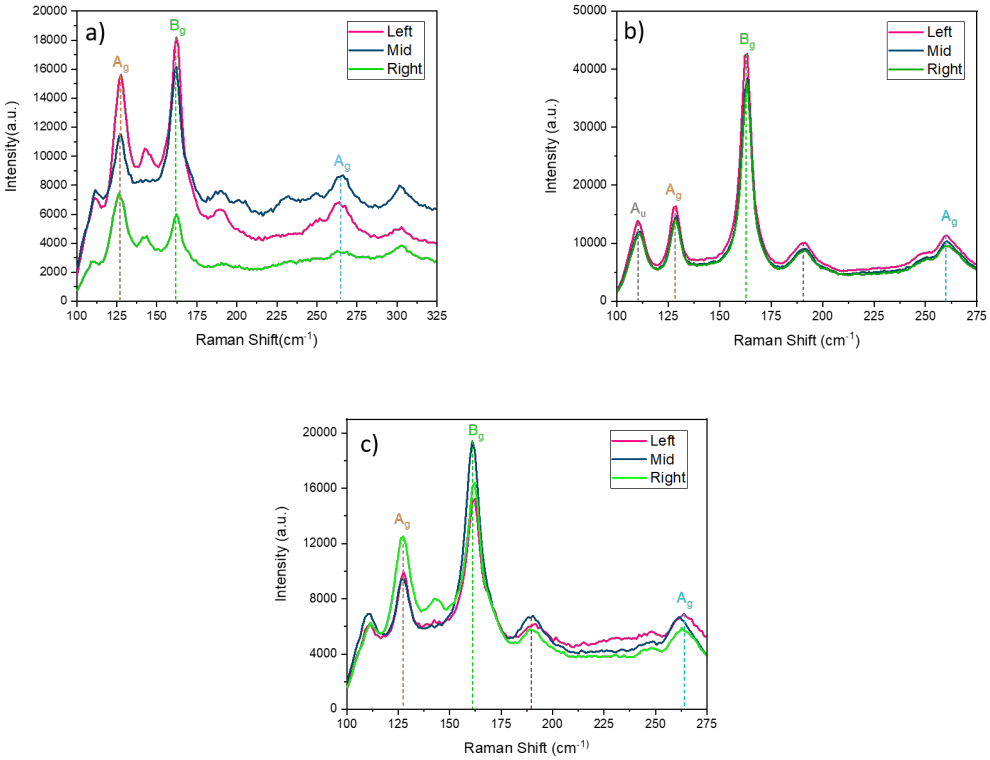

Figure 3.25: Raman spectra of the samples with a) 60 minutes growth time b) 90 minutes growth time c) 130 minutes growth time.

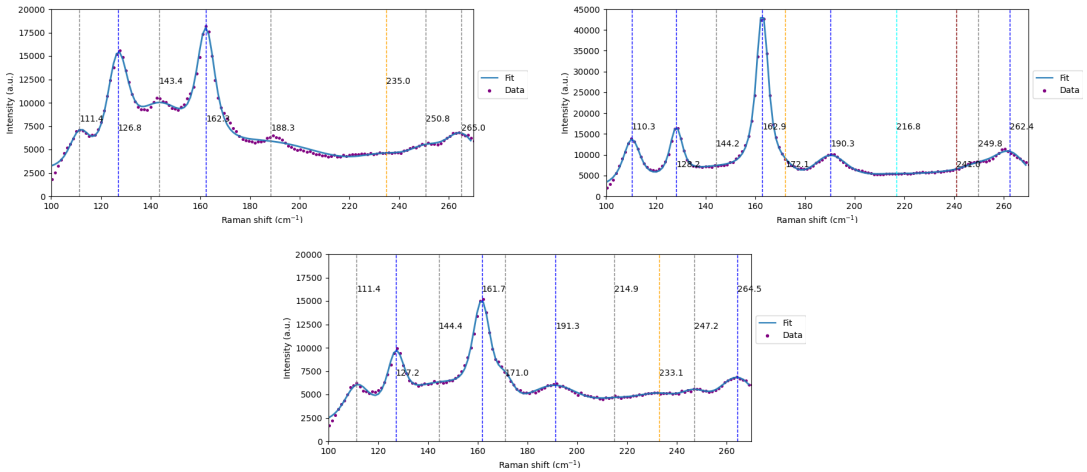

Figure 3.26: The fitted Raman spectrums of the left side (closer to the tellurium source) of the sample 7, 8, and 9 with Voigt function.

The comparison of the intensities and FWHM of the B_g peak at different growth times is represented in Figure 3.27. The methodology for fitting and calculating the uncertainty of the measurements is the same described in the previous sections. From the plot, we can draw the conclusion that increasing the growth time from 60 to 90 minutes will result in a more uniform deposition since the Raman spectra from the left to the right side of the 90 minutes sample show the higher average intensity and less dispersion than the 60 minutes sample. Further increasing the time to 130 minutes seems to negatively affect the spectra, causing a reduction of the peak intensity and an increase of the FWHM compared to the 90 minutes case.

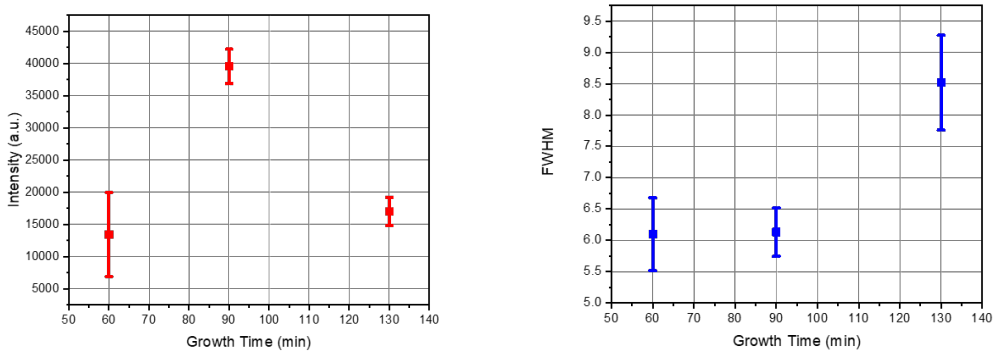

Figure 3.27: Comparison of the intensity of B_g peak at different growth time (left) comparison of the FWHM of the B_g peak at different growth time (right).

Preliminary conclusion

We can conclude that the optimized condition for the uniform $MoTe_2$ deposition is achieved within a window of growth time of around 90 minutes. The increased Raman peak intensity observed changing the growth time from 60 to 90 minutes probably suggests that, in the former experiment, the tellurization of the molybdenum precursor was not completed due to the insufficient duration of the growth step. On the other hand, the reduction of the peak intensity and the concurrent increase of the FWHM, observed by changing the growth time from 90 to 130 minutes, demonstrates that a prolonged growth time may lead to partial evaporation of the $MoTe_2$ and an increase of the structural disorder inside the material.

3.3 $MoTe_2$ phase control

Despite the relatively low energy formation difference between the 2H and 1T' phase, a few studies in literature pointed out that the phase transition in CVD growths depends on the interplay among several experimental parameters [63].

In previous sections, we studied the effect of temperature, carrier gas (flux and chemical composition), the distance between precursors, substrate positioning, and growth time on the tellurization of a molybdenum thin film. Even though we explored a broad range of experimental conditions, the grown $MoTe_2$ layers were deposited predominantly in the metallic 1T' phase, as confirmed by the Raman investigation. Aiming at a phase transition, we, therefore, focused on the role of the tellurium concentration as a knob for the 1T' to 2H formation. Indeed, our goal was to provide extra tellurium atoms, thus promoting the 2H formation as reported in a recent paper for CVD of $MoTe_2$ layers in the pure vapor phase approach [43].

We examined the effect of the Te-rich atmosphere by adding another quartz boat containing an extra 150 mg of Tellurium powder. In addition, we designed a new experiment condition to take into account the introduction of the second source: i) we moved both the boats of the primary tellurium source and molybdenum precursor entirely in the downstream furnaces. ii) we added the second source in the upstream furnace.

Our first attempt was to turn on the upstream furnace containing the extra tellurium atoms once we accomplished the first tellurization of the molybdenum film in the downstream furnace. Unfortunately, this approach resulted in not-reacted molybdenum oxides and extra tellurium clusters deposited on top.

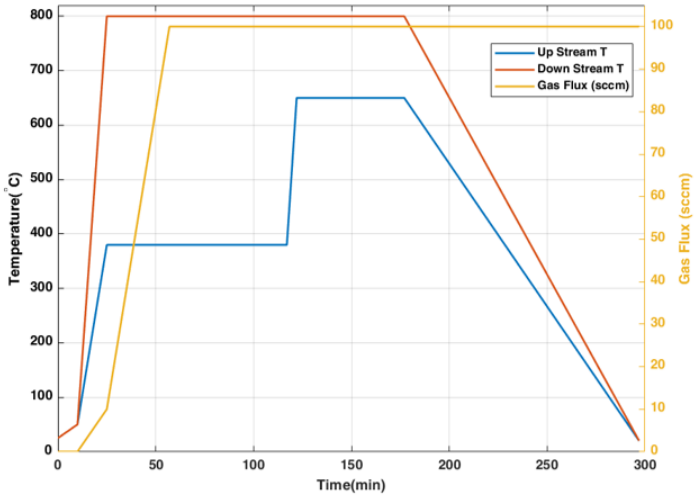

Figure 3.28: Growth ramp used in the experiment with two Te powder boats

In the second attempt, we revised the growth recipe increasing the temperature of the downstream furnace according to the thermal ramp reported in Figure 3.28. The temperature of the upstream furnace is kept below the Te melting point $450°C$ for 120 minutes, while in the downstream furnace, the growth process is carried out at $800°C$ to avoid the presence of not-reacted molybdenum oxide precursor. To provide the extra tellurium atoms, the temperature of the upstream furnace is varied from $380°C$ to $650°C$ after 120 minutes and kept constant for 55 minutes. Then the system is let to cool down by heat exchange with the environment naturally.

The spectra in Figure 3.29 show broad and relatively weak Raman peaks measured in the region localized through the optical microscope. Nevertheless, the prominent characteristic peaks of both 2H $MoTe_2$, E^1_2g at 233 cm^{-1}, and 1T' phase, B_g at 163 cm^{-1}, can be observed. This finding suggests that the 1T' phase develops due to the local tellurium deficiency while the formation of nucleation sites of $2H - MoTe_2$ occurs in localized Te-rich regions. To quantitatively measure the relative proportion between the two phases, we compute the relative intensity between the two characteristic peaks according to the relation [43]:

$$R(1T') = \frac{I_{1T'}}{I_{1T'} + I_{2H}} = \frac{I_{B_g}}{I_{B_g} + I_{E^1_{2g}}} = 50\% \tag{3.2}$$

This dependence allows measuring the relative percentage of 1T' and 2H, which reads 50%.

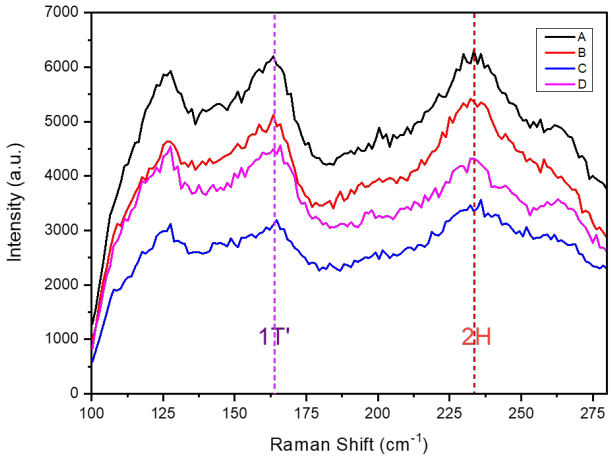

Figure 3.29: Raman spectra of the sample grown using two Te boats

3.4 Kelvin Probe Force Microscopy on the CVD-grown $MoTe_2$

In this section, I use AFM in Kelvin probe mode to characterize the $MoTe_2$ grown with the CVD method. Figure 3.30 shows in panel a) a representative AFM topography of the sample, in panel b) the corresponding surface potential map, in panel c) two image profiles, and in d) the histogram distribution of the surface potential.

As described in the previous sections, the sample obtained by the tellurization process (panel a) inherits a granular structure with nanometer-scale grains from the molybdenum film precursor. In detail, the self-correlation function analysis of this image reveals that the grain size is of the order of 50.22 ± 2.48 nm. In addition, the RMS roughness is 3.8 nm. In panel b) the surface potential voltage applied is 4V, with the lift height = 0.005 µm in dual pass mode. It shows a variation in the range 38 mV - 89 mV with a majority of regions at high potential (yellow regions) and nanometer-scale regions at low potential (blue-dark points).

To ensure that the KPFM technique is working correctly and no topographic artifacts are present, we match in panel c) the height profile with the potential profile along two different pathways. It is important to note that a morphological protrusion from the surface corresponds to different potential values in the two cases: a local minimum in profile 1 and a constant value in profile 2.

This comparative study excludes the so-called topographical cross-talk artifact that occurs when a one-to-one correlation is observed between topographical and potential features. The information on the surface potential of the scanned area is summarized in the histogram distribution shown in panel d). The average potential is at 82 mV, and the full-width-half-maximum of the curve is 11.8 mV.

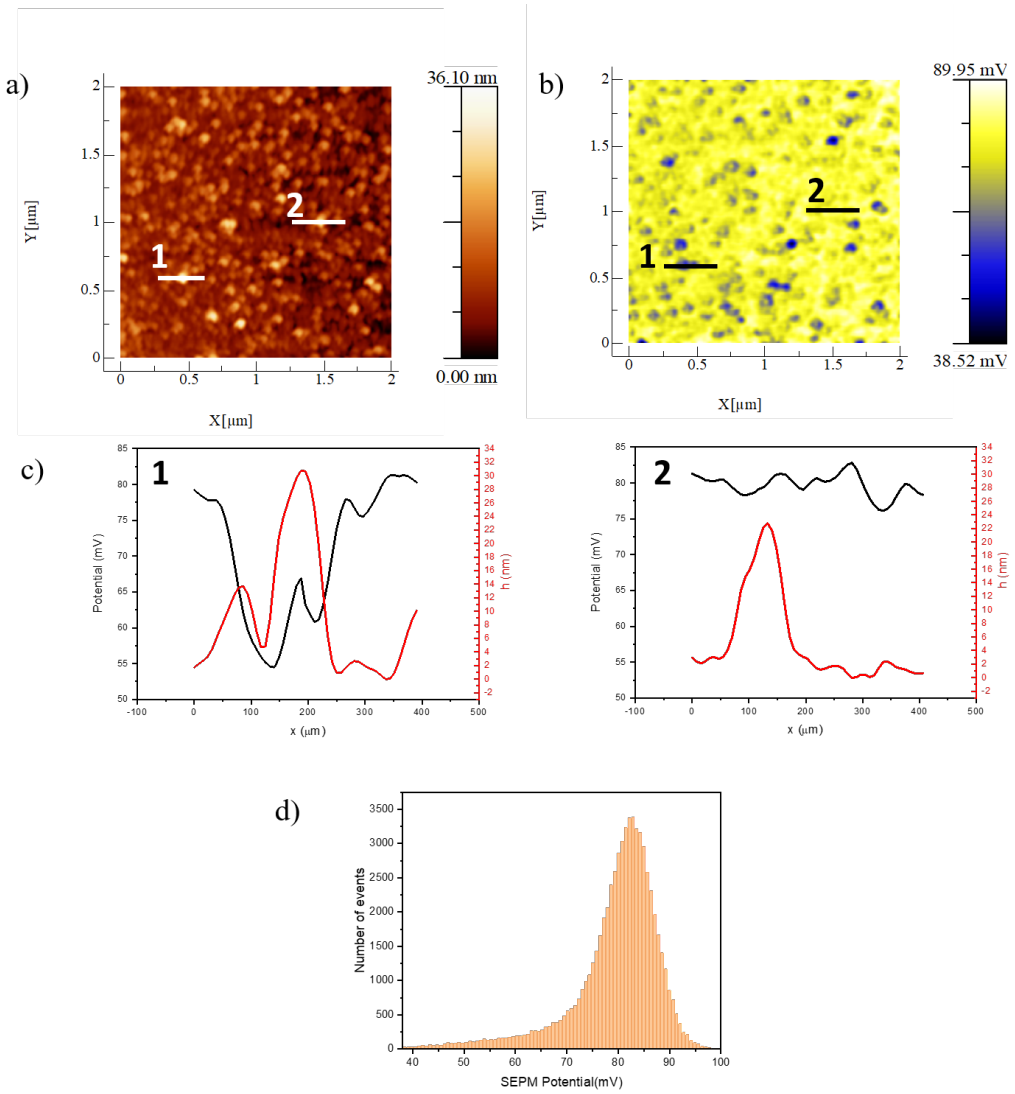

Figure 3.30: a) $2\mu m \times 2\mu m$ topographical image of $MoTe_2$ grown with Mo pre-deposited substrate. b) potential difference of the on/off illumination c) cross-sectional topography and potential profiles along the line 1 and line 2 d) histogram of the surface potential.

In the following, I exploit the KPFM technique to compare the samples obtained by two different growth approaches, tellurization, and co-deposition. I described the tellurization method in the previous sections.

In contrast, the co-deposition method consists of the use of MoO_3 powder as precursors (instead of the pre-deposited Mo film) and in the reaction of the vapor phases of the metal and the tellurium atoms. The deposition using the latter methodology was studied in the CNR lab in a previous thesis work. I used a sample grown using the developed methodology in this comparison. There is a stark difference in the morphological features of the two samples. The sample obtained by the co-deposition process is characterized by a continuous deposition ontop of which is observed the formation of the cluster (or crystallites) of lateral size and height in the hundreds of nanometers range.

For this reason, I show in Figure 3.31 the topography and potential map over a 10 µm × 10 µm area. For a detailed description of the morphological features of these samples, see [64] and [43]. The potential shows a variation in the range 0 mV - 110 mV. Compared to the case of the tellurization, the potential shows a lower average value as confirmed by the potential distribution in panel c).

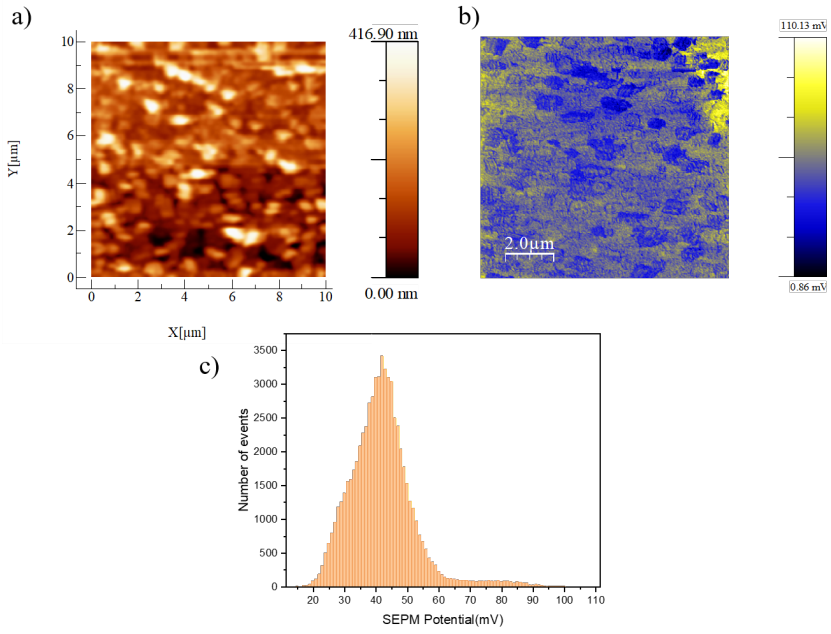

Figure 3.31: a) $10\mu m \times 10\mu m$ topographical image of $MoTe_2$ grown MoO_3 powder b) potential difference of the on/off illumination c) histogram of surface potential.

Raman spectroscopy characterization of the samples is reported in Figure 3.32. On the one hand, the sample obtained by the tellurization process is characterized by a pure 1T' dominant phase with characteristic Raman modes at 109 cm^{-1}, 127 cm^{-1}, and 161 cm^{-1}. On the other hand, the sample obtained by co-deposition does not show uniformity in the allotropic phase, and the Raman peaks are a combination of the 1T' phase and 2H phase. In particular, we can distinguish the E_{1g} mode of the 1T' phase at 137 cm^{-1}, the E^1_{2g} mode of the 2H phase at 229 cm^{-1}, the B_g mode of the 1T' phase at 163 cm^{-1}.

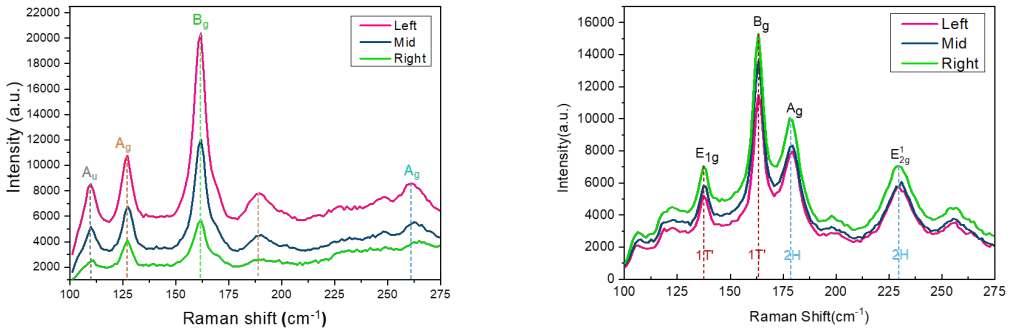

Figure 3.32: Raman spectra of the sample grown with tellurization (left) - Raman spectra of the sample grown with co-deposition (right).

Inspired by the Raman comparison, it is intriguing to study the sample response in the KPFM mode to show whether the difference in the allotropic phase is detectable at the nanoscale with the AFM.

To gain a deeper insight in this respect, I investigated the change in local potential produced in response to an optical excitation in both cases. This technique has been proposed in a recent paper to study TMDs based on sulfur [65].
I used the illumination led, built-in in the AFM system, to provide the excitation illumination. I measured the surface potential at zero illumination (measure in Figure 3.30 and 3.31) and 70 % of the illumination power.

I plot in Figure 3.33 a-b the variation in the potential, called surface photovoltage, for the tellurized and co-deposited samples, respectively.

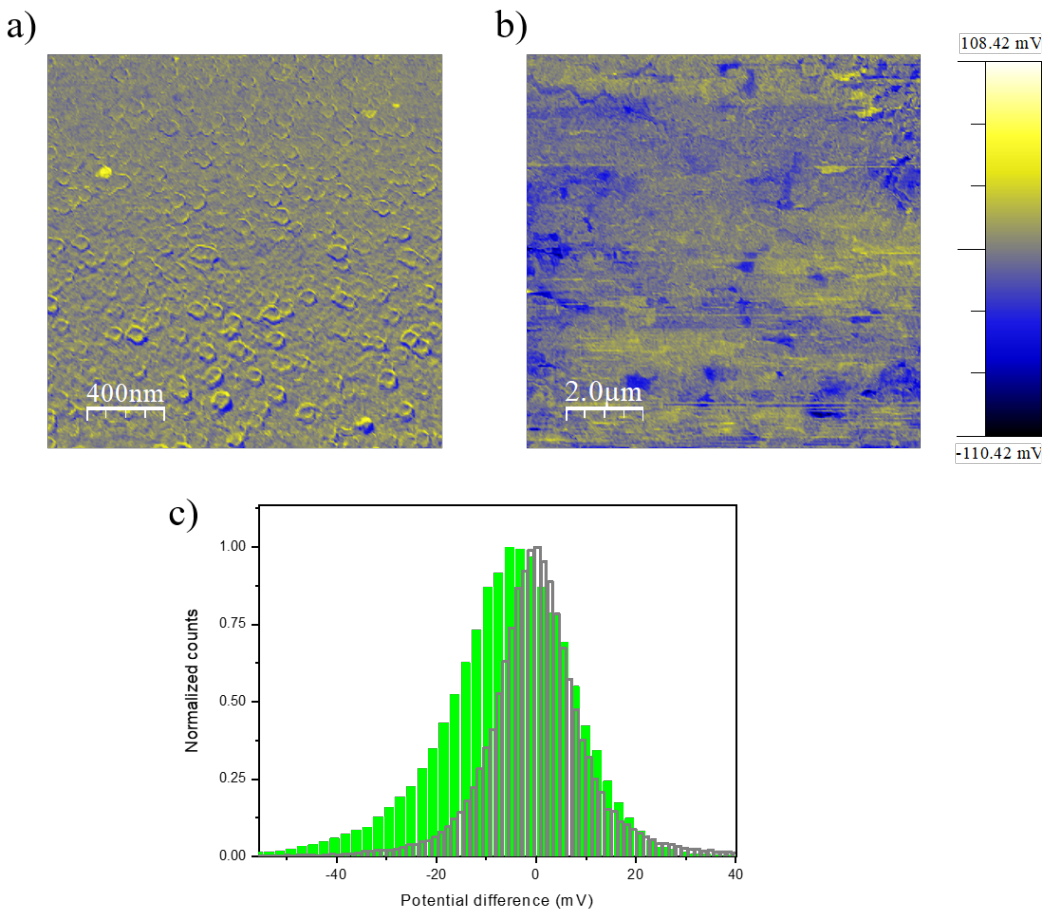

Figure 3.33: a) Variation in potential in the tellurized sample (1T' phase dominant). b) variation in potential in the co-deposited sample (mixed 1T' and 2H phase) - c) histogram distribution of potential difference of the tellurized (gray) and co-deposited (green) samples.

It is interesting to note that in the tellurized film, which is 1T' metallic dominant, the variation in the potential is relatively uniform on the whole surface area.
In contrast, the spatial map of the surface photovoltage for the mixed-phase sample reveals higher contrast in the surface potential due to mixed semiconducting and metallic phases in the co-deposited sample. It also presents regions with different values that hint at a different photoresponse at the nanoscale. Quantitatively, we can observe that the histogram distribution of the potential difference is centered at zero, namely no variation in the potential under illumination in the 1T' phase. At the same time, it shifts towards negative values in the mixed sample.

It can be due to the accumulation of negative charges when under illumination, which results from electron transfer. These results show that this technique provides a way to directly probe the spatially varying charge transfer properties when the system is driven away from equilibrium by illumination [65]. The surface photovoltage KPFM is a useful technique to investigate the photoresponse of nanostructures and their correlation with spatial heterogeneity. Differences in the photoresponses of the tellurized and co-deposited samples reveal the role of different allotropic phases.

Chapter 4

Conclusion

In this thesis, I studied the synthesis of ultra-thin $MoTe_2$ films based on a tellurization approach of a pre-deposited Mo layer on a SiO_2/Si substrate.
In detail, the approach is a revised version of a chemical vapor deposition (CVD) where the precursors of the molybdenum and tellurium react in two different phases, namely solid phase for the molybdenum and vapor phase for tellurium.

I determined the critical parameters of the growth by performing various experiments. First, the optimal growth temperature and carrier gas flux have been optimized. As a result, I found that the temperature range for the heterogeneous solid-vapor reaction to occur is below $700°C$. At the same time, by exceeding this threshold, the deposition will lead to the formation of tellurium clusters. I have drawn these conclusions by matching the AFM morphologies of the samples grown at different temperatures with their Raman scattering spectral features.

In addition, I determined that both the type and amount of carrier gas affect the growth of $MoTe_2$. I found that a reducing atmosphere is detrimental for the growth. I obtained this condition by introducing a small percentage of molecular hydrogen into the gas composition. Moreover, by exploiting a broad range of gas fluxes, I showed that the range 90-150 sccm appears as the best choice for uniform growth, as confirmed by AFM morphological analysis of the samples.

Aiming to improve the deposition quality further, I developed a Finite Element Method in the COMSOL Multiphysics platform by coupling laminar flow with the transport of diluted species models to estimate the precursor concentration and its gradient close to the substrate. I simulated three different conditions:
1) precursor boats distance of 14 cm, 2) precursor boats distance of 6 cm, and 3) tilted substrate configuration at precursor boats distance of 6 cm.
This calculation allowed me to identify the tilted configuration of the substrate

keeping a 6 cm distance from the Te source as the best condition to achieve the highest concentration of tellurium atoms at the substrate surface.

I experimentally verified the crucial role of precursor boats distance in order to increase the growth area and improve the homogeneity of the film in consequence of tilting the pre-deposited Mo substrate toward the precursor and carrier gas fluxes. The AFM and Raman investigations of the samples confirm that the designed conditions are in complete agreement with the simulation, showing that by keeping the distance between the precursors at 6 cm and a tilted positioning of the substrate in the reactor, more uniform coverage of the substrate surface is obtained, Moreover, I showed that this condition improves the uniformity of the growth by comparing the Raman scattering signatures acquired in different regions of the sample.

Another critical parameter that has a crucial role in further improving the uniformity of the growth is time. We observed that the window growth time of around 90 minutes resulted in a significant growth area and very high homogeneity of the grown film. After optimizing the parameters mentioned above, I also examined the role of increasing the Te concentration. I found that a Te-rich environment enables the formation of small domains of the semiconducting 2H phase in the dominant 1T' film. This finding suggests that further increasing the tellurium concentration can be beneficial for the complete transformation of the grown film from the 1T' to the 2H phase. It is worth noting that, on selected samples, I used different AFM configurations, namely electrostatic and Kelvin probe, to have a deeper insight into their physical properties, also matching the experimental results with those obtained on commercial exfoliated flakes.

As an outlook for future experiments, apart from increasing the tellurium concentration aiming at a phase transformation, different substrate configurations (such as vertical or face down) can be explored to further improve the grown material's quality, particularly for what concerns the morphology and roughness. The effectiveness of these configurations can be evaluated before their experimental realization by using the simulation tool I developed during my activity.

Appendix A

Tellurium growth

Chalcogens, more specifically, tellurium (Te), is a p-type semiconductor with a bandgap of ≈ 0.35 eV in bulk and ≈ 1 eV in monolayer. The importance of Te is since it has an asymmetrical crystal structure in its radial direction. The atoms in each individual chain are interacting by covalent bonding. The parallel Te atoms chains are arranged on a 2D hexagonal lattice which are interacting by van der Waals forces [61]. Due to its special structure the synthesis method yielding the 2D Te nanostructures are not much known. The growth of tellurene in mono-layer or few layer was reported for the first time in 2017 [66]. Due to the limited number of experimental studies, a few recent theoretical explorations predict the intriguing properties of 2D tellurene, e.g., extraordinary carrier mobility, significant optical absorption, and high stretchability [67].

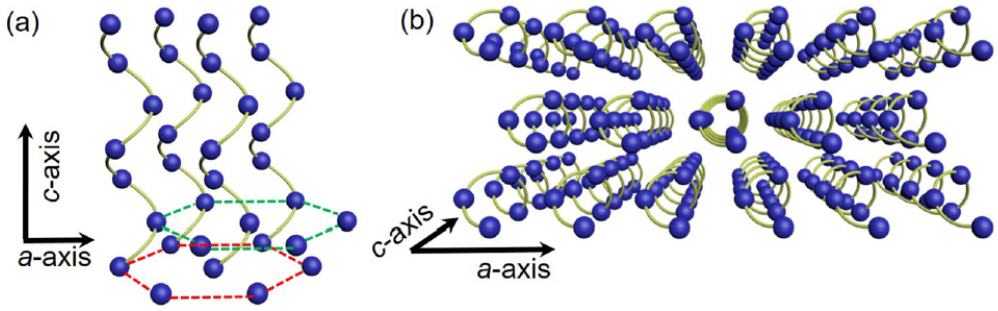

Figure A.1: The lattice structure of Te [61].

Various synthesis methods such as solution-based methods, vapor phase deposition methods, and exfoliation of Te from bulk have been reported in the literature. However, due to the high evaporation rate of Te, the re-evaporation of deposited Te makes it a challenge to create high structural quality Te nanostructures [68].It has been demonstrated that tellurium precipitates in spherical nanoparticles whose crystal structure is trigonal by solution synthesis [69].

In what follows, I intend to summarise the results obtained during the experimental activities to study the capability of the growing tellurium thin film on a large scale SiO_2/Si substrate.

We attempt to grow the tellurene during the $MoTe_2$ experiments, the furnaces temperature, and the gas flux follow the standard $MoTe_2$ recipe. The position of the Si substrate for the growth of Te is shifted upstream near the insulator edge with the distance of 20, and 14cm from the Te powder source. Since from the literature we expect that the Na-based solutions will help to the adhesion of Te on the substrate, we examined the effect of two different Na-based promoters: NaOH and NaCl, on the growth of thin Tellurium film.

In the first experiment, I dissolved 25 mg of NaOH in 100ml of water and transferred it to a piece of SiO_2/Si substrate using a micropipette. Another SiO_2/Si substrate with the same dimension and without exploiting promoter was also used. I put these two pieces of the substrate on top of an alumina boat and insert them in the tube at a 20 cm distance apart from the Te powder source.

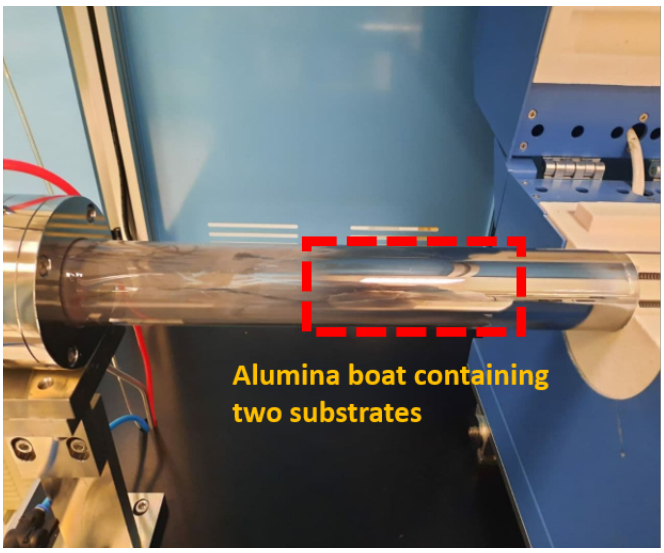

Figure A.2: The position of the boat used for the deposition of the tellurium.

The morphology comparison obtained by AFM in tapping mode demonstrates that by exploiting the NaOH solution the deposited Tellurium flakes has the thickness around 700 nm while in the case of not using NaOH on the substrate, it yields to the formation of flakes with 1.7 μm thickness.

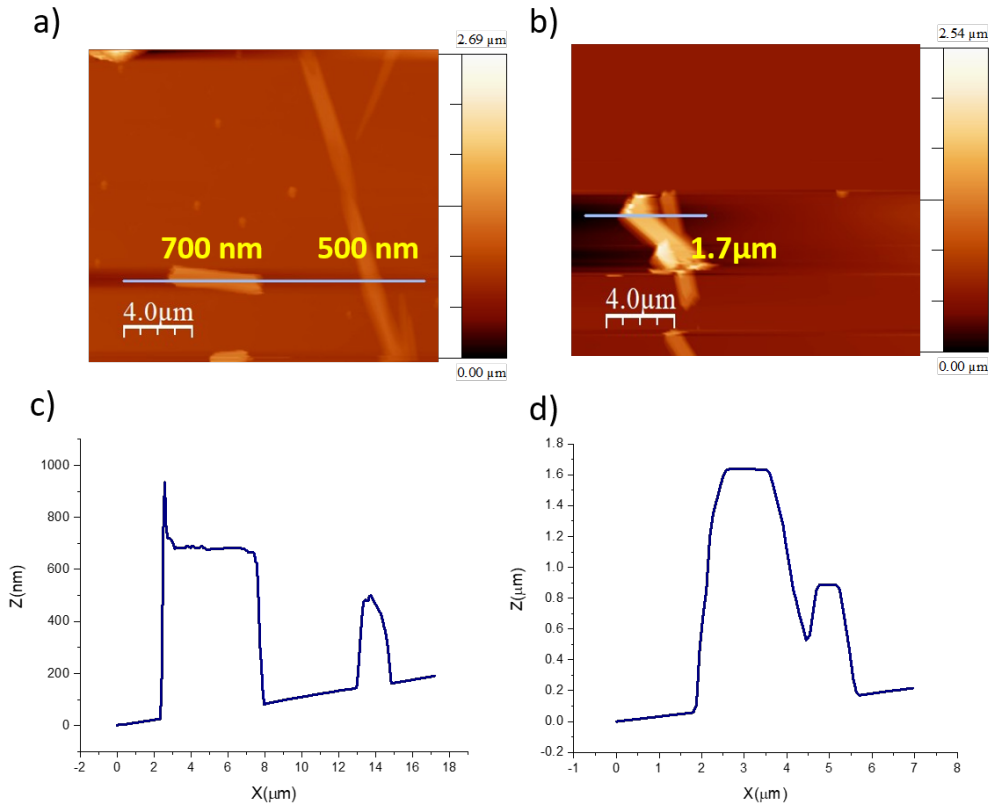

Figure A.3: a) The morphology obtained from the Te deposited flake on the substrate with NaOH. b) The morphology obtained from the Te deposited flake on the substrate without NaOH. c) height profile along the depicted line in a. d) height profile along the depicted line in b.

The Raman spectra of these two samples are reported in Figure A.4.

- In the case of Te growth on a substrate with NaOH promoter, the Raman spectra exhibit two peaks at 619 cm^{-1} and 672 cm^{-1}, which are characteristics peaks of TeO_2 due to the existence of oxygen in the Na-based solution NaOH.
- The Raman spectra were taken from the substrate without the NaOH promoter reveals two peaks of bulk tellurium at 121 cm^{-1} and 141 cm^{-1} at very high intensity, which confirms the high thickness of the Te obtained from AFM measurement.

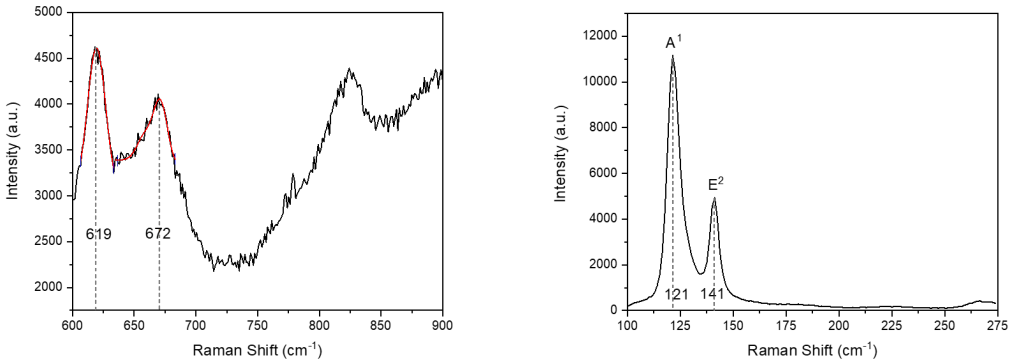

Figure A.4: The Raman spectra taken from the Te deposited using NaOH promoter (left) - Raman spectra taken from the Te deposited without using NaOH promoter (right).

After realizing the growth of TeO_2 instead of thin Te film by exploiting NaOH solution on the substrate, we decided to change the type of the Na-based solution to NaCl. In this case, I made a solution of 250 mg NaCl inside 20 ml water. Then, I transferred the droplets of the solution using a micropipette on a piece of SiO_2/Si substrate and let it dried on a hot plate. I inserted the alumina boat containing two pieces of substrates: one with dried NaCl droplets exposed on the substrate and the other without any promoter. The distance between Te powder source and substrate decreased to 14 cm in this case.

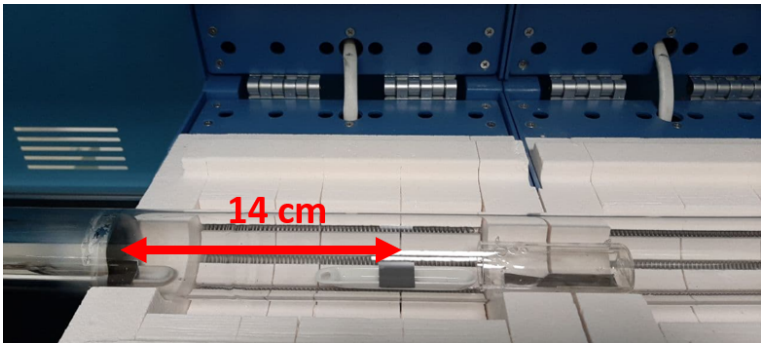

Figure A.5: The position of the boat used for the deposition of the tellurium.

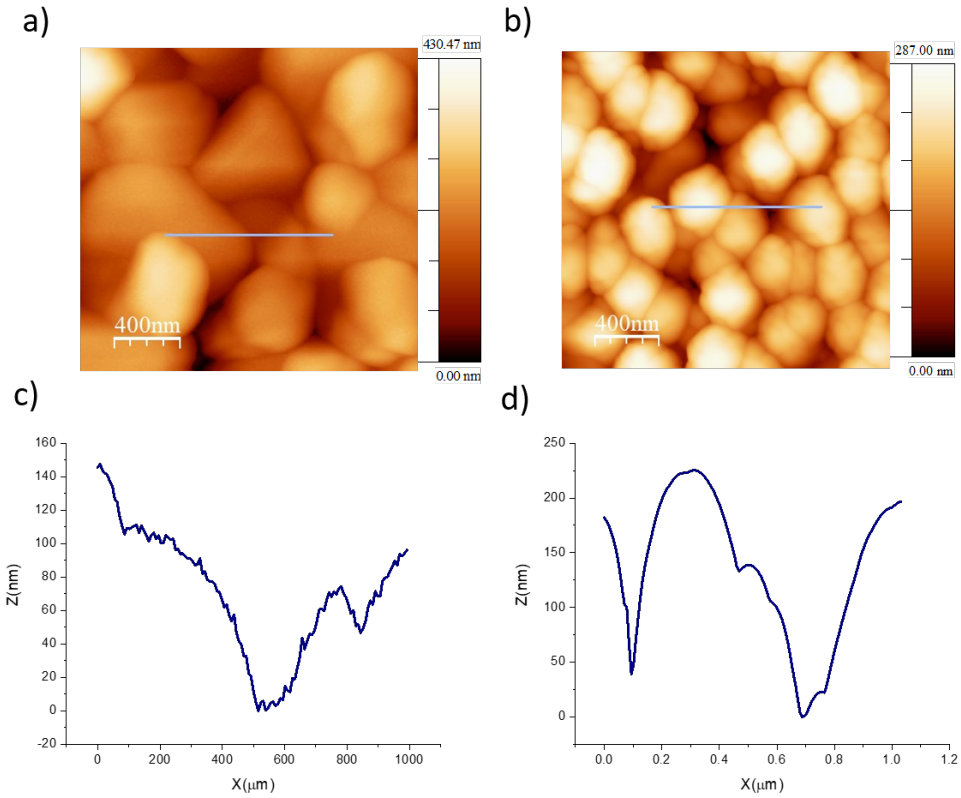

Figure A.6: The morphology obtained from the Te deposited film on the substrate a) with NaCl. b) without NaCl. c) height profile along the depicted line in a. d) height profile along the depicted line in b.

The mean grain size (Figure A.7) was obtained from measuring the FWHM of the peak along the horizontal line profile at the center of the self-correlation image. We can realize that by exploiting NaCl solution on a substrate, the Te deposition leads to the formation of grains of larger size.

The Raman spectrum (Figure A.8) taken from the sample using NaCl promoter reveals two peaks at 120 cm^{-1} and 140 cm^{-1} which have lower intensities in compared with bulk Tellurium.

It can confirm the fact that by exploiting NaCl, the growth of tellurium with lower thickness will be achievable. Indeed, reducing the amount of tellurium would be beneficial to decrease the thickness of the grown film further and reach the 2D domain.

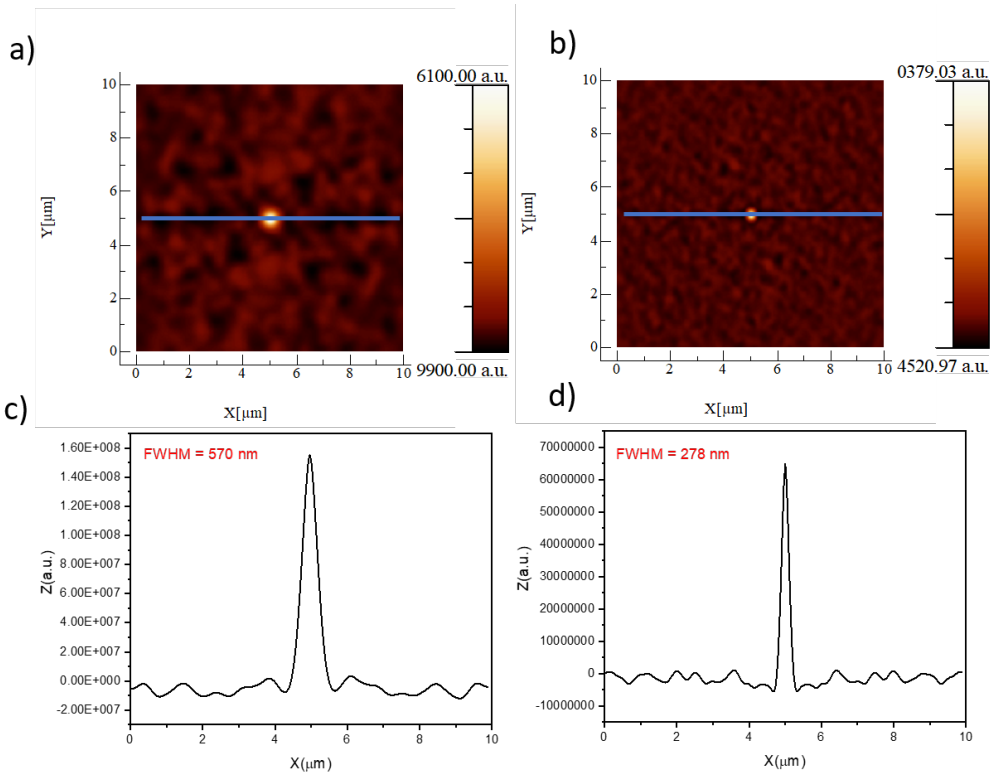

Figure A.7: $10\mu m \times 10\mu m$ self-correlation taken from sample grown a) with NaCl. b) without NaCl - cross-sectional plot along the depicted line c) in a. d) in b.

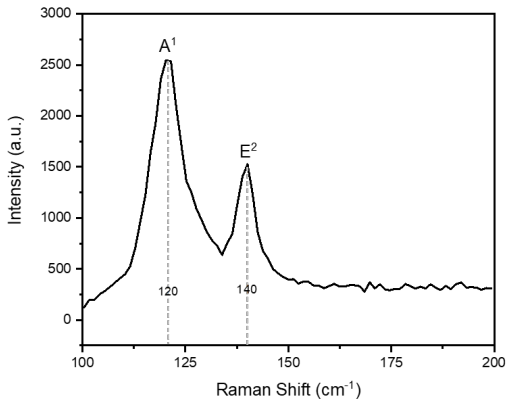

Figure A.8: The Raman spectra taken from the Te deposited using NaCl promoter.

Bibliography

[1] Mingsheng Xu, Tao Liang, Minmin Shi, and Hongzheng Chen. «Graphene-like two-dimensional materials». In: *Chemical reviews* 113.5 (2013), pp. 3766–3798 (cit. on p. 1).

[2] Xinming Li, Li Tao, Zefeng Chen, Hui Fang, Xuesong Li, Xinran Wang, Jian-Bin Xu, and Hongwei Zhu. «Graphene and related two-dimensional materials: Structure-property relationships for electronics and optoelectronics». In: *Applied Physics Reviews* 4.2 (2017), p. 021306 (cit. on p. 1).

[3] Matěj Velický and Peter S. Toth. «From two-dimensional materials to their heterostructures: An electrochemist's perspective». In: *Applied Materials Today* 8 (2017). 2D Materials in Electrochemistry, pp. 68–103 (cit. on pp. 1, 4).

[4] K. S. Novoselov, A. K. Geim, S. V. Morozov, D. Jiang, Y. Zhang, S. V. Dubonos, I. V. Grigorieva, and A. A. Firsov. «Electric Field Effect in Atomically Thin Carbon Films». In: *Science* 306.5696 (2004), pp. 666–669 (cit. on p. 1).

[5] Jin Chong Tan and Anthony K Cheetham. «Mechanical properties of hybrid inorganic–organic framework materials: establishing fundamental structure–property relationships». In: *Chemical Society Reviews* 40.2 (2011), pp. 1059–1080 (cit. on pp. 1, 2).

[6] Shaobin Tang, Weihua Wu, Xiaojun Xie, Xiaokang Li, and Junjing Gu. «Band gap opening of bilayer graphene by graphene oxide support doping». In: *RSC advances* 7.16 (2017), pp. 9862–9871 (cit. on p. 2).

[7] Brian J Schultz, Robert V Dennis, Vincent Lee, and Sarbajit Banerjee. «An electronic structure perspective of graphene interfaces». In: *Nanoscale* 6.7 (2014), pp. 3444–3466 (cit. on p. 2).

[8] Andre K Geim and Irina V Grigorieva. «Van der Waals heterostructures». In: *Nature* 499.7459 (2013), pp. 419–425 (cit. on p. 2).

[9] Xidong Duan, Chen Wang, Anlian Pan, Ruqin Yu, and Xiangfeng Duan. «Two-dimensional transition metal dichalcogenides as atomically thin semiconductors: opportunities and challenges». In: *Chemical Society Reviews* 44.24 (2015), pp. 8859–8876 (cit. on p. 3).

[10] Manish Chhowalla, Hyeon Suk Shin, Goki Eda, Lain-Jong Li, Kian Ping Loh, and Hua Zhang. «The chemistry of two-dimensional layered transition metal dichalcogenide nanosheets». In: *Nature chemistry* 5.4 (2013), pp. 263–275 (cit. on pp. 3, 5, 6).

[11] SJ Haigh et al. «Cross-sectional imaging of individual layers and buried interfaces of graphene-based heterostructures and superlattices». In: *Nature materials* 11.9 (2012), pp. 764–767 (cit. on p. 4).

[12] Chenxi Zhang et al. «Charge Mediated Reversible Metal–Insulator Transition in Monolayer $MoTe_2$ and W x Mo1–x Te2 Alloy». In: *ACS nano* 10.8 (2016), pp. 7370–7375 (cit. on p. 5).

[13] HH Huang, Xiaofeng Fan, David J Singh, and WT Zheng. «Recent progress of TMD nanomaterials: phase transitions and applications». In: *Nanoscale* 12.3 (2020), pp. 1247–1268 (cit. on p. 5).

[14] Wikipedia contributors. *Transition metal dichalcogenide monolayers — Wikipedia, The Free Encyclopedia*. [Online; accessed 9-May-2021]. 2021. URL: `https://en.wikipedia.org/w/index.php?title=Transition_metal_dichalcogenide_monolayers&oldid=1009912603` (cit. on p. 5).

[15] Nardeep Kumar, Sina Najmaei, Qiannan Cui, Frank Ceballos, Pulickel M Ajayan, Jun Lou, and Hui Zhao. «Second harmonic microscopy of monolayer MoS 2». In: *Physical Review B* 87.16 (2013), p. 161403 (cit. on p. 5).

[16] Ignacio Gutiérrez Lezama, Ashish Arora, Alberto Ubaldini, Céline Barreteau, Enrico Giannini, Marek Potemski, and Alberto F Morpurgo. «Indirect-to-direct band gap crossover in few-layer $MoTe_2$». In: *Nano letters* 15.4 (2015), pp. 2336–2342 (cit. on p. 7).

[17] Jin Cheol Park et al. «Phase-engineered synthesis of centimeter-scale 1T-and 2H-molybdenum ditelluride thin films». In: *ACS nano* 9.6 (2015), pp. 6548–6554 (cit. on p. 7).

[18] Dong Hoon Keum et al. «Bandgap opening in few-layered monoclinic $MoTe_2$». In: *Nature Physics* 11.6 (2015), pp. 482–486 (cit. on p. 7).

[19] Karel-Alexander N Duerloo, Yao Li, and Evan J Reed. «Structural phase transitions in two-dimensional Mo-and W-dichalcogenide monolayers». In: *Nature communications* 5.1 (2014), pp. 1–9 (cit. on p. 7).

[20] Xiaofeng Qian, Junwei Liu, Liang Fu, and Ju Li. «Quantum spin Hall effect in two-dimensional transition metal dichalcogenides». In: *Science* 346.6215 (2014), pp. 1344–1347 (cit. on p. 7).

[21] HH Huang, Xiaofeng Fan, David J Singh, Hong Chen, Q Jiang, and WT Zheng. «Controlling phase transition for single-layer MTe 2 (M= Mo and W): modulation of the potential barrier under strain». In: *Physical Chemistry Chemical Physics* 18.5 (2016), pp. 4086–4094 (cit. on p. 7).

[22] Xin Zhang, Qing-Hai Tan, Jiang-Bin Wu, Wei Shi, and Ping-Heng Tan. «Review on the Raman spectroscopy of different types of layered materials». In: *Nanoscale* 8.12 (2016), pp. 6435–6450 (cit. on p. 8).

[23] Mahito Yamamoto et al. «Strong enhancement of Raman scattering from a bulk-inactive vibrational mode in few-layer $MoTe_2$». In: *Acs Nano* 8.4 (2014), pp. 3895–3903 (cit. on p. 9).

[24] Katarzyna Gołasa, Magda Grzeszczyk, Maciej R Molas, Małgorzata Zinkiewicz, Łukasz Bala, Karol Nogajewski, Marek Potemski, Andrzej Wysmołek, and Adam Babiński. «Resonant quenching of Raman scattering due to out-of-plane A1g/A 1 modes in few-layer $MoTe_2$». In: *Nanophotonics* 6.6 (2017), pp. 1281–1288 (cit. on p. 9).

[25] Magdalena Grzeszczyk, Katarzyna Gołasa, M Zinkiewicz, K Nogajewski, Maciej Roman Molas, Marek Potemski, Andrzej Wysmołek, and Adam Babiński. «Raman scattering of few-layers $MoTe_2$». In: *2D Materials* 3.2 (2016), p. 025010 (cit. on p. 9).

[26] Yangye Sun et al. «Phase, Conductivity, and Surface Coordination Environment in Two-Dimensional Electrochemistry». In: *ACS applied materials & interfaces* 11.28 (2019), pp. 25108–25114 (cit. on p. 10).

[27] Bruce E Brown. «The crystal structures of WTe2 and high-temperature $MoTe_2$». In: *Acta Crystallographica* 20.2 (1966), pp. 268–274 (cit. on p. 11).

[28] Michal J Mleczko et al. «Contact engineering high-performance n-type $MoTe_2$ transistors». In: *Nano letters* 19.9 (2019), pp. 6352–6362 (cit. on p. 11).

[29] Nazila Haratipour and Steven J Koester. «Multi-layer $MoTe_2$ p-channel MOSFETs with high drive current». In: *72nd Device Research Conference*. IEEE. 2014, pp. 171–172 (cit. on p. 11).

[30] Yen-Fu Lin, Yong Xu, Che-Yi Lin, Yuen-Wuu Suen, Mahito Yamamoto, Shu Nakaharai, Keiji Ueno, and Kazuhito Tsukagoshi. «Origin of noise in layered $MoTe_2$ transistors and its possible use for environmental sensors». In: *Advanced Materials* 27.42 (2015), pp. 6612–6619 (cit. on p. 11).

[31] Lei Yin, Xueying Zhan, Kai Xu, Feng Wang, Zhenxing Wang, Yun Huang, Qisheng Wang, Chao Jiang, and Jun He. «Ultrahigh sensitive $MoTe_2$ phototransistors driven by carrier tunneling». In: *Applied Physics Letters* 108.4 (2016), p. 043503 (cit. on p. 12).

[32] Ning Ma, Xiao-Yu Jiang, Lu Zhang, Xiao-Shuang Wang, Yu-Liang Cao, and Xian-Zheng Zhang. «Novel 2D Layered Molybdenum Ditelluride Encapsulated in Few-Layer Graphene as High-Performance Anode for Lithium-Ion Batteries». In: *Small* 14.14 (2018), p. 1703680 (cit. on p. 12).

[33] John R Schaibley, Hongyi Yu, Genevieve Clark, Pasqual Rivera, Jason S Ross, Kyle L Seyler, Wang Yao, and Xiaodong Xu. «Valleytronics in 2D materials». In: *Nature Reviews Materials* 1.11 (2016), pp. 1–15 (cit. on p. 13).

[34] Di Xiao, Gui-Bin Liu, Wanxiang Feng, Xiaodong Xu, and Wang Yao. «Coupled spin and valley physics in monolayers of MoS 2 and other group-VI dichalcogenides». In: *Physical review letters* 108.19 (2012), p. 196802 (cit. on p. 13).

[35] Kin Fai Mak and Jie Shan. «Photonics and optoelectronics of 2D semiconductor transition metal dichalcogenides». In: *Nature Photonics* 10.4 (2016), pp. 216–226 (cit. on p. 13).

[36] Shanshan Wang, Youmin Rong, Ye Fan, Mercè Pacios, Harish Bhaskaran, Kuang He, and Jamie H Warner. «Shape evolution of monolayer MoS2 crystals grown by chemical vapor deposition». In: *Chemistry of Materials* 26.22 (2014), pp. 6371–6379 (cit. on p. 14).

[37] Jinbong Seok, Jun-Ho Lee, Dongyeon Bae, Byungdo Ji, Young-Woo Son, Young Hee Lee, Heejun Yang, and Suyeon Cho. «Hybrid catalyst with monoclinic $MoTe_2$ and platinum for efficient hydrogen evolution». In: *APL Materials* 7.7 (2019), p. 071118 (cit. on p. 14).

[38] Jessica C McGlynn et al. «The rapid electrochemical activation of $MoTe_2$ for the hydrogen evolution reaction». In: *Nature communications* 10.1 (2019), pp. 1–9 (cit. on p. 14).

[39] Jinbong Seok et al. «Active hydrogen evolution through lattice distortion in metallic $MoTe_2$». In: *2D Materials* 4.2 (2017), p. 025061 (cit. on p. 14).

[40] Zhong Lin et al. «2D materials advances: from large scale synthesis and controlled heterostructures to improved characterization techniques, defects and applications». In: *2D Materials* 3.4 (2016), p. 042001 (cit. on p. 15).

[41] Lin Zhou et al. «Large-area synthesis of high-quality uniform few-layer $MoTe_2$». In: *Journal of the American Chemical Society* 137.37 (2015), pp. 11892–11895 (cit. on p. 15).

[42] Zhiyuan Zeng, Zongyou Yin, Xiao Huang, Hai Li, Qiyuan He, Gang Lu, Freddy Boey, and Hua Zhang. «Single-Layer Semiconducting Nanosheets: High-yield preparation and device fabrication». In: *Angewandte Chemie* 123.47 (2011), pp. 11289–11293 (cit. on p. 16).

[43] Christian Martella, Alessio Quadrelli, Pinaka Pani Tummala, Cristina Lenardi, Roberto Mantovan, Alessio Lamperti, and Alessandro Molle. «Tailoring the Phase in Nanoscale $MoTe_2$ Grown by Barrier-Assisted Chemical Vapor Deposition». In: *Crystal Growth & Design* 21.5 (2021), pp. 2970–2976 (cit. on pp. 17, 69, 70, 73).

[44] Ghenadii Korotcenkov. *Metal Oxide Powder Technologies: Fundamentals, Processing Methods and Applications*. Elsevier, 2020 (cit. on p. 17).

[45] URL: `https://www.mdm.imm.cnr.it/articles/new-fully-automated-cvd-system-2d-tmd-growth-cnr-imm` (cit. on p. 19).

[46] URL: `https://www.nanophoton.net/lecture-room/lecture-room-category/raman-spectroscopy` (cit. on p. 20).

[47] Wikipedia contributors. *Raman spectroscopy — Wikipedia, The Free Encyclopedia*. [Online; accessed 2-June-2021]. 2021. URL: `https://en.wikipedia.org/w/index.php?title=Raman_spectroscopy&oldid=1026267797` (cit. on p. 21).

[48] Bernhard Schrader. *Infrared and Raman Spectroscopy*. New York, VCH Publishers, 1995 (cit. on p. 21).

[49] URL: `https://www.mdm.imm.cnr.it/articles/characterization-agrate-unit` (cit. on p. 21).

[50] URL: `https://www.doitpoms.ac.uk/tlplib/afm/cantilever.php` (cit. on p. 25).

[51] Greg Haugstad. *Atomic force microscopy: understanding basic modes and advanced applications*. John Wiley & Sons, 2012 (cit. on p. 25).

[52] Bin Wang, Xiao Wu, Tat-Hean Gan, and Alexis Rusinek. «Finite element modelling of atomic force microscope cantilever beams with uncertainty in material and dimensional parameters». In: (2014) (cit. on p. 25).

[53] Christian Martella et al. «Changing the Electronic Polarizability of Monolayer MoS2 by Perylene-Based Seeding Promoters». In: *Advanced Materials Interfaces* 7.20 (2020), p. 2000791 (cit. on p. 29).

[54] Tian Tian, Declan Scullion, Dale Hughes, Lu Hua Li, Chih-Jen Shih, Jonathan Coleman, Manish Chhowalla, and Elton JG Santos. «Electronic polarizability as the fundamental variable in the dielectric properties of two-dimensional materials». In: *Nano letters* 20.2 (2019), pp. 841–851 (cit. on p. 30).

[55] Marc Descoteaux, Jacob P Sunnerberg, and Cristian Staii. «Quantitative characterization of dielectric properties of nanoparticles using electrostatic force microscopy». In: *AIP Advances* 10.11 (2020), p. 115118 (cit. on p. 31).

[56] M Nonnenmacher, MP o'Boyle, and H Kumar Wickramasinghe. «Kelvin probe force microscopy». In: *Applied physics letters* 58.25 (1991), pp. 2921–2923 (cit. on p. 33).

[57] Wilhelm Melitz, Jian Shen, Andrew C Kummel, and Sangyeob Lee. «Kelvin probe force microscopy and its application». In: *Surface science reports* 66.1 (2011), pp. 1–27 (cit. on p. 33).

[58] Jong Hun Kim, Jinhwan Lee, Jae Hyeon Kim, CC Hwang, Changgu Lee, and Jeong Young Park. «Work function variation of MoS_2 atomic layers grown with chemical vapor deposition: The effects of thickness and the adsorption of water/oxygen molecules». In: *Applied Physics Letters* 106.25 (2015), p. 251606 (cit. on p. 34).

[59] Silvia Vangelista et al. «Towards a uniform and large-scale deposition of MoS_2 nanosheets via sulfurization of ultra-thin Mo-based solid films». In: *Nanotechnology* 27.17 (2016), p. 175703 (cit. on pp. 42, 43, 50, 51).

[60] Manoj K Jana, Anjali Singh, Archana Sampath, CNR Rao, and Umesh V Waghmare. «Structure and Electron-Transport Properties of Anion-Deficient $MoTe_2$: A Combined Experimental and Theoretical Study». In: *Zeitschrift für anorganische und allgemeine Chemie* 642.23 (2016), pp. 1386–1396 (cit. on pp. 49, 50).

[61] Yuchen Du, Gang Qiu, Yixiu Wang, Mengwei Si, Xianfan Xu, Wenzhuo Wu, and Peide D Ye. «One-dimensional van der Waals material tellurium: Raman spectroscopy under strain and magneto-transport». In: *Nano letters* 17.6 (2017), pp. 3965–3973 (cit. on pp. 51, 79).

[62] Fu Zhang, Kasra Momeni, Mohammed Abu AlSaud, Amin Azizi, Mel F Hainey, Joan M Redwing, Long-Qing Chen, and Nasim Alem. «Controlled synthesis of 2D transition metal dichalcogenides: from vertical to planar MoS_2». In: *2D Materials* 4.2 (2017), p. 025029 (cit. on p. 60).

[63] Leijie Sun, Manman Ding, Jie Li, Li Yang, Xun Lou, Zijian Xie, Wenfeng Zhang, and Haixin Chang. «An Investigation in Phase Transition of $MoTe_2$ Film with Continuous Tellurization Reaction». In: *IOP Conference Series: Materials Science and Engineering*. Vol. 677. 2. IOP Publishing. 2019, p. 022123 (cit. on p. 69).

[64] Alessio Quadrelli. «Tellurium-based van der Waals solids: chemical vapour deposition and characterization». In: (2019) (cit. on p. 73).

[65] Melinda J Shearer, Ming-Yang Li, Lain-Jong Li, Song Jin, and Robert J Hamers. «Nanoscale surface photovoltage mapping of 2D materials and heterostructures by illuminated Kelvin probe force microscopy». In: *The Journal of Physical Chemistry C* 122.25 (2018), pp. 13564–13571 (cit. on pp. 74, 76).

[66] Nicholas R Glavin, Rahul Rao, Vikas Varshney, Elisabeth Bianco, Amey Apte, Ajit Roy, Emilie Ringe, and Pulickel M Ajayan. «Emerging applications of elemental 2D materials». In: *Advanced Materials* 32.7 (2020), p. 1904302 (cit. on p. 79).

[67] Wenzhuo Wu, Gang Qiu, Yixiu Wang, Ruoxing Wang, and Peide Ye. «Tellurene: its physical properties, scalable nanomanufacturing, and device applications». In: *Chemical Society Reviews* 47.19 (2018), pp. 7203–7212 (cit. on p. 79).

[68] Keshab R Sapkota, Ping Lu, Douglas L Medlin, and George T Wang. «High temperature synthesis and characterization of ultrathin tellurium nanostructures». In: *APL Materials* 7.8 (2019), p. 081103 (cit. on p. 80).

[69] CD Gutiérrez-Lazos, F Solıs-Pomar, MF Meléndrez, AM Espinoza-Rivas, MA Pérez-Guzmán, R Ortega-Amaya, M Ortega-López, and E Pérez-Tijerina. «A simple method for the deposition of nanostructured tellurium synthesized in ammonia solution». In: *Applied Nanoscience* 6.7 (2016), pp. 1053–1057 (cit. on p. 80).